

IntechOpen

Electron Microscopy

Edited by Mohsen Mhadhbi



Electron Microscopy

Edited by Mohsen Mhadhbi

Published in London, United Kingdom

Electron Microscopy
<http://dx.doi.org/10.5772/intechopen.97922>
Edited by Mohsen Mhadhbi

Contributors

Lanzhuang Chen, Liming Guan, Muhammad Mustafa, Majid Jehangir, Anwar Latif, Neng Nenden Mulyaningsih, Rum Sapundani, Cengiz Temiz, Taitel-Goldman Nurit, Maša Skelin Klemen, Jurij Dolensek, Andraž Stožer, Saška Lipovšek, Ismael Valladolid-Acebes, Peter Körber, Niha Ansari

© The Editor(s) and the Author(s) 2022

The rights of the editor(s) and the author(s) have been asserted in accordance with the Copyright, Designs and Patents Act 1988. All rights to the book as a whole are reserved by INTECHOPEN LIMITED. The book as a whole (compilation) cannot be reproduced, distributed or used for commercial or non-commercial purposes without INTECHOPEN LIMITED's written permission. Enquiries concerning the use of the book should be directed to INTECHOPEN LIMITED rights and permissions department (permissions@intechopen.com).

Violations are liable to prosecution under the governing Copyright Law.



Individual chapters of this publication are distributed under the terms of the Creative Commons Attribution 3.0 Unported License which permits commercial use, distribution and reproduction of the individual chapters, provided the original author(s) and source publication are appropriately acknowledged. If so indicated, certain images may not be included under the Creative Commons license. In such cases users will need to obtain permission from the license holder to reproduce the material. More details and guidelines concerning content reuse and adaptation can be found at <http://www.intechopen.com/copyright-policy.html>.

Notice

Statements and opinions expressed in the chapters are these of the individual contributors and not necessarily those of the editors or publisher. No responsibility is accepted for the accuracy of information contained in the published chapters. The publisher assumes no responsibility for any damage or injury to persons or property arising out of the use of any materials, instructions, methods or ideas contained in the book.

First published in London, United Kingdom, 2022 by IntechOpen
IntechOpen is the global imprint of INTECHOPEN LIMITED, registered in England and Wales,
registration number: 11086078, 5 Princes Gate Court, London, SW7 2QJ, United Kingdom

British Library Cataloguing-in-Publication Data

A catalogue record for this book is available from the British Library

Additional hard and PDF copies can be obtained from orders@intechopen.com

Electron Microscopy
Edited by Mohsen Mhadhbi

p. cm.

Print ISBN 978-1-80355-945-2

Online ISBN 978-1-80355-946-9

eBook (PDF) ISBN 978-1-80355-947-6

We are IntechOpen, the world's leading publisher of Open Access books Built by scientists, for scientists

5,900+

Open access books available

145,000+

International authors and editors

180M+

Downloads

156

Countries delivered to

Our authors are among the
Top 1%

most cited scientists

12.2%

Contributors from top 500 universities



WEB OF SCIENCE™

Selection of our books indexed in the Book Citation Index
in Web of Science™ Core Collection (BKCI)

Interested in publishing with us?
Contact book.department@intechopen.com

Numbers displayed above are based on latest data collected.
For more information visit www.intechopen.com



Meet the editor



Dr. Mohsen Mhadhbi obtained his Ph.D. from the University of Sfax, Tunisia. He is currently an Assistant Professor of Chemistry at the National Institute of Research and Physicochemical Analysis, Tunisia. His research interests include nanomaterials, energy, powder technology, ceramics, composites, modeling, and simulations. Dr. Mhadhbi has published works in national and international journals and books. He is a teacher in Materials Science and has supervised several researchers in this field. He is also a member of various scientific associations and an editorial board member and reviewer of many reputable scientific journals.

Contents

| | |
|--|-----------|
| Preface | XI |
| Section 1 | |
| Electron Microscopy for Materials Science | 1 |
| Chapter 1 | 3 |
| Scanning Electron Microscopy <i>by Cengiz Temiz</i> | |
| Chapter 2 | 19 |
| Minerals Observed by Scanning Electron Microscopy (SEM), Transmission Electron Microscopy (TEM) and High Resolution Transmission Electron Microscopy (HRTEM) <i>by Taitel-Goldman Nurit</i> | |
| Chapter 3 | 33 |
| Investigation on Building Materials with the SEM in the ESEM Mode to Demonstrate Their Capillarity Using the Contact Angle Method <i>by Peter Körber</i> | |
| Section 2 | |
| Electron Microscopy for Biomedical Applications | 49 |
| Chapter 4 | 51 |
| Atomic Force Microscope in Forensic Examination <i>by Niha Ansari</i> | |
| Chapter 5 | 79 |
| The Cytological Mechanism of Apospory in <i>Paspalum notatum</i> Analyzed by Differential Interference-Contrast Microscopy <i>by Lanzhuang Chen and Liming Guan</i> | |
| Chapter 6 | 99 |
| Analysis of Osteoporosis by Electron Microscopy <i>by Neng Nenden Mulyaningsih and Rum Sapundani</i> | |

| | |
|---|------------|
| Chapter 7 | 117 |
| Application of Transmission Electron Microscopy to Detect Changes in Pancreas Physiology | |
| <i>by Maša Skelin Klemen, Jurij Dolensšek, Ismael Valladolid-Acebes, Andraž Stožer and Saška Lipovšek</i> | |
| Chapter 8 | 139 |
| Laser-Induced Breakdown Spectroscopy and Microscopy Study of Human Dental Tissues | |
| <i>by Muhammad Mustafa, Anwar Latif and Majid Jehangir</i> | |

Preface

Electron microscopy is a useful tool for examining morphological features of different materials. It is a technique for investigating the extremely fine detail or micro- and nanostructure of samples in various areas, such as biochemistry, materials science, microbiology, immunology, pathology, toxicology, geology, and so on.

In recent years, electron microscopy has attracted the scientific and industrial attention of many-electron microscopists.

This book provides a comprehensive overview of electron microscopy and its principles, models, and applications. It also covers advanced topics and trends in the R&D of electron microscopy. It includes eight chapters over two sections addressing electron microscopy for materials science and electron microscopy for biomedical applications.

The book is a valuable guide for materials scientists, physicists, chemists, pharmacists, earth scientists, biologists, and others. It is a powerful tool for new and experienced electron microscopists.

It is my great pleasure to acknowledge the assistance of Ms. Ana Cink for all her help throughout the publication process. I hope that the readers will find this book interesting and helpful for their works and studies.

All suggestions for the improvement of this book will be gratefully acknowledged.

Mohsen Mhadhbi
National Institute of Research and Physicochemical Analysis,
Ariana, Tunisia

Section 1

Electron Microscopy for Materials Science

Chapter 1

Scanning Electron Microscopy

Cengiz Temiz

Abstract

Scanning electron microscopy (SEM) is the most preferred method in microstructural analysis today. In this method, electrons accelerated by high voltage (0-30 kV) are focused on the sample. During the scanning of the surface of this focused electron beam, electrons and material atoms interact. Electrons and X-rays formed as a result of this interaction are collected by detectors. These signals coming to the detector are converted into digital signals and given to the computer screen. The image taken on the screen gives us information about the microstructure of our sample. In addition, SEM have the ability to perform microchemical analysis. Elemental analyzes of the surface can also be performed with the energy dispersive X-ray (EDX) feature. SEM has a much higher resolution and focusing depth compared to optical microscopes. For example, at 1000X magnification, the focal depth of the optical microscope is 0.1 μm , while the focal depth of the SEM is in the range of 30–40 μm . In today's technology, very modern and superior scanning electron microscopes are produced and used.

Keywords: SEM, EDX, resolution, imaging, sample preparation

1. Introduction

Microscope is derived from the Greek words mikros (small) and Skopeo (look at) [1]. It arose from the need to see and interpret objects at the micro and later nano levels that humanity could not see with the naked eye. From past to present, human beings need to see what is far from them closely. Technological developments and the advancement of the scientific world should shed light on these demands [2, 3]. The scanning electron microscope (SEM), which has made a great contribution to the development of the micro world view, has become a masterpiece in this regard. Just as a kitchen cannot be thought of without a knife, it is unthinkable that we can understand micro and nano structures without enlarging them, especially in metallurgy and micro biology [3, 4]. It makes a great contribution to the examination of wet and dry structures in their natural state, especially in biological samples [2, 5]. For this reason, SEM has become a basic need. Today, this instrument, which is the basis for scientific research, has two types as optical and electron. Optical microscopes use a radiation source, while electron microscopes use an electron source. While optical microscopes were sufficient up to a certain level, they were insufficient for high magnification needs [4, 6]. For this reason, electron microscopes were needed and developed to meet the need for higher magnification. In this part of our book, the historical development, general features and usage areas of SEM will be discussed.

2. Historical development

The human eye's ability to see very small and fine details is limited. For this reason, optical devices have been developed that help to see smaller images and details by changing the light paths that provide the transmission of the image with the help of various lenses. In 1923, De Broglie showed that electrons have wave behavior. In 1926, Busch discovered that electrons are deflected in a magnetic field. In 1935, Max Knoll became the name that produced the first SEM device. The first commercial scanning electron microscope was produced by Siemens in 1965. When Max Knoll manufactured the first Scanning Electron microscope in Berlin in 1935, he did not need a patent because he could not reach high magnifications [1]. In the same period, transmissive electron microscopes (TEM) are being developed, but images with the desired resolution cannot be obtained. With the simultaneous development and use of electronics with optical systems, imaging at high magnifications has become possible. The scanning electron microscope, designed within the framework of electrooptical principles, is one of the devices that serve this purpose. In addition to its use in research and development studies in many branches, SEM is widely used in chip production in microelectronics, error analysis in different branches of industry, biological sciences, medicine and criminal applications [2]. As a result of technological developments, SEM devices with high resolution field emission gun (FEG) have been developed. For this reason, the potential of SEM has emerged.

3. General features

In scanning electron microscope image formation, electrons accelerated by high voltage are focused onto the sample. This focused beam of electrons scans the sample surface. During scanning, various interferences occur between electron and sample atoms. Signals resulting from this interference are collected by appropriate sensors. The signals passed through the signal amplifiers are then transferred to the screen of a cathode ray tube. Thus, a surface image is obtained [3]. In modern systems, the signals obtained from the sensors are easily converted into digital signals and transferred to the monitor. In newly developed devices, it expands the usage area by combining separation power, depth of focus and imaging. For example, while the optical microscope is 0.1 μm at 1000X magnification, this focal depth reaches 30 μm in the scanning electron microscope. This situation is compared in more detail in **Table 1**.

| | Light Microscope | Electron Microscope |
|-------------------|---|--|
| Lighting Source | Visible rays ($\lambda = 550 \text{ nm}$) | Electron beam ($\lambda = 0.005 \text{ nm}$) |
| Resolution | 0.25 μm | 0.05 nm |
| Max Magnification | 1500X | 1,000,000 X |
| Lens Type | Glass Lenses | Electromagnetic Lenses |
| Vacuum | Without Vacuum | Electrons travel all the way under vacuum |

Table 1.
Differences in optical and electron microscope.

Today, the discrimination power of modern scanning electron microscopes can be as low as 0.05 nm.

The Quanta FEG 450 model, shown in **Figure 1** [7], provides an advantage in imaging biological and metallic samples at high resolution and effectively, thanks to its high and low vacuum mode.

3.1 Working principle

The scanning electron microscope consists of three main parts: optical column, sample chamber, and imaging (**Figure 2**) [8]. In the optical part, it forms the electron gun, which is the source of the electron beam. In this part, there is an anode plate to which high voltage is applied to accelerate the electrons falling on the sample, condensing lenses to ensure uniform electron beam formation, objective lens to focus, and apertures of different diameters to adjust the density of this lens. Magnetic lenses and deflectors located here thin the electron beam coming from the electron gun and focus it on the sample surface. This system, namely the optical column, is kept in a vacuum of 10^{-4} – 10^{-7} Pa. In the image system, there are detectors that collect the electrons and radiations formed as a result of the sample interference with the incoming electron beam. These detectors amplify electrons or signals that are reflected or interfering from the surface. At the same time, these detectors multiply these signals and convert them into digital signals and send them to the screen through video multipliers [9].

3.2 Electron gun

One of the most important parts of electron microscopes is electron guns, which we call electron sources. It is very important for imaging that the source can produce electrons continuously and uniformly. This is just like a river that constantly flows into a dam built for a hydroelectric power plant. While tungsten filaments were generally used for the first commercial SEM, FEG guns are now used more commonly and effectively. An important point here is that the tungsten filament does not require a vacuum, while the FEG source is in a vacuum environment [3, 9]. One reason for this is the excellent blasting of the electron flow in a vacuum-free environment. Below we can see the various electron sources (see **Figure 3**).

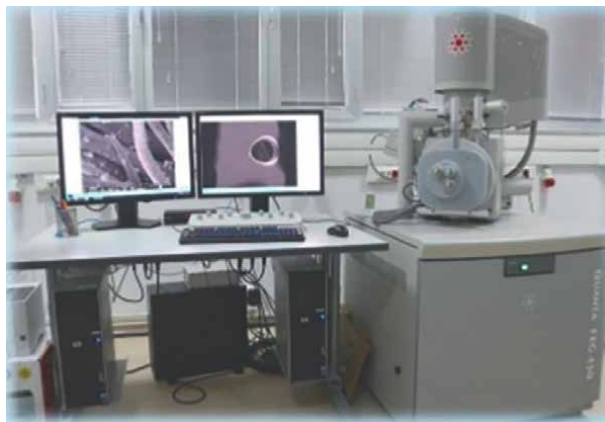


Figure 1.
FEG (field emission gun) scanning electron microscope.

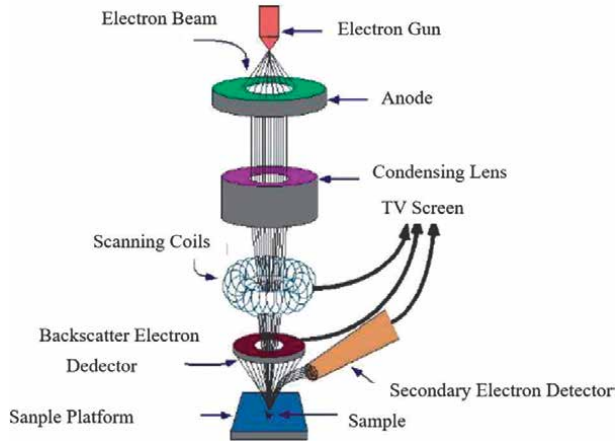


Figure 2.
Schematic view of the scanning electron microscope.

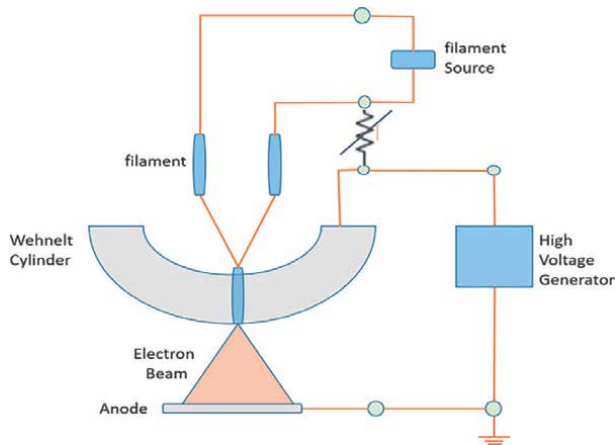


Figure 3.
Schematic view of electron gun.

3.3 Electron sources

Electron sources are widely used tungsten, LaB₆, Cold FEG, Shotky FEG [8]. The most used old model tungsten and FEG electron sources from these sources are indicated in **Figure 4** [8]. Here, tungsten filament electron source is used in older technology devices, while FEG welding is used as a more technological electron source. The advantages and disadvantages of these sources relative to each other are presented in **Table 1**. When **Table 2** is examined, it is clearly seen that FEG electron sources are more useful sources.

As can be seen from the **Table 2**, FEG pistols appear to be advantageous in many respects. In scanning electron microscopes, the most important values for the sample are magnification and resolution.

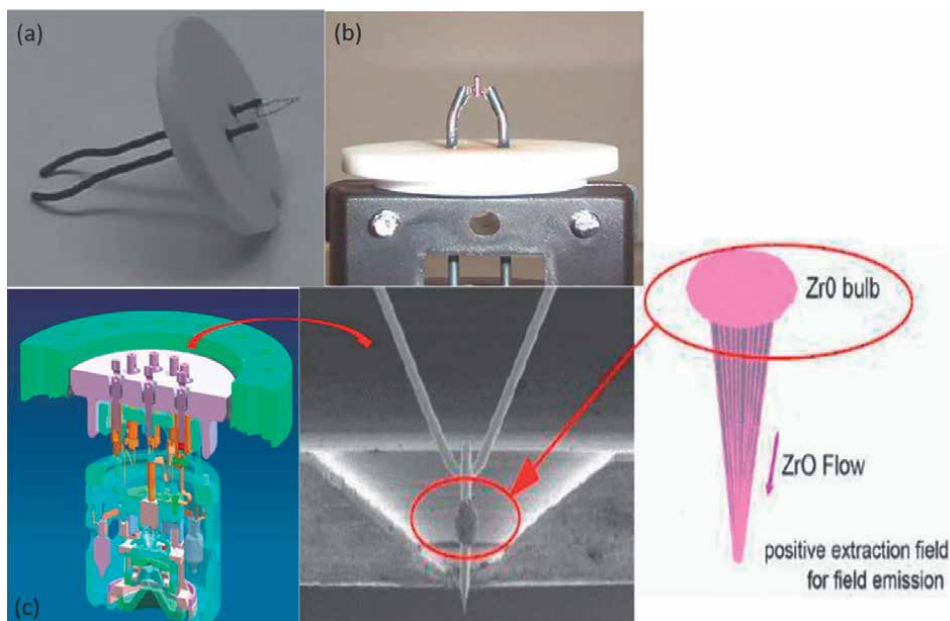


Figure 4.
 Electron sources (a) tungsten (b) FEG (c) FEG module.

| | Tungsten | LaB6 | Schottky FEG |
|-----------------------------------|-------------------|-------------------|-------------------------------------|
| Brightness (A/cm ² sr) | 100 | 1000 | 5000 |
| Energy Distribution | 3.0 eV | 1.5 eV | 0.3 eV |
| Welding Temperature (K) | ~2800 | ~1850 | ~1350 |
| Lifetime (s) | 100 | 2000+ | 10,000+ |
| Vacuum (mbar) | ~10 ⁻⁵ | ~10 ⁻⁷ | ~10 ⁻⁸ -10 ⁻⁹ |
| Resolution (30 kV) | 3 nm | <2.7 nm | <1.2 nm |
| Resolution (1 kV) | 15 nm | <12 nm | <3 nm |

Table 2.
 Comparison of electron sources.

Resolution: It expresses the power of distinguishing two different parts on the viewed surface.

Magnification: Shows the ratio of the imaged area to the scanned area.

These two values are actually a comparative situation, namely qualitative. In fact, the magnification may vary depending on the screen and print size on which it is viewed. Therefore, the main thing in microscopic images is the length bar. The resolution event, on the other hand, depends on the analysis configuration. That is, it depends on the acceleration potential, the working distance (h), the current value and the structure of the sample.

3.4 Interactions of electrons with sample

Electrons emanating from the gun strike the sample surface with an acceleration potential. Three physical events will occur for these incoming electrons. These are

back scattering, passing through scattering and elastic scattering, respectively. This situation is illustrated in **Figure 5** below.

As can be understood from here, different rays and electrons are formed as a result of the collision of electrons with the surface. Before talking about these electrons, let us look at the depth at which the incoming electrons affect the sample surface (**Figure 6**) [3].

When we look at the electron-sample interaction, shown schematically in **Figure 6**, we see that the interference is in the form of a water drop. Here, high energy electrons form low energy auger electrons as a result of inelastic interference of sample atoms with outer orbital electrons. These auger electrons contain information about the sample surface and form the working principle of auger Spectroscopy [8]. Again, as a result of the interference between the incoming electrons and the orbital electrons, the beam electrons that are thrown out of the orbit or whose energy decreases, move towards the sample surface. These electrons are called secondary electrons. These secondary electrons are collected in the scintillator in the sample chamber and converted into a secondary electron image signal. Secondary electrons come from approximately 10 nm depth of the sample surface. This provides a high resolution topographic image. In addition, inelastic interference occurs between the sample atoms and the electron beam. As a result of these inelastic interactions, characteristic X-rays and continuous radiations occur in the sample. The characteristic radiations generated here are evaluated as wavelength or energy dispersed radiation. This evaluation gives us the chemical composition of the sample, that is, the elemental analysis information. This analysis is called EDX analysis.

The electron beam on the sample also makes elastic interferences with the sample atoms. During this elastic interference, the incident electron beam is deflected by the attractive force of the nuclei of the sample atoms and backscattering occurs. These

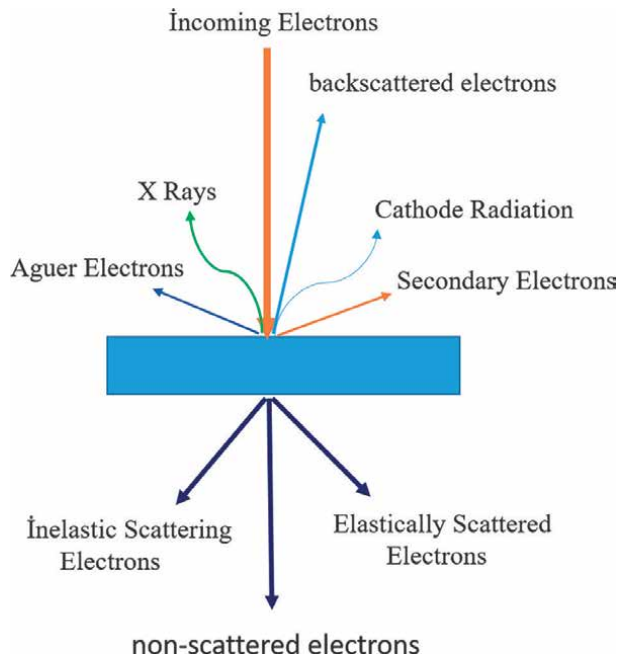


Figure 5.
Rays and electrons formed as a result of the interaction of the incoming electron beam.

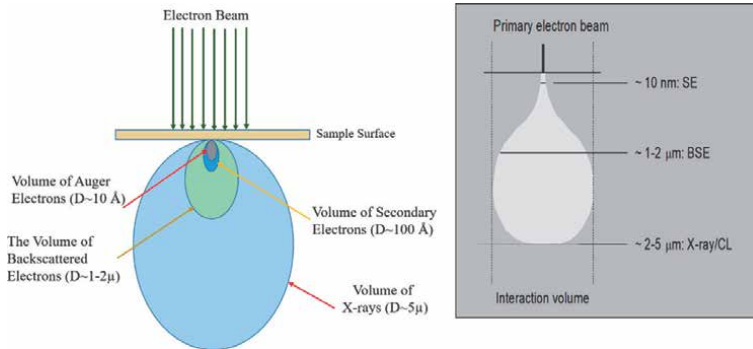


Figure 6.
 Interaction between electron beam and sample.

scattered electrons are defined as back-scattered electrons. The image formed by these backscattered electrons is called the backscattered image. Here, the amount of backscattered electrons is proportional to the atomic number of the sample. This provides atomic number dependent contrast for polyphase systems in image formation. When the signals are collected ($A + B$) in the backscattered electron detector, a compositional image depending on the atomic number contrast is obtained [7]. If the image is obtained by taking the difference of the signals here ($A - B$), a topographic composition image is formed (**Figure 7**) [7].

In summary,

Secondary Electrons:

- Caused by inelastic collision between incoming electrons and electrons in the conduction or valence band (**Figure 8a**).
- The energy of the incoming electrons is high and it removes electrons from the sample (**Figure 8b**).
- Secondary electrons are low energy electrons and can be collected with a potential between 100 and 300 V applied to the detector.

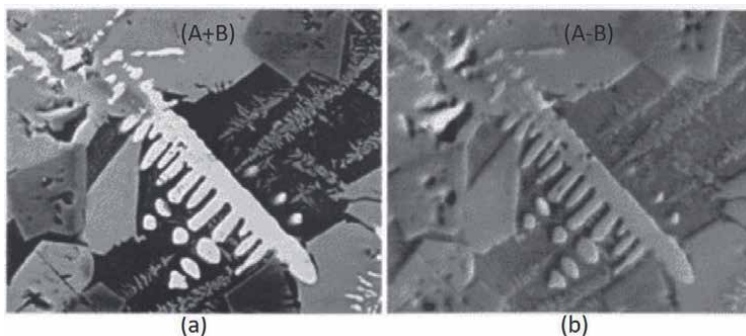


Figure 7.
 Elemental backscatter images (a) backscattered $A + B$ "composition" signal (b) backscattered $A - B$ "topographic" signal.

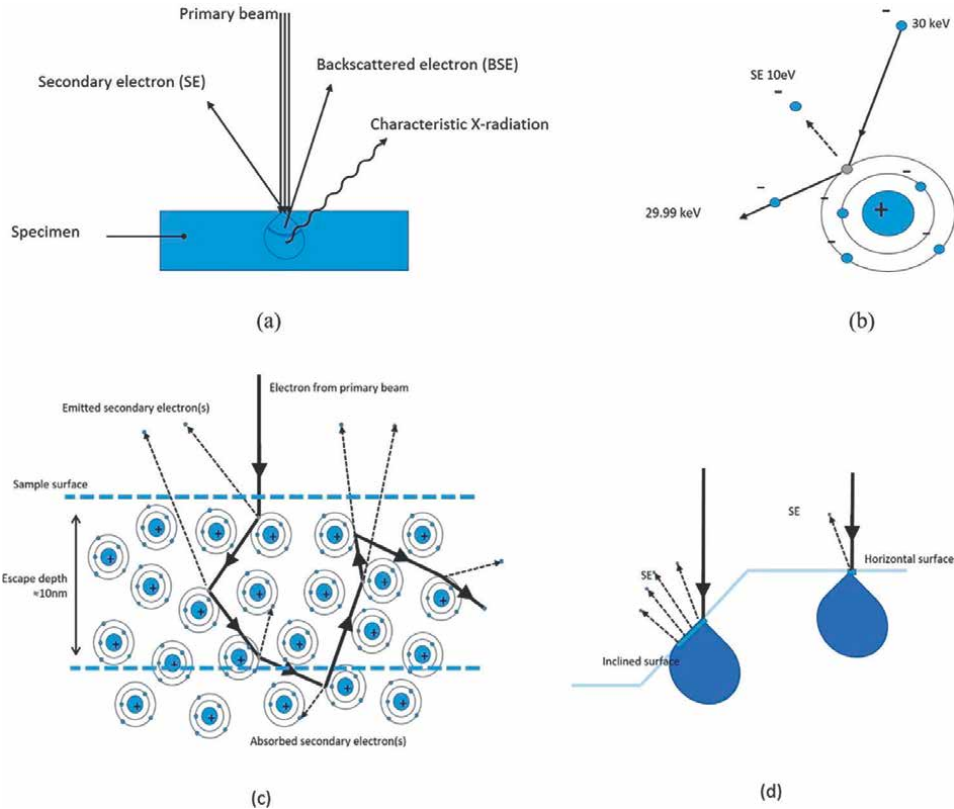


Figure 8. Schematic representation of interference patterns of secondary electrons (a) electron interaction (b) production of secondary electrons (c) formation of secondary electrons (d) effect of sloping surface on SE emission [8].

- Independent of the atomic number of the scattering atoms
- Originate from surface area < 10 nm (most from 2 to 5 nm depth)
- Contrast by topology
- Low energy electrons <50 eV (90% <10 eV)

When **Figure 8** [8] is examined, the interaction of the secondary electron with the sample surface and sample electrons is seen in a and b. Also, in c and d, we see how it interacts with the electrons that make up the sample and then leaves the sample surface.

Backscattered Electrons:

- They are formed as a result of elastic collision between incoming electrons and nuclei of sample atoms (**Figure 9b**). (Rutherford Scattering).
- The higher the atomic number of the sample atoms, the more backscattered electrons are obtained. In this way, materials with a large atomic number appear brighter (**Figure 9d**).

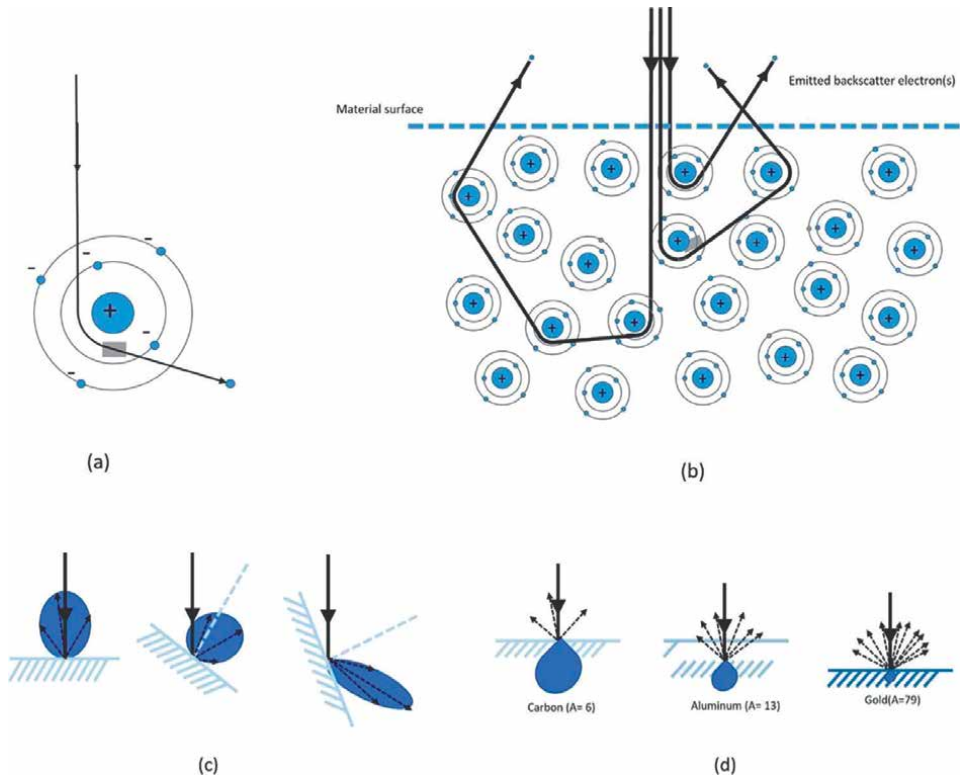


Figure 9. Schematic representation of the interference patterns of backscattered electrons. (a) Production of backscattered electrons (b) production of backscattered electrons (c) effect of inclined surface to BSE emission (d) effect of atomic number to BSE emission [8].

- Varies strongly with the atomic number Z of the scattering atoms
- Originate from deeper in the sample ($<1-2 \mu\text{m}$)
- Contrast by atomic number and topology
- High energy electrons (50 eV – 30 keV)

When **Figure 9** [8] is examined, the interaction of backscattered electrons with the sample surface and sample electrons can be seen in **Figure 9a-b**. Also, in **Figure 9c-d**, we can see how it interacts with the electrons that make up the sample, and the scattering increases as the atomic number increases.

When the backscattered electron (**Figure 10a**) and the secondary electron image (**Figure 10b**) are examined in **Figure 10** [8], different properties of the same sample surface are clearly seen. From here, it is easy to understand the detection of different phases with the BSE detector. The detection of different phases is mostly used in metallurgical materials science to easily distinguish the structures of the phases in the sample. This shows us that SEM is more than imaging.

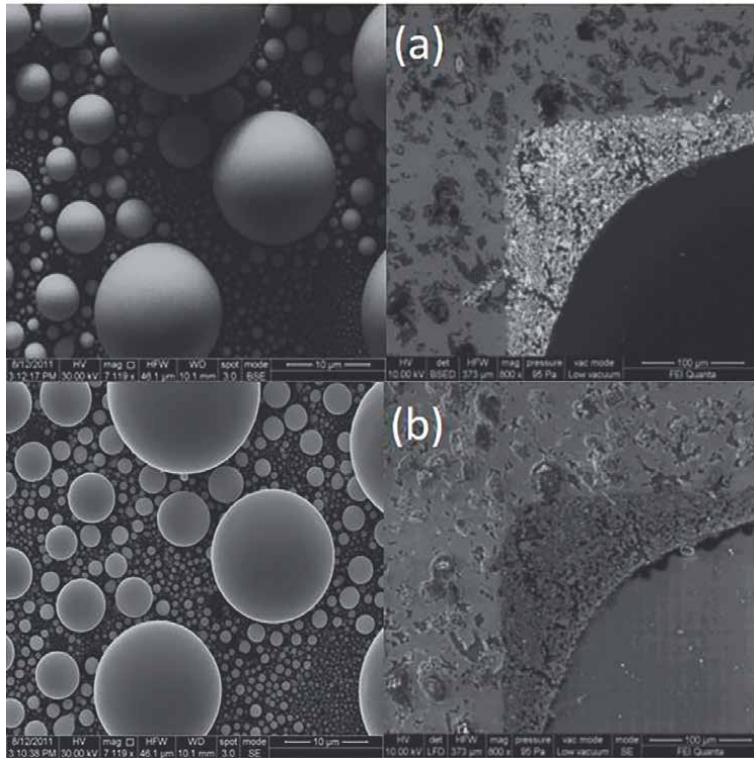


Figure 10. Topographic images taken with different detectors (a) BSE image (b) SE image [8].

4. Usage areas of scanning

Scanning Electron Microscope, besides its use in research and development studies in many branches, is widely used in microelectronics chip production, error analysis in different branches of industry, biological sciences, medicine and criminal applications. Among them,

In Forensic Medicine: It is used to compare materials such as metal parts, wood chips, paint and ink, and also to examine evidence in police laboratories by examining materials such as hair, skin pieces, thread. It is also used effectively in the fields of medicine such as Anatomy, Biochemistry, Physiology, Microbiology, Pathology, Toxicology. It is also used in fields such as dentistry, Biological Botany and Cell Biology in the field of health [5].

In metallurgy: Metals are used to determine the durability of metals in different conditions such as hot and cold [6]. Also in this field; SEM analyzes are also used in many fields such as Material Sciences (Content Analysis of Materials), Materials Research, Investigation of Rough Surfaces, Surface Topography, Investigation of Material Damages, Magnetic and Superconducting Materials, Geological Sections, Soft Materials and Crystallization/Phase Transformation.

It is used to determine the durability of metals used in aircraft, automotive, defense industry, vehicles such as aircraft, automobiles, trains, ships, which require the use of strong metal for security reasons.

In Scientific Research: Biologists study plant and animal tissues, chemists use microscopic crystals, metal, plastic, ceramics, etc. They make use of SEM in the analysis.

In addition, it is of great importance to make use of the EDX features of SEM devices for additional analysis such as sample content determination and a color mapping of this content.

5. Sample preparation

Surface images of any object imaginable can be obtained in scanning electron microscopes. To express these under two main headings, we can define them as conductor and insulator. In general, it is sufficient to have suitable dimensions in the chamber for conductive samples, while preliminary preparations are required for insulating and biological samples [5]. In general, the following factors should be considered during sample preparation.

- Sample sizes should be tailored to the SEM instrument chamber.
- The sample must be resistant to high vacuum and no outgassing.
- Care should be taken to ensure that it is clean, dust-free, spotless and oil-free.
- If possible, coating should not be done or should be done in sufficient quantities.
- Care should be taken not to deform it while placing it in the chamber with the holders.
- If there is a possibility of doubt, a control sample should also be included.
- There must be good electrical contact between the sample stub (holder) and ground potential.
- There should be good conductive contact between the sample surface and the stub.
- The sampled stub should not be prone to excessive interference with electrons. Generally, aluminum is preferred.
- Small and thin materials should be mounted on the mass foil very well to give a minimum background signal.
- The sample should be mounted in the sample holder so that it does not move.
- The rotation and inclination of the samples to be used should be of appropriate size and should be attached in a non-slip manner.

5.1 Conductive and non-conductive samples

5.1.1 Conductors

If we consider it in two groups, metals and semi-metals are included in this group. Since metals have good conductivity, not much preparation is needed.

5.1.2 Non-conductive ones

This group includes those that have no electrical conductivity at all. For example, plastics, polymers and materials with fiber properties should be considered in this category.

5.1.3 Volatile and Non-Conductive

If the sample does not contain moisture but is also a non-conductive material, that is, if it is not possible to take an image without coating, the following should be applied. Even if many materials are dry and insulating, they can cause gas to come out in high vacuum. For this reason, it is sufficient to cover the samples containing non-volatile elements and non-conductive properties with a thin layer such as Au, C, Au/Pd and Al. This layer is generally 20–30 nm thick [4, 6]. There are some reasons why we do this.

- The conductivity of the sample is increased, which minimizes the accumulation of electrons on the sample surface and minimizes the emergence of poor quality image.
- Reduces prolonged exposure to the sample surface for imaging and reduces distortion.
- Increases primary and secondary electron emission.
- It will reduce the penetration depth of electrons and cause high resolution.
- Usually gold plating is used. Among the main reasons for this are the following.
- High secondary spread co-efficient.
- High conductivity of electron and temperature.
- Non-oxidation.
- Coarse grain of sputtered particles in the surface coating.

Coatings are usually made by evaporation. If the coating is made with carbon, gold plating will be preferred since it cannot accurately analyze the amount of carbon in the sample in X-ray microanalysis. In addition, it should not be preferred too much as it will oxidize in aluminum [6].

Coated and uncoated sample images are given in **Figure 11** [8]. Since the coated sample increases the surface conductivity here, electrons from the electron gun do not cause accumulation on the surface. This provides a much more detailed and clear image of a coated sample.

5.1.4 Biological Samples

Biological samples are among the most important groups to be examined in scanning electron microscopy. These samples show some differences from the samples from other areas. This difference is due to the fact that it is a living tissue and requires different pre-processing before imaging. Chief among these,

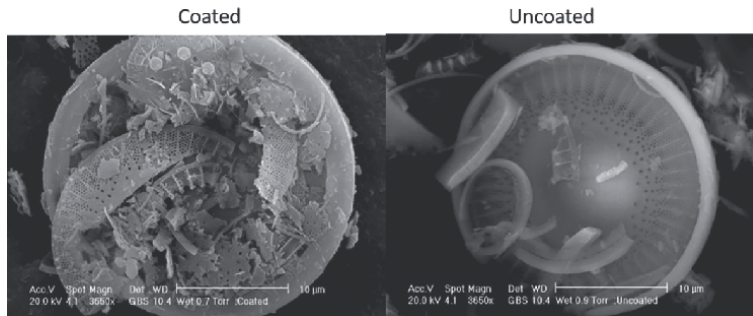


Figure 11.
Images of coated and uncoated samples.

A. Fixation: The fixation time and temperature are different from tissue to tissue.

- Primary fixation is done with Glutaraldehyde.
- Washing: It is done with tampons. At this stage, Sorrenson Buffer Phosphate solution is used.
- Secondary fixation: The sample is kept in a solution up to 10 times its volume with osmium tetroxide.
- For example, if it is soft and has a high oil content, it causes it to darken.
- The hardness of the tissue allows it to take less amount of osmium tetroxide.

B. Dehydration: Ethyl alcohol, acetone, amyl acetate series are used. It is gradually passed from low concentration to high concentration. The percent concentration is determined according to the sensitivity of the sample. The concentration range is narrow in soft samples and wide in hard samples. In addition, it is kept in each series for at least 15–20 minutes.

C. Drying: The drying time varies according to the ambient temperature and sample size. Critical desiccant should be used on sensitive tissues. With this method, acetone, ethanol or amyl acetate in the tissue and liquid CO₂ are replaced at the critical point (35 Co and 1100 Bar). Here, while the liquid CO₂ evaporates from the liquid state, the tissue is dried without spoiling. Drying should be done with whatever substance our sample was dehydrated with [5]. In hard tissues such as bone and teeth, air drying is preferred.

In **Figure 12** [10], we see a photo of a wet sample with moisture taken in SEM. Here we see a much clearer view of the sample dried with the critical dryer. This shows how important the sample preparation process is.

5.2 Dimensions to be examined

Scanning electron microscopes are manufactured in a certain size in that they are high-tech and have electron guns and magnetic deflectors on them. Therefore the

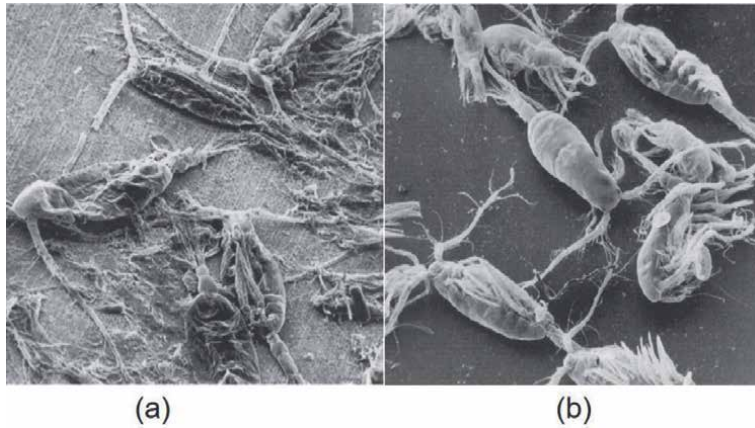


Figure 12.
SEM image of a wet sample (a) natural dried (b) critical dryer dried.

Maximum dimensions of the sample to be imaged

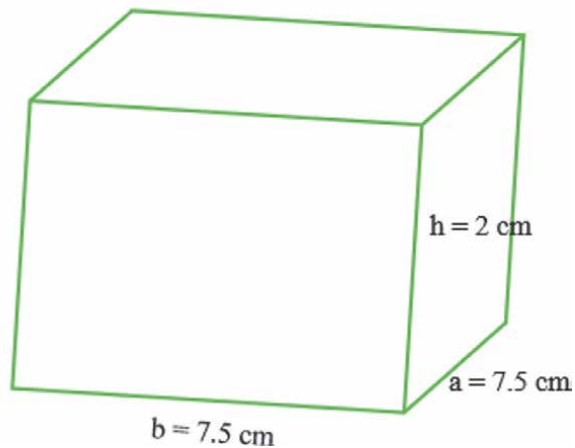


Figure 13.
Schematic representation of sample size suitable for SEM device.

sample chamber has a certain volume. Rotation and angulation in the sample chamber also limits the width, length, and height of the sample. Therefore, the maximum width and maximum height are limited to 7.5 cm. In addition, the maximum height of the sample can be at most 2 cm. However, in some SEM devices, the sample holders can be removed and the height can be increased up to 5 cm. Since this situation is not valid for all samples, the sample height should be accepted as 2 cm as a standard. Representative dimensions are shown in **Figure 13**.

6. Conclusion

Knowing better the mysterious world we live in will be in the light of science. Humanity first wonders about this light and develops the necessary equipment to satisfy this curiosity. SEM devices have been one of these lights in the better

understanding of human beings in this micro and nano world. In this part of our book, the origin story of the scanning electron microscope device, its necessity and usage areas are examined. In these examinations, from which areas and for what purposes SEM is used to how it performs imaging has been examined. As a result of this examination, SEM devices not only shed light on scientific studies, but also show in detail the quantities in our daily life that we cannot see with the naked eye. Its wide range of use and its ease of use necessitate use in all fields of science. In other words, human beings have eyes in every field, from a cell tissue to a hair strand or from a clay powder to a computer circuit. SEM can show us all the details that we can see today.


Author details

Cengiz Temiz

Electronics and Automation Department, Zonguldak Bulent Ecevit University, Alaplı Vocational School, Zonguldak, Turkey

*Address all correspondence to: cengiztemiz60@gmail.com

IntechOpen

© 2022 The Author(s). Licensee IntechOpen. This chapter is distributed under the terms of the Creative Commons Attribution License (<http://creativecommons.org/licenses/by/3.0>), which permits unrestricted use, distribution, and reproduction in any medium, provided the original work is properly cited. 

References

- [1] Singh A, Verma R, Murari A, Agrawal A, Singh S, Singh V. Electron microscope: A review. *Medico-Legal Update*. 2013;**13**:12-16. DOI: 10.5958/j.0974-1283.13.2.004
- [2] Kapakin Terim KA. Scanning Elektron Mikroskopy. *Journal of Yüzüncü Yıl University Faculty of Veterinary Medicine*. 2006;**17**:55-58
- [3] Vernon-Parry KD. Scanning electron microscopy: An introduction. *III-Vs Review*. 2000;**13**:40-44. DOI: 10.1016/S0961-1290(00)80006-X
- [4] Temiz C, Yılmaz F, Kölemen U. Investigation of microstructures and mechanical properties of Sc-doped Al-5Cu alloys. *Journal of Gazi University Faculty of Engineering and Architecture*. 2022;**37**:75-88. DOI: 10.17341/gazimmfd.855196
- [5] Mungan C. Evaluation of Fixation Potential of Aldehyde Group Fixatives under Super Resolution Microscope with Immunofluorescence Technique [Thesis]. Ankara: Ankara University Biotechnology Institute; 2019
- [6] Temiz C. Mechanical Characterization of Al-5Cu-XSc (X=0,5 and 1,0) Alloys Production by Using Induction Melting and Melt Spinning Techniques [Thesis]. Tokat: Tokat Gaziosmanpasa University Graduate School Of Natural And Applied Sciences; 2019
- [7] Xin HL, Varat I, David AM. Depth sectioning of individual dopant atoms with aberration-corrected scanning transmission electron microscopy. *Applied Physics Letters*. 2008;**92**(1):013125. DOI: 10.1063/1.2828990
- [8] FEI Company Tools for Nanotech. [Internet]. 2013. Available from: www.fei.com/www.anatek.com.tr [Accessed: January 18, 2013]
- [9] Richard BC et al. *Encyclopedia of materials characterization: Surfaces, interfaces, thin films*. Gulf Professional Publishing. 1992:65-87
- [10] Can A. Ankara University Biotechnology Institute scanning electron microscopy sample preparation and investigation methods. Graduate Lecture Notes ppt. 2006

Chapter 2

Minerals Observed by Scanning Electron Microscopy (SEM), Transmission Electron Microscopy (TEM) and High Resolution Transmission Electron Microscopy (HRTEM)

Taitel-Goldman Nurit

Abstract

Pictures from a scanning electron microscopy, transmission electron microscopy and high resolution microscopy are presented. Samples were collected from the marl layer in Judean Mountains in Israel, and the minerals observed were dolomite, calcite, goethite, and K-feldspar. In sands along the Mediterranean Seashore and the coastal plain in Israel, dark grains were rich in Ti, and quartz grains were covered by clays and hematite. Dust samples included clay minerals, Ti and Fe oxides. Iron oxides (goethite, akaganéite and lepidocrocite) were preserved within halite crystals at the Dead Sea area. In the Atlantis II and Thetis Deeps, in the central Red Sea, hot brines feel the deeps and minerals found in cores were magnetite, goethite, ferroxhyte, manganite, todorokite, groutite and short range ordered ferrihydrite and singerite. Observation by electron microscopy enables us to see the size of euhedral or unehedral phases. Relations between the minerals are observed. Point analyses yield the chemical composition of the mineral with impurities, and Electron diffraction identifies the crystallography of the minerals.

Keywords: natural Fe, Ti, Mn oxides, quartz grains, euhedral, dolomite and K-feldspar

1. Introduction

The use of electron microscopy enables us to observe the size of minerals and understand their formation and the relations between various minerals in sediments. By using scanning electron microscopy (SEM), the size of minerals can be measured, morphology and relations between phases like coating or erosion of crystals can be observed. Using energy dispersive systems (EDS), the chemical composition of minerals can be obtained. The use of transmission electron microscopy (TEM) or high resolution transmission electron microscopy (HRTEM) enables us to measure the size of nanocrystals, obtain their chemical composition and identify the minerals formed.

With HRTEM, short range ordered phases can be identified and recrystallization of the minerals preserving initial morphology can be observed [1].

In this chapter, samples from various sites from Israel and the central Red Sea Deeps are presented and described. Rounded quartz grains arrive from the Nile River in Egypt to the Nile Delta, then are moved from the Delta with longshore current along the southeastern Mediterranean Sea to the Israeli coast. Moving of the grains to the coastal plain results from transgression and regressions of the sea causing the formation of sandstone ridges and soils [2]. The sand was also blown inland, forming sand dunes and eolianite calcareous sandstones ('kurkar').

Carbonate layers and marl or clay layers were formed during the Cretaceous period transgression of the Thetis Ocean. At the end of the Cretaceous, the layers were folded as part of the Syrian arc and the Judean Mountains were formed [3]. The maximum elevation of 1000 m separates between the western side of the mountains and the Judean desert on the eastern side.

The hypersaline terminate lake of the Dead Sea is located along the Dead Sea Transform fault at the eastern side of the Judean Mountains. The desert in the area causes evaporation of the Dead Sea water leading to elevated salinity of 340 g/l and precipitation of halite crystals [4].

Dust storms are common in Israel, mainly during autumn and spring. During the winter, dust storms appear at the early stage of rainstorms. The dust arrives either from North Africa from the Sahara desert or Saudi Arabia, depending on the weather cyclones [5]. The dust contains coarse silty quartz grains sourced from Sinai and the Negev in southern Israel [6].

The Atlantis II and Thetis Deeps are located in the central part of the Red Sea along the axial rift separating the Arabian and African plates. Hydrothermal brine discharges into the Deeps and the salinity results from dissolution of Miocene evaporates [7]. Elevated temperature results from interaction with hot magmatic and peridotite rocks, located underneath. Dissolved iron that is discharged from ultrabasic magmatic rocks, reacts with oxygen to form various phases of iron oxides. A narrow channel connects the southern Atlantis II Deep with small chain and discovery basins [8]. Drillings were performed during 'Mesada 3' expedition by Peussag company from Germany in the late 1970s and at the beginning of the 1980s as a part of the 'Saudi Sudanese Red Sea joint commission for exploring of red Sea Resources'. Samples were kept under 4°C in institut für meeresforschung (IFM) Geomar in Kiel, Germany [9].

2. Analysis of minerals

2.1 Mediterranean seashore sample

A sample from the southern part of the Mediterranean seashore was observed using scanning electron microscopy (SEM). The grains consist of transparent quartz grains (SiO₂) and black grains (**Figure 1**). The black grains were separated and checked using SEM and energy dispersive systems (EDS). It appears from the chemical analyses that these black grains are composed mainly of Ti-oxides.

2.2 Judean Mountains samples

Samples from the Judean Mountains in Israel were collected from layers of marl or clay. The samples were chipped or broken. The fresh surface was gold-carbonate

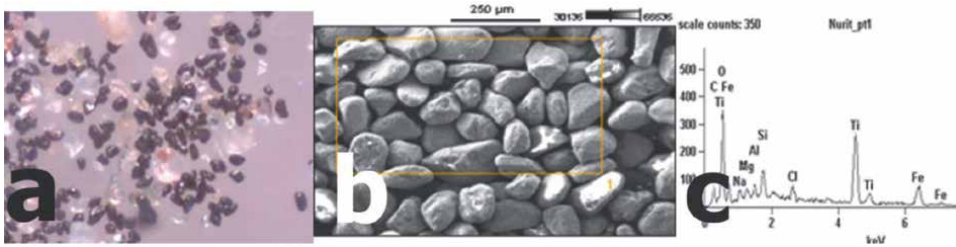


Figure 1.
(a) Observation under the magnifying glass of sand from the southern part of the Israeli coast had transparent quartz grains and black grains, (b) SEM image of the black grains, and (c) chemical analyses of the black grains obtained by EDS, showing clays and Ti-oxide with iron impurity.

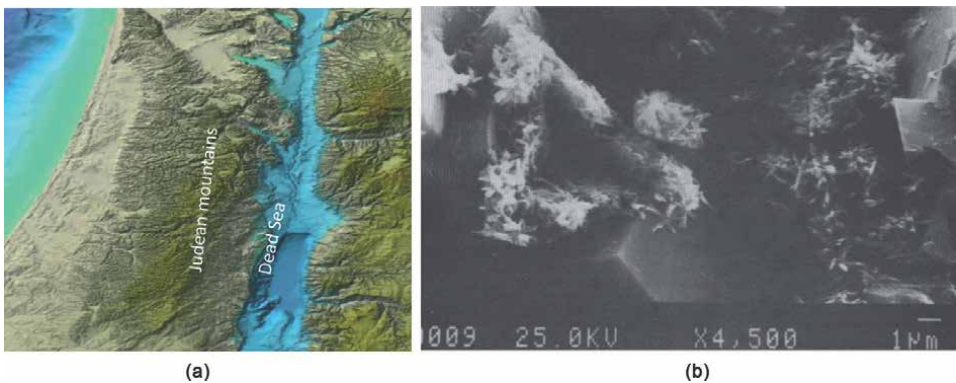


Figure 2.
(a) Map of Israel with Judean mountains and the Dead Sea, and (b) SEM image of dolomite and goethite crystals from the Judean Hills in Israel.

coated for back-scattered mode on SEM and the chemical composition was established with EDS. By observing the samples, newly-formed minerals were identified by their euhedral morphology. Crystals of dolomite ($\text{CaMg}(\text{CO}_3)_2$) were identified

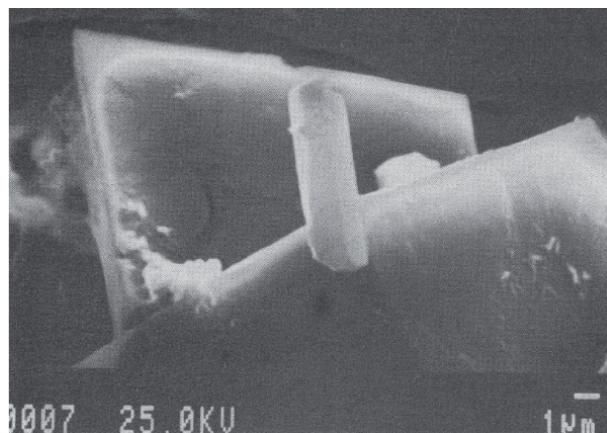


Figure 3.
SEM image of idiomorphic shape of K-feldspar on euhedral dolomite crystals in marl layers of the Judean Hills in Israel.

in the argillaceous strata of the Judea group in the Judean Hills (**Figure 2**). The euhedral morphology indicates that they were formed in the marl layer. Goethite (FeOOH) crystals were formed later, filling the open spaces between the dolomite crystals.

In the marl layer K-feldspar, probably orthoclase or adularia (KAlSi₃O₈), was formed on euhedral dolomite crystals (**Figure 3**). Euhedral morphology of the K-feldspar indicates that it was formed in situ after dolomite crystallization [3]. Finding autogenic K-feldspar in the marl layers enabled measurement of the age of the layers [10].

Some of the dolomites in the Judean Hills were dissolved due to exposure to rains (**Figure 4**). The inner part was dissolved probably due to initial crystallization of dolomite with Ca/Mg > 1. As the dolomite crystallization continued, the outer part had a ratio of Ca/Mg = 1 so the dolomite was more stable. The dissolved inner part was later filled with calcite and clay minerals.

Crystallization of calcite (CaCO₃) along with clay minerals formed by agglutination of cyanobacteria caused formation of a tube (**Figure 5**).

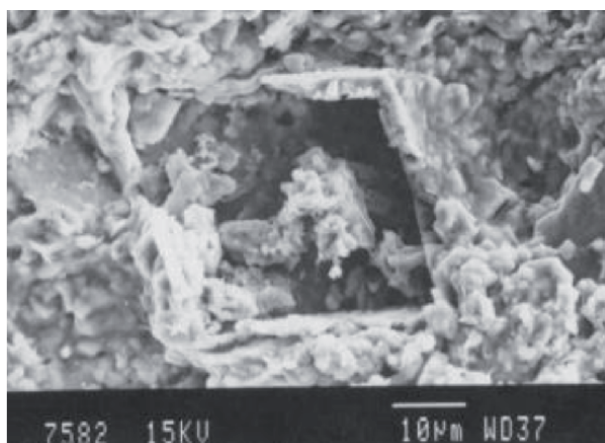


Figure 4.
SEM image of dolomite with inner part dissolved and outer part remained stable.

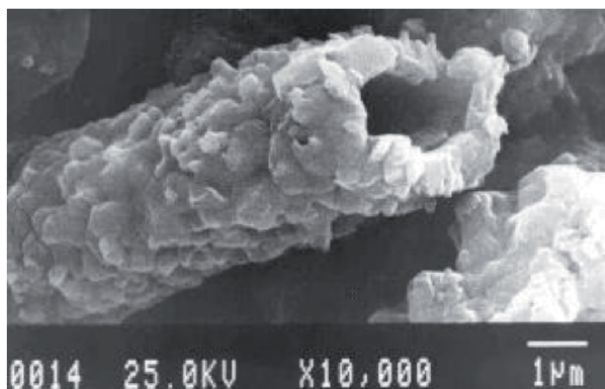


Figure 5.
SEM image of tube morphology of calcite and clays indicates biogenic origin and formation by cyanobacteria.

2.3 Samples from Red Sea deeps

Samples were collected from cores in the Atlantis II and Thetis Deep from the central Red Sea [9]. The sediments there were formed in a highly saline hydrothermal environment. Magnetite (Fe_3O_4) crystals were studied using SEM. They crystallized in the Thetis Deep located in the central Red Sea (**Figure 6**). Needles of goethite precipitate close to the magnetite. Point analyses measured on the magnetite yielded $\text{Si}/\text{Fe} = 0.01$ and impurities of V with $\text{V}/\text{Fe} = 0.002$ and Mn with $\text{Mn}/\text{Fe} = 0.002$.

Foraminifera's shells that originate from the upper part of the Red Sea sink and attach to the magnetite crystals.

Nano-sized particles (5–200 nm) were checked under transmission electron microscopy (TEM) using JEOL JEM-2100f analytical TEM operated at 200 kV, equipped with a JED-2300 T energy dispersive spectrometer (EDS) for microprobe elemental analyses. All chemical analyses were obtained by point analysis with a beam width of 1 nm JEOL. Crystalline phases were identified, using selected area electron diffraction (SAED) in the TEM.

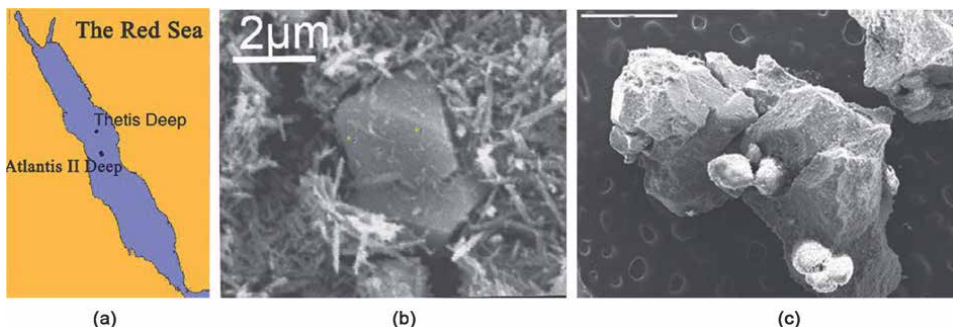


Figure 6. (a) Location of the Thetis deep and Atlantis II deep in the Red Sea, (b) SEM image of euhedral magnetite crystals surrounded by goethite crystals, and (c) SEM image of magnetite crystallized in the Thetis deep in the Red Sea with foraminifer's shells.

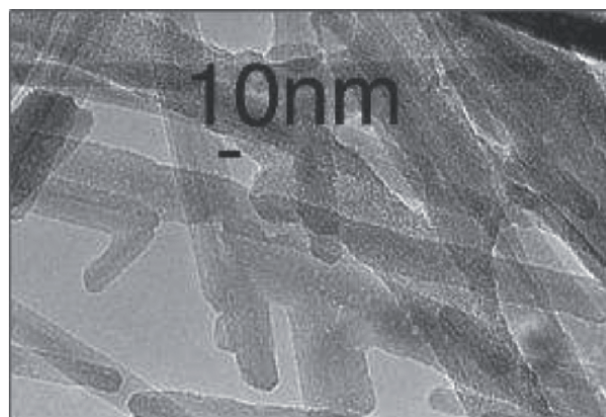


Figure 7. TEM image of mono-domain goethite with twinning from the Red Sea deeps due to elevated temperature. Goethite had an impurity of Si/Fe 0.02 atomic ratio.

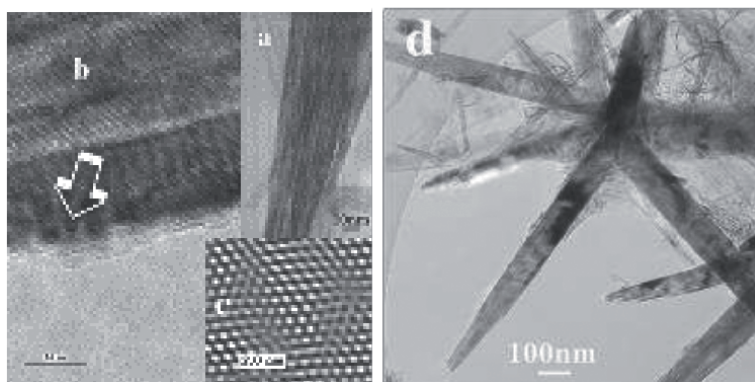


Figure 8. (a) HRTEM image of multi-domain goethite, (b) HRTEM image of the goethite, (c) fast Fourier transformation that shows the well-crystallized goethite, and (d) TEM image of goethite with twinning forming a star shape impurity of Si/Fe 0.04 atomic ratio.

Samples that were crystallized in the Red Sea Deeps had various morphologies due to salinity of the hydrothermal brines and their high temperature. Goethite (α -FeOOH) appears as mono-domain with twinning (**Figure 7**) or as multi-domain (**Figure 8**) and by high resolution, it is possible to observe well-crystallized phases. Impurity of Si in the goethite crystals was observed within the crystals: Si/Fe = 0.1 in multi-domain phase and Si/Fe = 0.02 in mono-domain structure. Star shape had Si/Fe = 0.04. Crystallization of goethite occurred at the upper part of the hydrothermal brine due to iron that discharges from the Deep and oxygen from Red Sea deep water.

Tiny goethite crystals grow on groutite (α MnOOH) in a sample from the southern part of the Atlantis II Deep in the Red Sea [11]. Groutite and goethite are iso-structural; hence crystallization of goethite was favored (**Figure 9**).

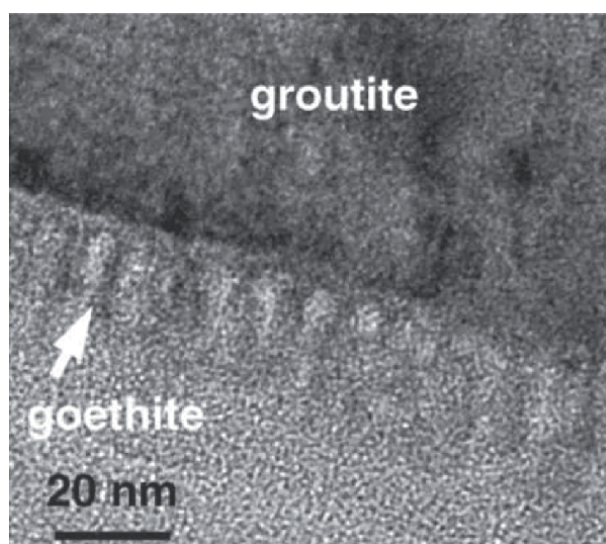


Figure 9. HRTEM image of goethite crystallized on groutite.

2.4 Samples from Dead Sea area and the Red Sea

In the Dead Sea area, colored halite can be observed with iron oxides preserved within halite crystals. Samples were studied using HRTEM [12]. Multi-domain akaganéite (β -FeOOH) (**Figure 10**) and multi-domain lepidocrocite (γ -FeOOH) (**Figure 11**) were crystallized in the area of the Dead Sea and then covered by halite crystals that preserved the initial phases.

Formation of akaganéite requires the presence of Cl^- ions, which had Si and Mn impurities ($\text{Si}/\text{Fe} = 0.06$, $\text{Mn}/\text{Fe} = 0.06$).

Lepidocrocite is crystallized at slow oxidation at $\text{pH} > 5$ and in the presence of chloride [12]. Plate morphologies of lepidocrocite were observed in Atlantis II and Discovery Deep sediments in the Red Sea. Rod morphology was observed in sediments of the Thetis Deep in the Red Sea [9].

Formation of ferroxhyte (δ -FeOOH) requires high oxidation conditions [13]. Ferroxhyte was crystallized at the transition zone between the Red Sea deep water and the hydrothermal saline brine. Sample was collected from the upper part of sediments in the south-west basin of the Atlantis II Deep in the Red Sea. Ferroxhyte

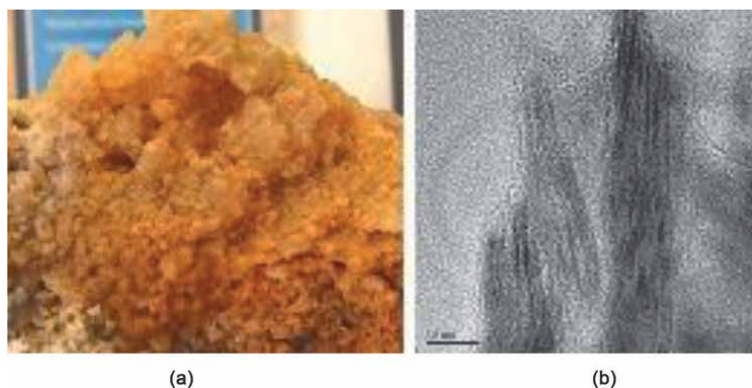


Figure 10. (a) Halite crystals from the Dead Sea area that include iron oxides, and (b) HRTEM image of multi-domain akaganéite (β -FeOOH) it contributes to the color of halite.

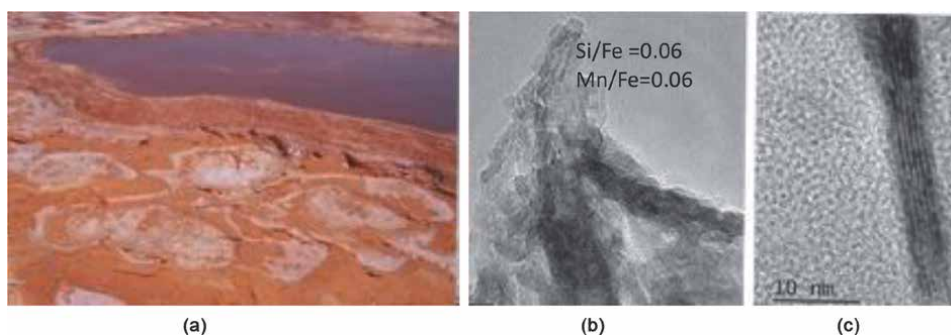


Figure 11. (a) Dead Sea area close to the seashore with halite that precipitates from the lake, (b) TEM image of lepidocrocite crystals that cause the color of the halite. Lepidocrocite crystals had impurities of $\text{Si}/\text{Fe} = 0.06$ and $\text{Mn}/\text{Fe} = 0.06$, and (c) HRTEM image of lepidocrocite preserved in the halite crystals.

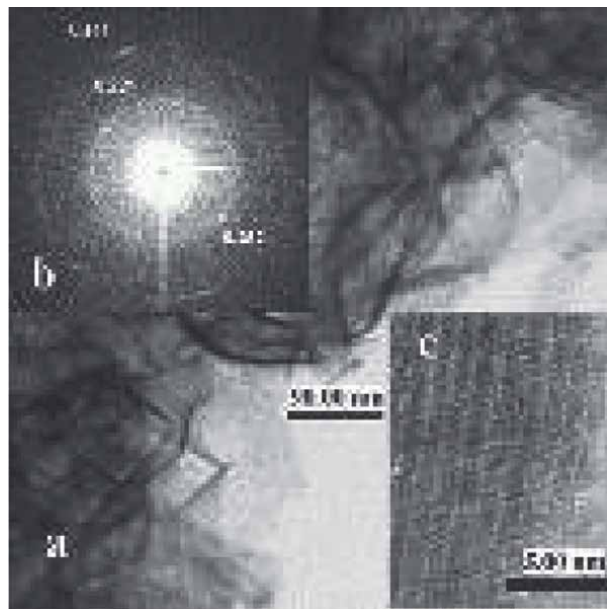


Figure 12. (a) HRTEM image of folded layers of ferrosxyhyte from the sediments of the Atlantis II deep, (b) Electron diffraction of ferrosxyhyte, and (c) HRTEM image shows a well-crystallized phase without dislocations.

appears as folded layers and a high resolution image shows that there are no dislocations in the crystals (**Figure 12**).

In the southern part of Atlantis II Deep in shallow water, Mn oxides were formed from the upper part of the brine. Minerals identified were todorokite $(Ca,Mg)_{1-x}Mn^{4+}O_{12} \cdot 3-4H_2O$, with impurities of $Si/Mn = 0.15$, $Fe/Mn = 0.28$. Manganite γ - $MnOOH$ had also an impurity of $Si/Mn = 0.10$ and $Fe/Mn = 0.20$ (**Figure 13**).

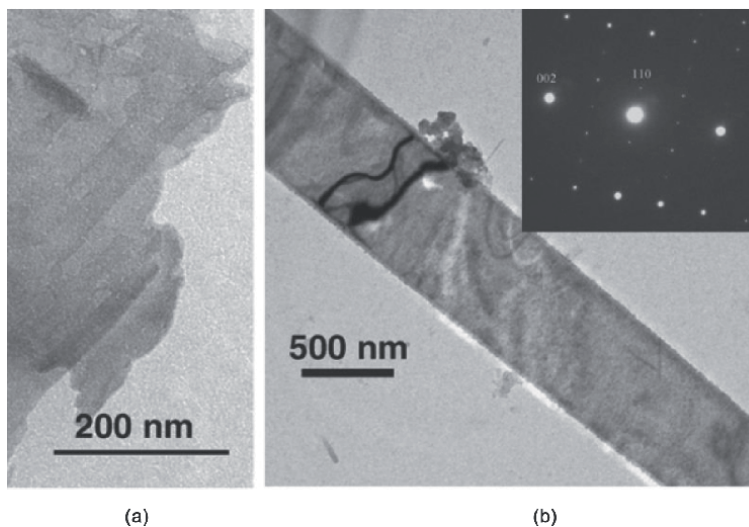


Figure 13. TEM images of Mn oxides from the southern part of the Atlantis II deep with Fe and Si impurities. (a) Todorokite $(Ca,Mg)_{1-x}Mn^{4+}O_{12} \cdot 3-4H_2O$, and (b) manganite γ - $MnOOH$, with electron diffraction.

Similar phases were also identified in the Chain and Discovery Deeps close to the Atlantis II Deep in the Red Sea [11].

2.5 Samples from the coastal plain of Israel

Quartz grains are dominant in soils on the coastal plain of Israel. Clay minerals, kaolinite ($\text{Al}_2\text{Si}_2\text{O}_5(\text{OH})_4$), montmorillonite ($(\text{Al}_2\text{Mg}_3\text{Si}_4)_n(\text{OH})_2n\text{H}_2\text{O}$), which arrive in the area as dust storms, cover the well rounded quartz grains. Iron oxides, mainly hematite (Fe_2O_3) crystals, are attached to the clay minerals and contribute to the red color of the red sandy soils (**Figure 14**).

2.6 Dust samples of Israel

Dust storms are common in Israel, (**Figure 15**). Dust samples were collected and studied with TEM. Most of the samples contain clay minerals, mainly montmorillonite, kaolinite and small amounts of illite. Nano-sized iron and titanium oxides are

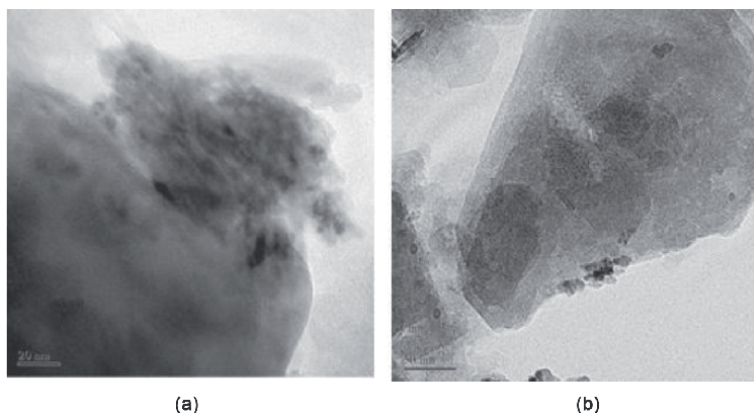


Figure 14. (a and b) TEM images of rounded quartz grains covered by kaolinite and hematite in red sandy soil.

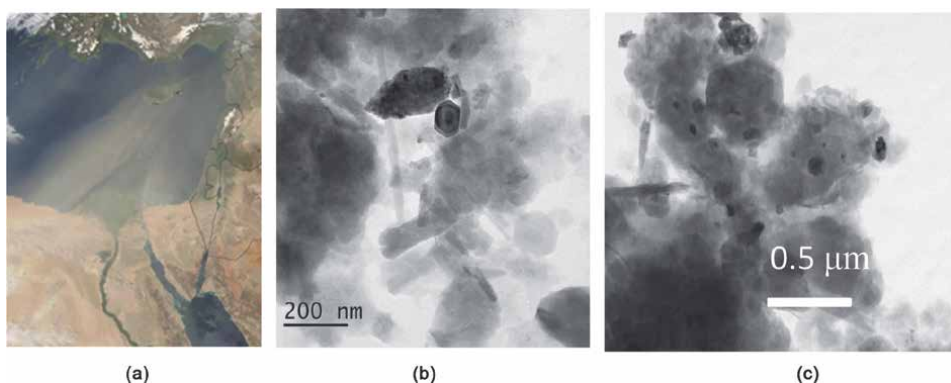


Figure 15. (a) Dust storm in the Middle East, (b) TEM image of well-crystallized rutile that was identified in the dust along with clays and hematite, and (c) HRTEM image of dust samples made of clay minerals mainly montmorillonite and kaolinite. Hematite, ilmenite and Ti oxides are attached to the clays.

attached to the clay minerals forming clusters. The dust also covers quartz grains in sand dunes along the Mediterranean seashore and colors them into darker colors.

2.7 Short range ordered phases

HRTEM enables observation of short range ordered phases. Ferrihydrite ($\text{Fe}_5^{3+}\text{HO}_8 \cdot 4\text{H}_2\text{O}$) and singerite ($\text{SiFe}_4\text{O}_6(\text{OH})_4 \cdot \text{H}_2\text{O}$) were observed using HRTEM. The size of the ferrihydrite is around 5 nm in samples from the Atlantis II Deep and it has a hexagonal outline. Ferrihydrite from the Dead Sea forms clusters. In both samples, the use of high resolution enables us to see that the phase is short range ordered (**Figure 16**).

Formation of Ferrihydrite is at fast oxidation and $\text{pH} > 2$. Si serves as an impurity in the phase. With time, ferrihydrite can recrystallize into more stable iron oxides like hematite, akaganéite or goethite (**Figure 17**).

In the upper layer of sediments of the Atlantis II Deep in the Red Sea, a new short range ordered phase was observed using HRTEM. The new phase has disc morphology with well-crystallized margins and short range ordered inner part and it was named singerite ($\text{SiFe}_4\text{O}_6(\text{OH}_4 \cdot \text{H}_2\text{O})$) (**Figure 18**) [14]. Singerite was formed by mixing of the highly saline hydrothermal brine that discharges into the Deep and Red Sea

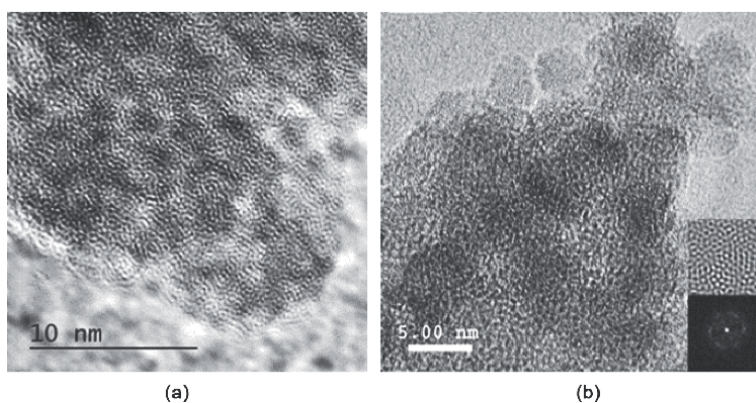


Figure 16. (a) HRTEM image of short range ordered ferrihydrite from the area of the Dead Sea, and (b) HRTEM image of ferrihydrite from Atlantis II deep with electron diffraction and fast Fourier transformation obtained by digital micrograph (Gatan) software.

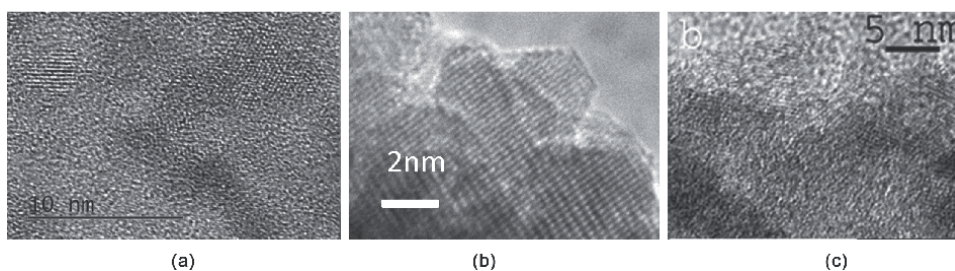


Figure 17. HRTEM images of samples from the Dead Sea area formed by recrystallization of ferrihydrite: (a) well-crystallized hematite, (b) well-crystallized akaganéite, and (c) well-crystallized goethite.

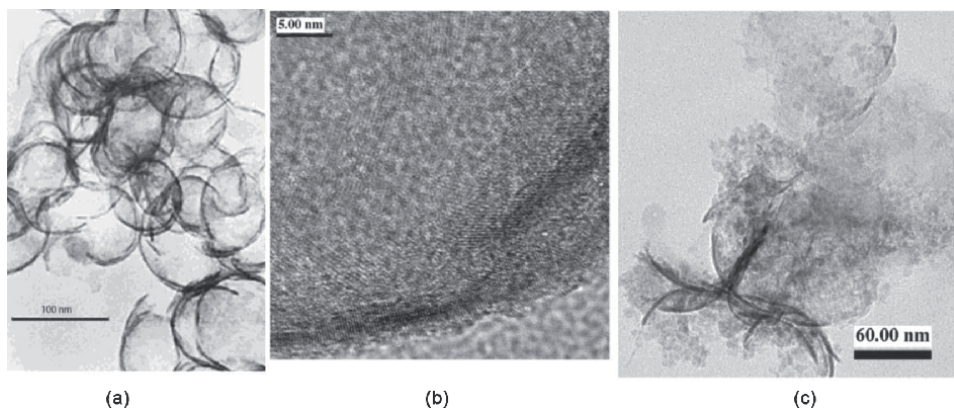


Figure 18. (a) HRTEM image of a cluster of rounded plates from the Atlantis II deep, Red Sea, (b) high resolution image of singerite with well crystallized outer part and short range ordered inner part, and (c) HRTEM image of recrystallization of singerite into clay mineral, probably nontronite.

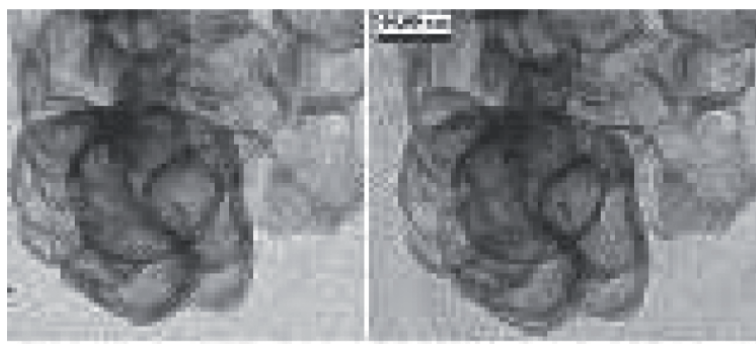


Figure 19. HRTEM image of a cluster of singerite. A small tilt of the sample enables us to see that singerite is made of rounded plates.

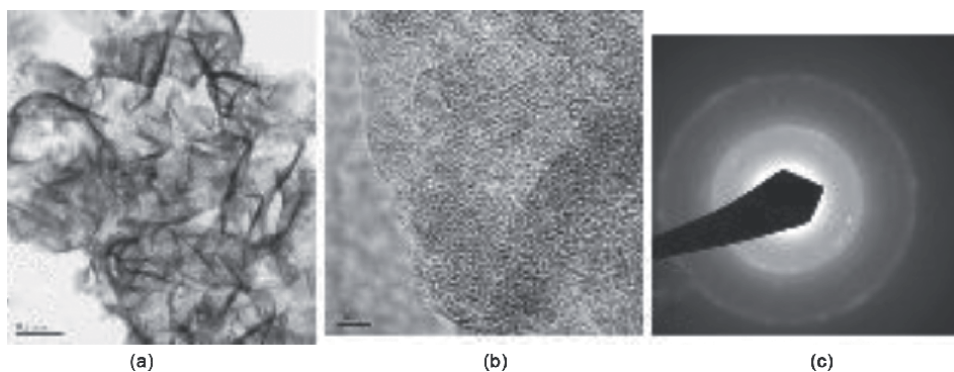


Figure 20. (a) HRTEM image of a cluster of mineraloid of Si, Fe Mn oxyhydroxide, (b) HRTEM image showing short range ordered phase, and (c) Electron diffraction shows values of 0.255, 0.22 and 0.149.

deep water. With time, singerite recrystallizes into clay minerals, usually nontronite (iron-rich smectite). Hence singerite was found only in the upper layer of sediments in the Deeps. A similar rounded phase was synthesized under saline hydrothermal conditions [9].

A small tilt of the singerite sample enables us to see that singerite is a round plate (**Figure 19**).

A new short range ordered phase from Red Sea deeps: Mn-singerite?
 $\text{Si}(\text{Fe},\text{Mn})_4\text{O}_6(\text{OH})_4\text{H}_2\text{O}$ electron diffraction yielded 0.255, 0.22 and 0.149 (**Figure 20**).

3. Discussion

Observation of minerals under electron microscopy enables observation of well-crystallized phases, study of their chemical composition and finding of impurities in the crystals by using point analyses. Under HRTEM nano-sized short range ordered phase like ferrihydrite and singerite can be observed. A new phase Mn-singerite was also observed under HRTEM. Observation of twinning that results from the conditions in which the crystals were formed, such as salinity, pH, temperature, contributes to understanding the conditions in which formation of crystals occurred. Goethite for example appears as mono-domain, multi-domain crystals or twinning creating star shape morphology. Identification of the crystallography of the minerals observed was used by electron diffraction in transmission electron microscopy. Well-crystallized minerals with euhedral morphology indicate that they were formed in situ like samples covered by halite in the Dead Sea area. It is also possible to see the initially formed dolomite minerals and later another phase, goethite, filling the open space or attached to the initially formed phases. Goethite is also crystallized on groutite since both are isostructural.

Rounded morphology is formed due to pounding as the minerals moved from their initial location where they had crystallized to the new site. Quartz grains were observed along with Ti-rich minerals with rounded morphology as well. Other rounded quartz grains were observed in red sandy soils. Using electron microscopy enables us to see Nano-size phases that form a cluster of different minerals like clusters of dust. Clays are the main phases and iron or titanium oxides are captured between the clay layers or are adsorbed on their surfaces.

4. Conclusion

In this chapter Fe-oxides, Mn-oxides, Ti-oxides, quartz, dolomite, clays and K feldspar were studied using various electron microscopies (SEM, TEM and HRTEM). Using these methods helped to identify the crystallography, morphology and chemical composition of the minerals. Nano-sized short range ordered phases like ferrihydrite and singerite were also observed and identified.

Acknowledgements

Thanks to the Hebrew University of Israel for funding part of the research.

Thanks to Vladimir Ezersky from Ilse katz institute in Ben Gurion University in Israel for using TEM and HRTEM.


The research of the Dead Sea was supported by the Open University grant no. 100975.

Author details

Taitel-Goldman Nurit
The Open University of Israel, Raanana, Israel

*Address all correspondence to: nurittg@hotmail.com

IntechOpen

© 2022 The Author(s). Licensee IntechOpen. This chapter is distributed under the terms of the Creative Commons Attribution License (<http://creativecommons.org/licenses/by/3.0>), which permits unrestricted use, distribution, and reproduction in any medium, provided the original work is properly cited. 

References

- [1] Nurit T-G. Recrystallization Processes Involving Iron Oxides in Natural Environments and in Vitro, INTECH Recent Developments in the Study of Recrystallization. In: Wilson P, editor. 2013. pp. 163-174. ISBN: 978-953-51-0962-4
- [2] Arieh S. The Soils of Israel. Berlin Heidelberg: Springer-verlag; 2007
- [3] Nurit T-G, Lisa H-K, Eytan S. Clay minerals and feldspars in argillaceous strata of the Judea Group in the Jerusalem Hills. *Israel Journal of Earth Science*. 1995;44:71-79
- [4] Avraham S, Amitai K. The story of saline water in the Dead Sea rift – The role of runoff and relative humidity. In: Garfunkel Z, Ben Avraham Z, Kagan E, editors. *Dead Sea Transform Fault System: Reviews* Springer. Dordrecht, Heidelberg, New York, London: Springer; 2014. pp. 317-353
- [5] Ganor E, Foner HA, Brenner S, Neeman E, Lavi N. The chemical composition of aerosols settling in Israel following dust storms. *Atmospheric Environment*. 1991;254(12):2665-2670
- [6] Rivka A, Yehouda E, Onn C. Quaternary influx of proximal coarse-grained dust altered circum-Mediterranean soil productivity and impacted early human culture. *Geology*. 2021;49:61-65
- [7] Manheim FT. Red sea geochemistry Init. 1974. pp. 975-998
- [8] Hartmann M, Scholten JC, Stoffers P, Wehner F. Hydrographic structure of brine filled deeps in the Red Sea – New results from Shaban, Kerbit, Atlantis II and discovery deep. *Marine Geology*. 1998;144:311-330
- [9] Nurit T-G. Nano-Sized iron-Oxides and Clays of the Red-Sea Hydrothermal Deeps. Characterization and Formation Processes. Saarbrücken, Germany: VDM Verlag Dr. Müller Aktiengesellschaft & Co KG; 2009
- [10] Gideon S, Kapusta Y, Amir S, Peter K. Sedimentary K-Ar signatures in clay fractions from Mesozoic marine shelf environments in Israel. *Sedimentology*. 1995;42(6):921-934
- [11] Nurit TG, Vladimir E, Dimitry M. High-resolution transmission electron microscopy study of Fe-Mn oxides in the hydrothermal sediments of the Red Sea deeps system. *Clays and Clay Minerals*. 2009;57(4):465-475
- [12] Nurit T-G, Vladimir E, Dimitry M. Nano iron oxides in the Dead Sea area. *Journal of Earth Science*. 2016;2:94-104
- [13] Rochelle C, Udo S. The iron Oxides, Structure, Properties, Reactions, Occurrences and Uses. New York: VCH Weinheim; 1996. p. 573
- [14] Nurit T-G. Crystallization of Fe and Mn oxides-hydroxides in saline and hypersaline environments and in vitro. In: *Advanced Topics in Crystallization*. Rijeka: Intech; 2015. pp. 323-339

Chapter 3

Investigation on Building Materials with the SEM in the ESEM Mode to Demonstrate Their Capillarity Using the Contact Angle Method

Peter Körber

Abstract

The chapter describes the use of the Scanning Electron Microscope (SEM) in the Environmental Scanning Electron Microscope (ESEM) mode on building materials, whose capillarity is to be examined. The abbreviation SEM means Scanning Electron Microscope. The abbreviation ESEM means Environmental Scanning Electron Microscope. On the basis of condensation in the ESEM, the hydrophobicity of capillary building materials is demonstrated with the help of the contact angle method. In the chapter, the investigation in the ESEM is shown using capillary building materials that have been given subsequent injections. Due to the problem of rising masonry moisture on capillary masonry in the absence of a cross-section sealing, injection agents, which have a hydrophobic and pore-filling effect, subsequently are used in the borehole method. Such a subsequent masonry sealing must be checked for effectiveness. In addition to already existing macroscopic methods, a new microscopic detection method is presented. This detection method uses ESEM technology in the SEM to generate and detect in situ dew processes at samples taken from the injection level of the examined masonry. The output of the results is done by image or film. By means of the condensation with the medium of water, the contact angle measurement method on the dew drops can be used to make accurate statements about the water-repellent capabilities of the examined sample and thus about the sealing success. There are detectable correlations to the macroscopic detection methods. The contact angles measured in the ESEM during condensation are connected to the conventional macroscopic measurement methods. The method presented in this chapter offers the advantage to have very small samples and to be investigated in a short time with very precise results. The new detection method is suitable for practical use.

Keywords: SEM in the ESEM mode, capillary building materials, contact angle method, masonry moisture, capillary masonry, cross-section sealing, masonry injection, subsequent masonry sealing

1. Introduction

In the refurbishment of old buildings, especially in the area of monuments [1, 2], capillary building materials, for example, consisting of brick masonry are found very often. Since the building materials of old buildings are often capillary-active materials [3–5], there is distinctive water absorption and release as well as water transport behaviour on this material. This process is called capillarity. Investigating the capillarity of old building materials can be of considerable relevance. The water absorption and release behaviour is, for example, crucially important for moisture transport and the moisture penetration of components.

The possibilities that result from examining the capillarity of a material in the Environmental Scanning Electron Microscope (ESEM) are explained in this abstract, using a subsequent sealing with injection agents on capillary masonry.

In many cases when renovating old buildings [6], sealing has to be carried out later because no sealing was installed when the object was built or the sealing is no longer adequately functional now. The proof of capillarity and the description of the moisture behaviour of the building materials play a major role here.

A good example is the construction of a subsequent cross-section sealing with injection agents. Although already known from antiquity, the regular use of functioning building waterproofing at capillary building materials began around 1890. Nevertheless, there were no uniform rules for the execution of structural waterproofing at that time. Only in the 1930s, structural waterproofing was normatively regulated. Although the cross-section sealing in massive walls had already a higher priority than other seals on buildings at the end of the nineteenth century, cross-section seals were regularly installed in masonry walls since 1930 onwards. In the old building area, there are very often buildings to find that have a cellar, even if the space requirements made this cellar unnecessary. This is related to the previous construction use, in which the basement was due to lack of sealing technology while permanently moist, but served as a 'buffer' to the upper floors, which thereby could be kept sufficiently dry. In this way, the buildings were built without a cross-sectional sealing. For these reasons, solid brick walls in cellars are often encountered in old building renovation and monument preservation, in which there is rising masonry moisture due to non-existent cross-sectional sealing. However, due to usage or conversion requirements of a value retention, there is a great need to permanently seal capillary masonry walls against increasing moisture in the wall cross section in the refurbishment in the renovation of historical monuments. A main group in the retrofitting of masonry cross-section seals is the masonry injection methods, which do not require static interventions [7, 8].

There are currently about 150 different injection agents [7] available for the subsequent cross-sectional sealing of capillary masonry. All injection agents have in common that they are applied by the production of borehole chains in the masonry. The injection agents react chemically. The sealant layer in the masonry is physically formed. There are pressurized and non-pressurized processes to apply the injection medium into the masonry.

However, all injection agents work in the same way: they change the capillarity of the building material and thus also the water transport properties of the material [9]. Therefore, the capillarity of a capillary-active substance that is changed by the injection agent can be used as a reference for the investigations in the Scanning Electron Microscope (SEM) in the ESEM mode. The investigations with the SEM in the ESEM mode can provide information about the efficiency of such a subsequent sealing by

means of injection. In order to be able to monitor the injection procedure and to be able to demonstrate the effectiveness of the injection medium, it is therefore necessary to monitor the quality and quantity of the actually changed capillarity on the object [10].

The detection method presented here is based on the contact angle method in the Environmental Scanning Electron Microscope, ESEM. The ESEM is a modified version of a Scanning Electron Microscope, SEM [11, 12]. In contrast to the SEM, the ESEM can be used in low-vacuum mode. This circumstance allows the supply of a medium (here water steam) during the investigation. A cooling table in the chamber allows the sample to be refrigerated while the air in the chamber is at 100% relative humidity. Changing the chamber pressure causes condensation in the ESEM chamber [13]. During the investigation in the ESEM, condensation water droplets are formed on the sample. The contact angles can be determined on the formed drops of water [14]. When measuring the contact angle, one makes use of the interfacial tension of the water. Both static contact angles and dynamic contact angles can be measured in the ESEM. The contact angles provide information about the changed capillarity of the sample material on which the drops were formed. The contact angle can be measured directly in the ESEM or afterwards. The data obtained from this show a geometrically differentiated picture of the changed capillarity of the examined material. The method can provide information about the quality of the injection as well as about the geometric penetration with the injection agent.

2. The SEM in the ESEM mode

The Environmental Scanning Electron Microscope (ESEM) is a special variant of the Scanning Electron Microscope (SEM). The main difference to a conventional Scanning Electron Microscope lies in the lower vacuum in the measuring chamber [15]. Moreover, a special detector is installed for the operation of the ESEM. Due to the lower vacuum (low vac mode), a medium can be supplied to the chamber in ESEM mode. For the examination of building materials, the supplied medium is usually water/water vapour. The gas pressure in the chamber of the ESEM is usually 130–1.300 pascals. In the same way as when using the SEM, the sample is scanned by a focused electron beam in the ESEM. The signal resulting from an interaction with the sample is picked up by the detector and used to generate the image. The ESEM uses the generation of low-energy secondary electrons (0–50 eV), which are emitted from the sample surface as slow electrons. For signal amplification, the ESEM uses the gas in the sample chamber, which generates an amplification cascade through ionization. This system also neutralizes charges on the samples. The most important difference between the ESEM and operation in high vacuum (= SEM) is that in low vacuum the water is not 'expelled' from the sample and condensation processes (droplet formation) and can thus be made visible. For this purpose, the detector of the ESEM is not sensitive to light or temperature. In order to be able to visualize the water wetting and drying processes in the ESEM, different aggregate states of the medium, here water, which are pressure- and temperature-dependent, are used.

For this purpose, a cooling table connected to a recirculating cooler is arranged in the chamber of the ESEM. The sample is glued to this cooling table with carbon or conductive silver to ensure optimal temperature conductivity. As part of the investigations in the ESEM, the temperature conditions of the cooling table are fixed while the chamber pressure is changed. This causes a change in the state of aggregation of

the medium in the chamber (from gaseous to liquid). If the dew point is reached on the sample, the water condenses out on the sample surface. This process is recorded with the help of pictures. In the ESEM, the forming contact angle of a drop can be measured in situ using the contact angle measurement method. Progressive, receding or static contact angles can be measured on ripe droplets. If a drying process is to be shown, the condensation water that has formed can be evaporated by reducing the chamber pressure, and the drying process is made visible. Technically, the ESEM is very well suited to show dynamic condensation in situ [16–20] (Figure 1).

The figure above shows the limit curves of the three phases: gaseous (water vapour), liquid (water) and solid (water-ice). These phase areas meet at the triple point. At this point, the three phases are in thermodynamic equilibrium. The formation of condensation is related to the dependence of the state of aggregation of the phases on temperature and pressure.

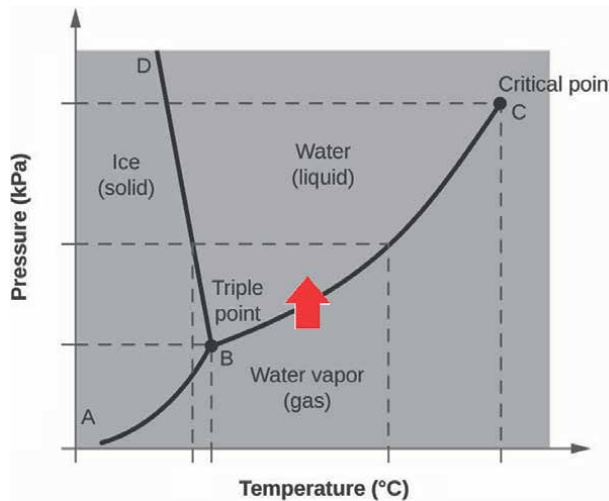


Figure 1.
Phase diagram of water, P. Körber.

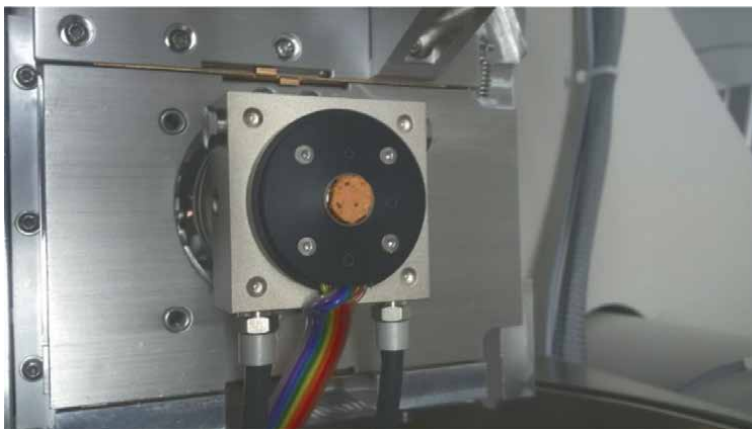


Figure 2.
Cooling table with circulation cooler, P. Körber.



Figure 3.
 ESEM chamber: Cooling table with circulation cooler, P. Körber.

Due to the change in the pressure conditions in the ESEM, the dew point inevitably occurs during the investigation in the ESEM, and the water that is gaseous in the medium becomes liquid in the form of droplets on the sample surface (**Figures 2 and 3**).

3. Contact angle method

The contact angle θ is the angle between the liquid surface and the outline of the contact surface at an interface between a liquid and a solid. The external stress of a liquid is defined by the imbalance of molecules within the liquid and at the liquid boundary (interface between liquid and gas). This intermolecular force that contacts the surface is called surface tension. A drop is formed due to the surface tension of a liquid. In addition, external influences such as gravity play a role shaping the drop. The contact angle of a drop occurs at the contact surface of the drop on a solid and also depends on the shape of the drop. The contact angle can provide information about the wettability of a solid with a liquid. The contact angle of a drop of water placed on a component surface can be

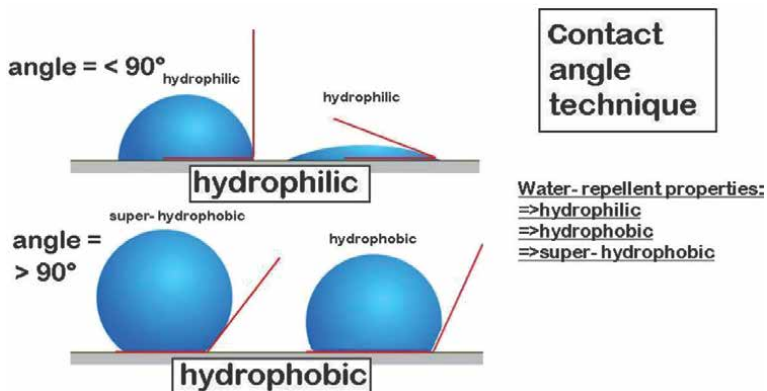


Figure 4.
 Contact angle measurement with the tangent method, P. Körber.

measured macroscopically or microscopically. Water is well suited for carrying out a contact angle measurement, as it is characterized by a relatively high surface tension (≈ 0.072 n/m). The principle of the contact angle measurement is illustrated in the **Figure 4**. The static contact angle is measured by applying a tangent to the point where the water droplet touches the solid surface and the ambient phase (here it is air). The contact angle decreases with increasing wettability of the solid (building material surface). The contact angle θ is defined as an angle at the phase boundary of the gaseous, liquid and solid phases of liquids on a solid surface surrounded by gas [21, 22]. This relationship was already defined in 1805 by Thomas Young.

Eq. (1): Interfacial tension between solid and gaseous:

$$\gamma_{SG} = \gamma_{SL} + \gamma_{LG} \cos\theta \quad (1)$$

In Young's equation, the solid-gas interfacial tension is calculated by adding the solid-liquid interfacial tension to the liquid-gas interfacial tension and multiplying it by the contact angle. The equation below is used to calculate the Young's contact angle.

Eq. (2): Young's equation for calculating the contact angle:

$$\cos\theta = \frac{\sigma_s - \sigma_{LS}}{\sigma_L} \quad (2)$$

Surface and interfacial tension defines the 'work' required to increase the interface area. Within the liquid, the molecules interact in all directions (cohesion), while at the interface there is no interaction of the liquid molecules with the outside (adhesion). Young's equation describes the balance of these forces. This is viewed at the three-phase contact line and exists when the contact line is balanced and at rest. Then the horizontal forces acting on the contact line exactly cancel each other out. The interfacial tension is temperature-dependent, so the contact angles also depend on the temperature and, for most substances, decrease with increasing temperature. However, because there are other forces acting on the contact line in addition to surface tension, the Young's contact angle cannot be measured per se. If there are movements of the contact line, one speaks of 'dynamic contact angles'. When the drop volume increases, one speaks of 'advancing contact angles', while when liquids evaporate, one speaks of 'receding contact angles'. In this context, it can be assumed that the advancing contact angle is always greater than the receding contact angle. The difference between these two contact angles is called 'contact angle hysteresis'.

The hydrophilic or hydrophobic properties of substances can be precisely determined using the 'Drop Shape Analysis System'. In this method, a droplet illuminated from behind is observed with a camera and displayed on a monitor. With this method a static contact angle is measured by assuming, for the sake of simplicity, that static conditions are present for the contact angle measurement. In fact, this is not the case, because contact angles determined in this way are also subject to certain, very small, changes during the measurement. However, this inaccuracy is included in the tolerance to be estimated and can therefore remain irrelevant for the purposes considered here.

The static contact angle can be measured using the tangent method, as shown above. The results of the contact angle measurements on building materials are differentiated using the 90° limit in A) hydrophobic $> 90^\circ$ and B) hydrophilic $< 90^\circ$. In addition to this 90° angle definition, the angle measurements also provide information about the gradual water absorption capacity of the substance being examined. If a dynamic condensation/evaporation process is present, static contact angles can only be measured when the dynamic equilibrium between condensation and evaporation

is reached. The contact angle method described here for determining the capillarity of a building material can also be applied macroscopically. In the present case, however, this method is applied microscopically in the ESEM. A reliable optical method for drop shape measurement can be carried out on the drops measured in the ESEM: The Drop Shape Analysis (DSA).

In the Drop Shape Analysis (DSA), images are taken of the droplets that are formed and then examined by using computer software. The contact angle is determined by the use of an image. The software can sharpen the captured image and recognize the contour of the drop. The measurement is computer-aided utilizing a geometric model. In the next step, the surface tension can be calculated applying the 'Young-Laplace-Fit' if the density difference and thus the imaging scale between the droplet phase and the surrounding phase are known. Accuracies of $\pm 0.2^\circ$ can be achieved here.

The optically measured drop contour can be calculated using a conic section equation => Conic Section Method. The conic section method is based on the assumption that the contour of the drop to be measured describes an arc of an ellipse.

4. Hydrophilic or hydrophobic

The term 'hydrophobe' (hydrophobic) is borrowed from ancient Greek (hýdor = water and phob = repellent). Hydrophobic describes a water-repellent property of a substance. This means that the substance does not dissolve in water and cannot be wetted by water. The term 'hydrophil' (hydrophilic) is also borrowed from the ancient Greek

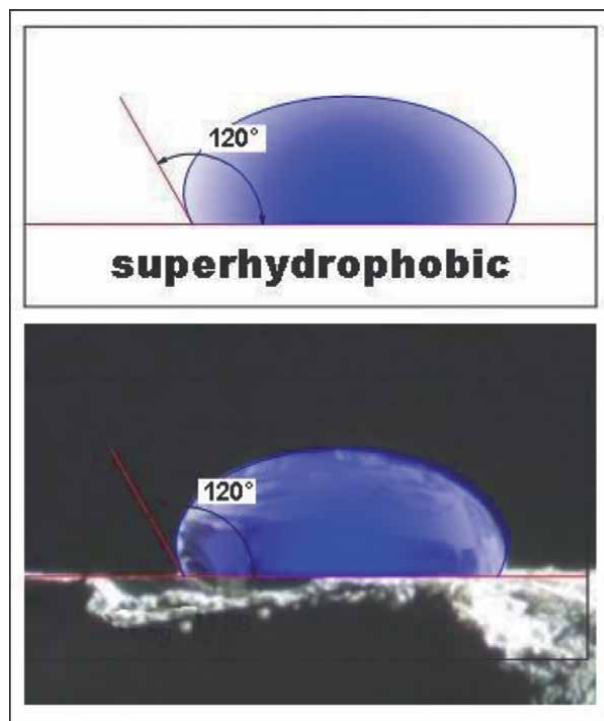


Figure 5.
Contact angle measurement: superhydrophobic, P. Körber.

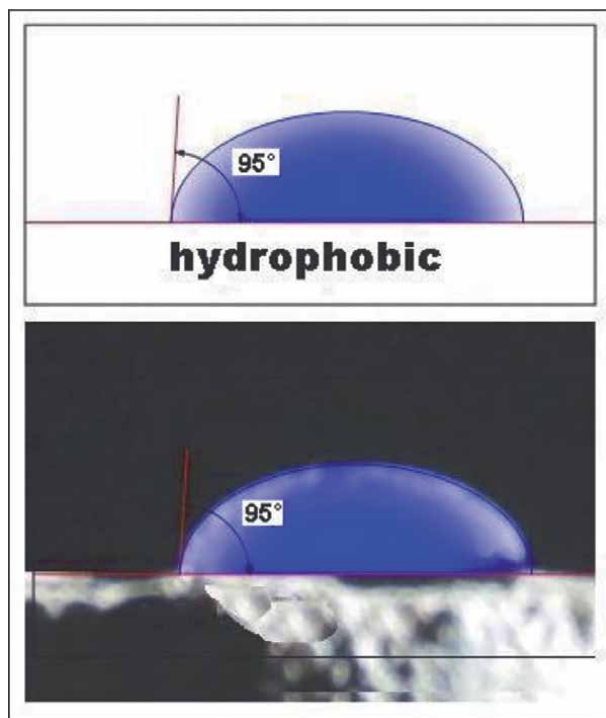


Figure 6.
Contact angle measurement: hydrophobic, P. Körber.

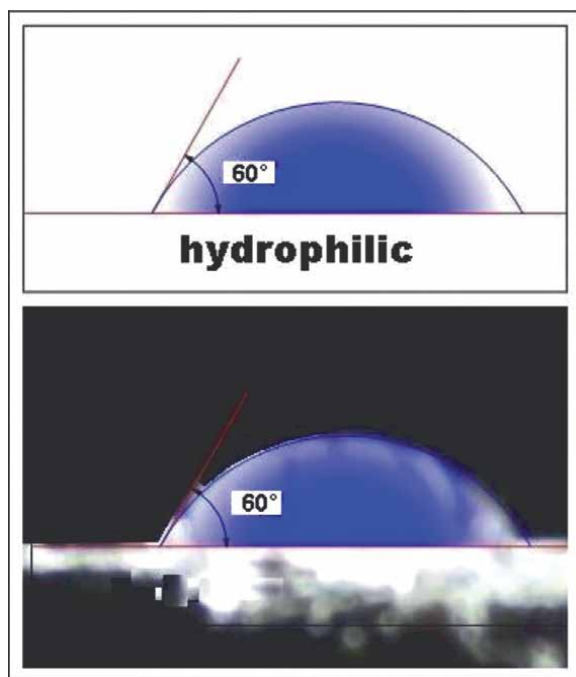


Figure 7.
Contact angle measurement: hydrophilic, P. Körber.

(hýdor = water and philos = loving). Hydrophilic means that a substance is water-friendly, water-loving. Hydrophilic describes a water-accepting property of a substance. This means that the substance can be dissolved in water and wetted with water (**Figures 5–7**).

5. Investigations in the ESEM on building materials

The examination method described here for building materials in the ESEM can be used in particular for the question in the hydrophobicity of the substance to be examined. During the investigation in the ESEM, condensation processes are carried out, which provide information on how water-absorbent the examined substance is [23].

The procedure for examining building materials in the ESEM is explained below on the basis of a subsequent waterproofing of capillary building materials using injection agents. Such an injection method is used in particular in historic buildings made of solid building materials and in renovations [9].

Investigations in the ESEM are particularly useful when the question arises to what extent a building material is capillary-active or to what extent the capillarity of the building material has changed. Such changes are conceivable, for example, through the use of injection agents in building waterproofing. In the case of injection agent seals, for example, on brick masonry, the penetration of the injection agent changes the capillarity of the building material in such a way that the transfer of water in the building material is impeded or prevented. In this way, it is possible to subsequently create a cross-section seal in masonry walls. For such a procedure, it is necessary to prove the changed capillarity of the building material. This proof documents the sealing success. In this respect, the condensation in the ESEM is predestined to provide evidence for the use of injection agents for the subsequent sealing. The advantage of the examination method in the ESEM is that very small sample quantities can be evaluated in a very short time. The ESEM investigations on building materials are therefore qualitative, microscopic (imaging) detection methods. In addition to these microscopic methods, there are also macroscopic detection methods to investigate the changed capillarity in building materials [24–29].

The qualitative microscopic (imaging) detection method in the ESEM as described here can also be used by verifying the macroscopic, also qualitative, detection methods. It can provide comprehensive information about the changes in the capillary building material under the influence of the injection agent used.

Furthermore, the extent to which an injection material was used at all and to which the building material now exhibits hydrophobic properties after use can be verified. With the exact measurements, the hydrophobicity of the building material can be gradually verified. A comparative examination of the building material before and after injection is possible. With the qualitative microscopic (imaging) detection method, as with the macroscopic investigations, local samples are taken from the injection level using mini core drillings and are analysed in the laboratory in the ESEM.

Essentially, significantly less material has to be removed from the structure for the verification method described here.

To examine the building material in the ESEM, samples are to be taken from the injection level. In addition, reference samples of the masonry without adding the injection agent are required.

The reference samples and the samples from the injection level are subjected to condensation in the ESEM. In the ESEM mode, condensation on a microscopic scale can be brought about within the pores of the building material (bricks and mortar).

The condensation process is recorded using pictures and, if necessary, using film. During the condensation process, there is a time window in which the contact angle of the forming water droplets can be measured. The measurement of the contact angle can be carried out directly in the ESEM.

In addition, the measurement can also be carried out retrospectively on the images generated in the ESEM. The measured contact angles can be used to determine whether the substance is hydrophobic or hydrophilic. The examination results consist of an imaging procedure that can be evaluated afterwards. In particular, comparisons with the reference samples are possible.

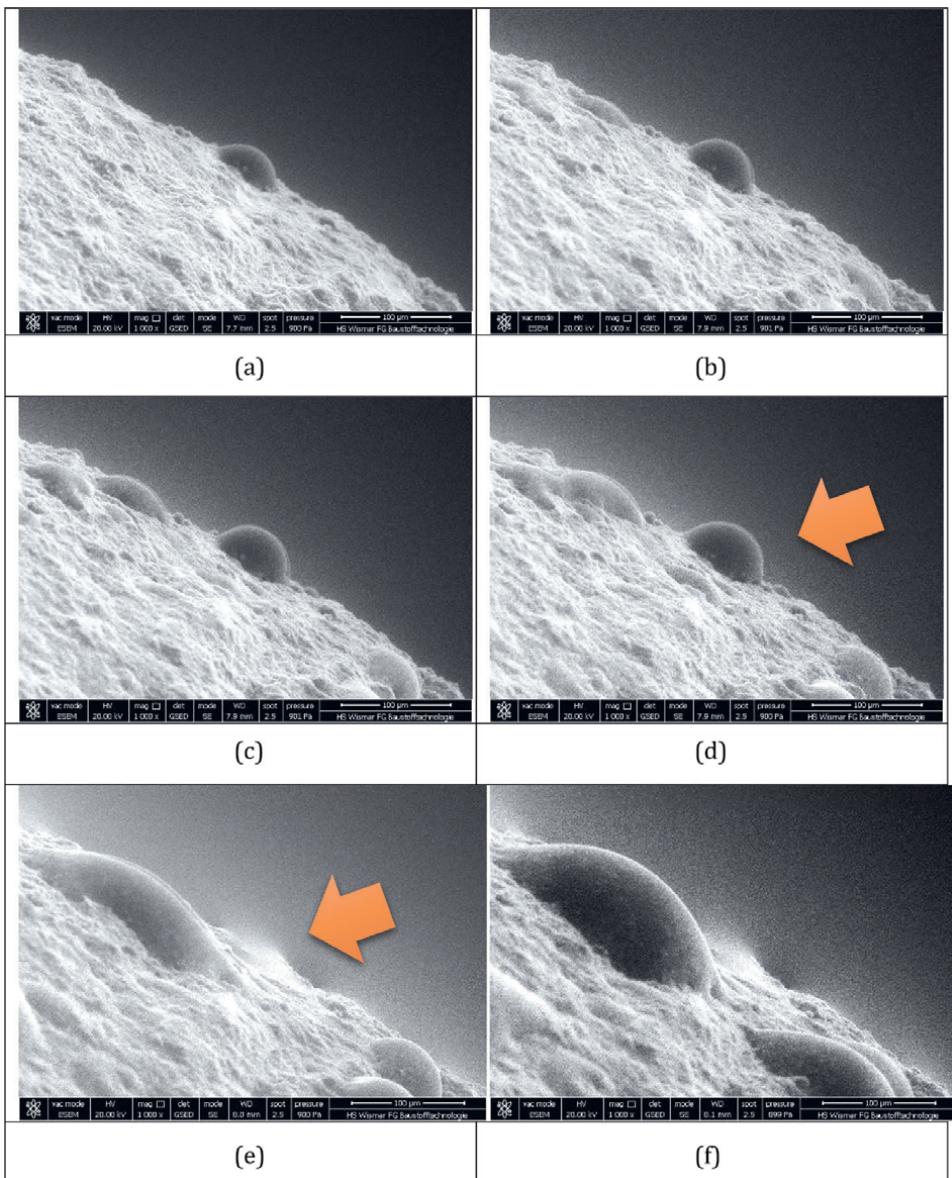


Figure 8. Condensation process on a brick sample in the ESEM, P. Körber.

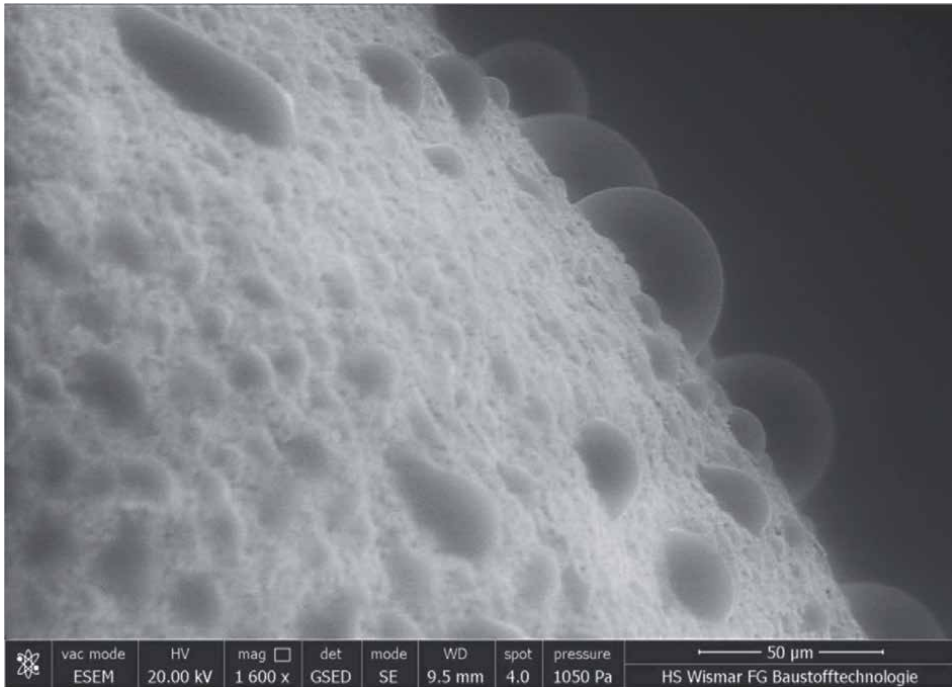


Figure 9.
Condensation process on a brick sample in the ESEM, P. Körber.

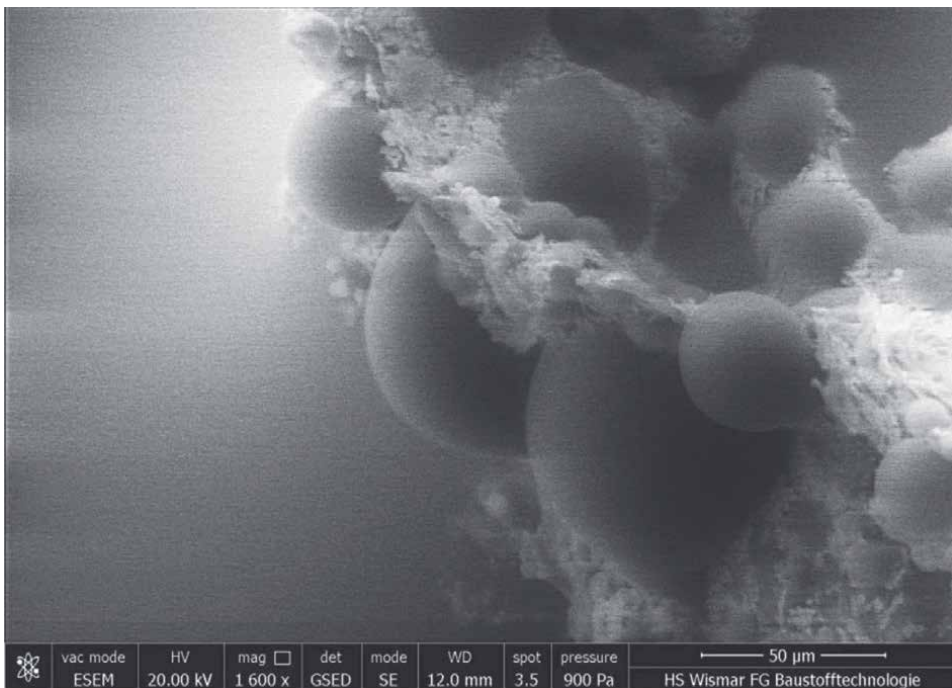


Figure 10.
Condensation process on a mortar sample in the ESEM, P. Körber.

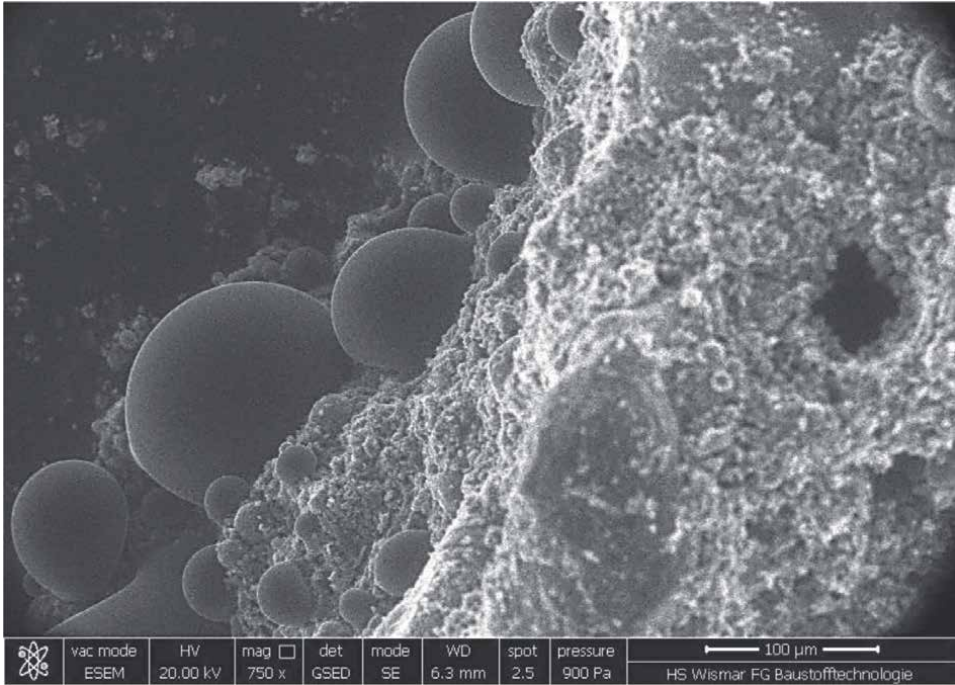


Figure 11.
Condensation process on a brick sample in the ESEM, P. Körber.

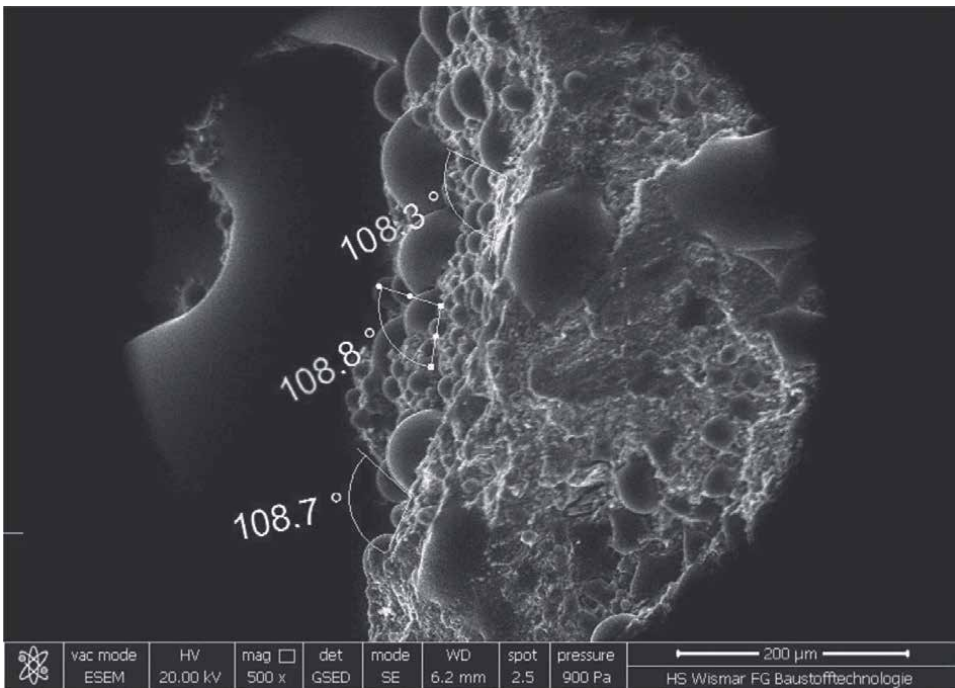


Figure 12.
Measurement of the contact angle in the ESEM, P. Körber.

The qualitative microscopic, imaging detection method described here can be flanked and verified by macroscopic examinations. The macroscopic investigations can serve as a calibration function for the ESEM measurements. In this way, serial tests can be carried out, in which differentiated proof of the sealing success of the subsequent building sealing with injection agents can be provided [29].

In **Figure 8a–f**, shown below, it becomes clear how the condensation water droplets form in the ESEM. After the time window for the formation of the drops has expired, these attract each other and then merge into one another, so that the time window for the measurement is over. The maximum achievable contact angle is relevant for the measurement.


The following figures show examples of the formation of condensation water droplets in the ESEM on brick and mortar samples (**Figures 9–11**). **Figure 12** shows the contact angle measurement, which takes place directly in the ESEM.

Author details

Peter Körber
University of Applied Science Technology, Business and Design, Wismar, Germany

*Address all correspondence to: kontakt@architekt-koerber.de

IntechOpen

© 2022 The Author(s). Licensee IntechOpen. This chapter is distributed under the terms of the Creative Commons Attribution License (<http://creativecommons.org/licenses/by/3.0>), which permits unrestricted use, distribution, and reproduction in any medium, provided the original work is properly cited. 

References

- [1] Bonk M, Cziesielski E. Lufsky, Bauwerksabdichtung (Sealing of Structures), Bd. 7. Auflage, Vieweg + Teubner Verlag; 2010. p. XVII 609
- [2] Klauß S, Kirchhof W. Baustoffe und Bauweisen (Building Materials and Construction Methods). Fraunhofer IRB Verlag; 2010. p. 192
- [3] Weber J. Horizontalsperren im Injektionsverfahren (Horizontal sealing in the injection procedure). In: Weber J, Hafkesbrink V, editors. Bauwerksabdichtung in der Altbausanierung (Building sealing in the old building renovation). Wiesbaden: Springer Vieweg; 2012. pp. 205-235
- [4] Hacquebord A, Lubelli B, Hees van R, Nijland T. Evaluation of spreading and effectiveness of injection products against rising damp in mortar/brick combinations. *Procedia Chemistry*. 2013;**8**:139-149
- [5] Tamas F, Tuns I. Removing capillary moisture from brick walls using a drying method and case study. *Bulletin of the Transilvania University of Brasov, Series I: Engineering Sciences*. 2010;**3**(52):323-328
- [6] Honsinger DJ. Nachträgliche Abdichtung gegen kapillar aufsteigende Feuchte in Mauerwerk (Subsequent sealing against capillary rising damp in masonry). *Der Bausachverständige*. 2013;**1**:23-32
- [7] Körber P, Rupieper D. Marktübersicht Injektionsmittel für die nachträgliche Horizontalabdichtung gegen kapillaren Feuchtetransport (Market overview Injection means for subsequent horizontal sealing against capillary moisture transport), B+B Bauen im Bestand, 5. Ausgabe. 2013:54-60
- [8] Körber P. Unterlassene Injektionsmittelabdichtung hat Folgeschäden, Hausschwamm durch fehlende nachträgliche Abdichtungen (Failed injection sealing has consequential damage, rotten wood by missing subsequent seals). In: *Der Bauschaden Spezial, Feuchteschutz in der Altbausanierung*. Merching: Forum Verlag; 2017
- [9] Nenadálova S, Balik L, Kolisko J, Klecka T. Impact of the chemical injection method on the dispersion of the injected agents in masonry, *Proceedings of the Conference on the Rehabilitation and Reconstruction of Buildings, CRRB 2012. Advanced Materials Research*. 2012;**688**:73-78
- [10] Körber P, Venzmer H. Rasterelektronenmikroskopische Nachweise von Injektionsmitteln in Mörtel- und Ziegelstrukturen unter Nutzung von Betaungsvorgängen (Scanning electron micrographs of injectables in mortar and brick structures using dewing processes). In: Schmidt B, Schmidt D, Venzmer H, editors. *Energielieferant Altbau*. Berlin: Beuth Verlag; 2017
- [11] Colliex C. Elektronenmikroskopie, Eine anwendungsbezogene Einführung (Electron microscopy, an application-related introduction). Stuttgart: Wissenschaftliche Verlagsgesellschaft mbH; 2008
- [12] Reimer L, Pfeifferkorn G. Raster—Elektronenmikroskopie (Scanning electron microscopy). Berlin Heidelberg: Springer Verlag; 1977
- [13] Danilatos GD. Environmental Scanning Electron Microscopy. In: *In-Situ Microscopy in Materials Research*, ESEM Research Lyboratory, Sydney, Australia. New York: Springer Science+Business Media; 1997. pp. 13-44

- [14] Hecht C, Steiner T. Kontaktwinkelmessung des Bausachverständigen, (Contact angle measurement of the construction expert) Der Bausachverständige. 2009;2:29-31
- [15] Gai PL, Boyes ED. Environmental high resolution electron microscopy in materials science. In: Gai PL, editor. In-Situ Microscopy in Materials Research. Boston: Springer; 1997. pp. 123-147
- [16] Stokes DJ, Thiel BL, Donald AM. Dynamic secondary electron contrast effects in liquid systems studied by ESEM. Polymers and Colloids: Department of Physics, University of Cambridge, UK; 2000
- [17] Doehne E, Stuli C. Applications of the environmental scanning electron microscope to conservation science. MRS Online Proceeding Library Archive, Symposium G—Materials Issues in Art and Archaeology II. 1990;185:23-29
- [18] Doehne E. ESEM development and application in cultural heritage conservation. In: Gai PI, editor. In-Situ Microscopy in Materials Research. Vol. 3. 1997. pp. 45-62
- [19] Gai PL. In: Gai P, editor. In-Situ Microscopy in Materials Research, Bd. 1. New York: Springer Science+Business Media; 1997. p. 336
- [20] Dufek M. FEI Company, The Quanta FEG 450. SEM/ESEM User Operation Manual. 2013:7-88
- [21] Yuan A, Lee TR. Contact angle and wetting properties. In: Bracco G, Holst B, editors. Surface Science Techniques. Berlin Heidelberg: Springer Verlag; 2013. pp. 3-34
- [22] Bracco G, Holst B, editors. Surface Science Techniques. Berlin: Springer Verlag; 2013. p. 663
- [23] Pop M, Campian C. Methods for elimination of dampness in Building walls. IOP Conference Series: Material Science and Engineering. 2016;133:1-6
- [24] Hardt TA. Environmental SEM and Related Applications. In: Rickerby DG, Valdrè G, Valdrè U, editors. Impact of Electron and Scanning Probe Microscopy on Materials Research, NATO Science Series (Series E: Applied Sciences). Vol. 364. Netherlands: Springer; 1999. pp. 397-406
- [25] Stelmashenko NA, Craven JP, Donald AM, Terentjev EM, Thiel BL. Topographic contrast of partially wetting water droplets in environmental scanning electron microscopy. Journal of Microscopy. 2001;204(2):172-183
- [26] Rykaczewski K, Scott JHJ, Fedorocv G. Electron beam heating effects during environmental scanning electron microscopy imaging of water condensation on superhydrophobic surfaces. Applied Physics Letters. 2011;98:106-109
- [27] Milijkovic N, Enright R, Wang E. Modeling and optimization of superhydrophobic condensaton. Journal of Heat Transfer. 2013;135(11), paper No. HT-12-1145
- [28] Guikema JW. Scanning Hall Probe Microscopy of Magnetic Vortices in Very Underdoped Yttrium-barium-copper-oxide. Stanford Linear Accelerator Center: Stanford University, Stanford; 2004
- [29] Körber P. Two-Stage Study Program to Demonstrate the Effectiveness of Injections in Capillary Masonry Structures by Using the ESEM. In: Chapter 7, Advances in Engeneering Research. Vol. 29. New York: Nova Science Publishers, Inc.; 2019. pp. 191-227

Section 2

Electron Microscopy for
Biomedical Applications

Chapter 4

Atomic Force Microscope in Forensic Examination

Niha Ansari

Abstract

Criminal activities have their footprints from time immemorial and nature of crime has drastically changed over a period of time. There is neither a geographical boundary, nor technical limitations. Moreover terrorist's activities, drug trafficking eco-crimes, high-profile crimes, robbery hit and run cases, building collapse, petroleum products adulteration are some of latest forms of crimes. In last 20 years, scanning probe microscopes have emerged as an essential technique in various fields, and atomic force microscope (AFM) is most commonly used scanning probe technique which has shown its wide range of application in examination of various evidences encountered on crime scene. Major advantages of AFM involve its high resolution in three dimensions, and sample is not necessary to be conductive and it does not need to be operated within a vacuum. It helps in studying a large range of topographies and many types of materials can be imaged under it. Evidences such as blood, fibers, hair, soil, finger prints, gunshot residue, pollen, etc. found on crime scene at nano- or micro-level can be examined under AFM. The chapter describes applications of AFM with respect to its application in examination of evidences that can help in bringing justice.

Keywords: Atomic force microscope, forensic science, trace evidence, physical evidence, forensic examination

1. Introduction

Forensic science is an umbrella term incorporating an innumerable professions where they uses their skills to help law enforcement agencies in reaching to the truth during any investigations. Forensic scientist succors in investigating and adjudicating both criminal and civil cases. Criminal activities have their footprints from ancient time and the nature of crime has considerably changed over a time period. Criminal activities are neither limited to geographical boundary, nor technical limitations. Moreover terrorist's activities, drug trafficking eco-crimes, high profile crimes, robbery hit and run cases, building collapse, petroleum products adulteration are some of the latest forms of crimes. In many cases, forensic evidence plays key role in obtaining conviction and often only trace evidences are existent on a suspect.

In past 20 years, scanning probe microscopes have emerged as an essential technique in various fields. The atomic force microscope (AFM) uses the most common scanning probe technique for materials characterization [1, 2]. Major advantages of

AFM involves its high resolution in three dimensions, the sample is not necessary to be conductive and it does not need to be operated within a vacuum. It help in studying a large range of topographies and many types of materials can be imaged under it. AFM is capable of imaging 3D topography information from the angstrom level to the micron scale with extraordinary resolution. In AFM, the Z-axis resolution (perpendicular to the surface) is better than the X–Y scan plane resolution of the sample surface. The Z-resolution in AFM is on the sub-angstrom level under ambient atmospheric condition while the resolution in X–Y scan is limited due to the diameter of the probe and is on the order of a few nanometers. In the X and Y axis, AFM images shows complication of the probe geometry and sample texture, however, if the probe is much smaller than the surface features, the image distortions lead by the probe are nominal. The AFM sensitivity is derived from a force sensor which measures the forces between the probe and target surface which is usually less than 1 nN/nm. **Figure 1** shows a representation of the AFM [3].

Evidences such as blood, fibers, hair, soil, finger prints, gunshot residue, pollen etc. are found on the crime scene at nano or even at molecular level. At present, different nanotechnologies such as the application of nanoscale powders, high resolution scanning and transmission electron microscopy and atomic force microscopy are applied for the examination of various evidences for forensic investigations [4, 5]. Nevertheless, forensic trace depiction of forensic evidences at the nanoscale does not yield applicable forensic information as explained by Inman and Rudin [6, 7] with the principle of divisible matter. Examination of such type of evidences require combination of sophisticated instrumentation which can help in proving the facts and can provide a conclusive results which can provide justice to the society. As mentioned earlier AFM technique has showed application for the examination of such type of evidences which is centered with an extremely high resolution scanning probe microscope to sense intermolecular and interatomic forces between a sharp probe and the specimen. AFM is highly applied in forensic field as it has the biggest advantage of examination of evidences in minimal non-destructive manner as well as possess imaging capabilities to examine the sample in various environmental conditions. As it possess highly accurate piezoelectric scanners its lateral resolution is hundreds of times better than the diffraction limit of traditional optical microscope. The sample is scanned by the tip of the cantilever which results into the deflection because of the attractive or repulsive forces between sample and tip molecules. The cantilever's deflection is measured by

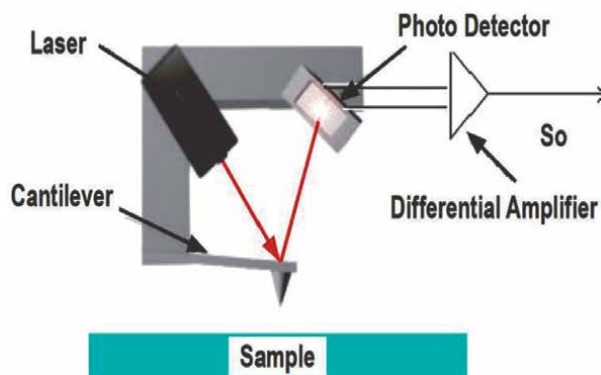


Figure 1.
A representation of the AFM.

the laser beam which is later converted into an electrical signal by photodiodes, thus helping in imaging of the topography surfaces of the sample at the nano-level.

2. Sample preparation

Sample preparation art is in fact a simple procedure of critical-path steps, where every single step makes a large difference. The sample preparation in AFM is easier as compared to the other electron microscope techniques [8]. Further, AFM provides advantage of operating in almost any environment conditions, such as aqueous solutions, in air, vacuum, or other gases. Typically, AFM is operated at three different modes namely contact mode, noncontact mode, and tapping mode. Contact is a static mode, and tapping and noncontact are dynamic modes, as the cantilever oscillates in tapping and noncontact modes. This is achieved by adding an extra piezoelectric element that oscillates up and down between 5 and 400 kHz to the cantilever holder. The contact mode is the mode where the tip of the cantilever scans the sample in close contact with the surface. This mode is used usually for surface force measurements. In noncontact mode, the tip flies about 5–15 nm above the sample surface. Whereas in tapping mode the tip of probe touches the sample, and moves completely away from the sample in each oscillation cycle. The tip usually taps the sample during each oscillation in tapping mode, hence it is often the most stable mode used in air. In noncontact mode the cantilever stays close to the sample all the times and possess much smaller oscillation amplitude. The contact mode imaging is heavily influenced by frictional and adhesive forces which may damage samples and distort image data. The non-contact imaging mostly provides low resolution and can get hindered by the contaminant thus producing interfere with oscillation. On the other side the tapping mode imaging overcome the disadvantages of the other two modes. It eradicates the frictional forces by spasmodically contacting the surface and oscillating with appropriate amplitude to avoid the tip from being trapped by adhesive meniscus forces from the contaminant layer.

In general, for particle analysis in AFM the smaller the size of the particles the flatter/smoother the substrate should be that is the size of the particles should be greater than the topographical features of the substrate. Commonly used substrates are glass cover slips, highly ordered pyrolytic graphite, silicon oxide wafers, mica and atomically flat gold. For biological samples like imaging DNA¹² and proteins, atomically flat substrates are used while for fine-size features examination like bio-cells, colloids, quantum dots and carbon nanotubes, glass, mica and silicon substrate are used. If a sample comes in the form of a bulk material such as wood or epoxy-resin, metal discs are used as a substrate. The adhesive used in this case is typically carbon tape or thermal wax [3].

In case of biological samples, in order to observe biological structures in their native state, they are supposed to be attached to a smooth solid substrate to resist the lateral forces exerted by the scanning tip, in that reverence, mica, glass and silicon oxide have proved to be excellent substrates for the examination. Muscovite mica, is a non-conducting layered mineral composed of multiple 1 nm thick layers [9]. It can be cleaved simply with the help of adhesive tape to yield clean, atomically flat surfaces which are negatively charged. Mica is most normally used substrate for imaging double-stranded DNA, DNA-protein complexes, protein arrays, densely packed proteins, supported lipid films and animal cells. Also, the mica surface can be modified with silanes which helps in both to promote adsorption or to allow covalent binding of the

biomolecules [10]. Glass represents another suitable substrate for imaging biological samples. For imaging cells and other large structures glass cover slips are flat enough for imaging adsorbed molecules while in some cases, silicon oxide wafer can also be used instead of glass. Though they are more expensive and difficult to handle, they offer much smoother surface than glass. Hydrophobic substrates, highly orientated pyrolytic graphite, which is atomically flat over large areas [11] are also preferred for biological sample preparation. Hydrophobic surface can be obtained by coating the mica surface with carbon for immobilizing DNA [12, 13].

For imaging document, adhesives and fibers sample under AFM, the frequently used substrate is microscope slide. Usually the samples are cut as per the required area to be imaged under the AFM and then double-sided adhesives are applied to affix the sample at its fixed position as when the AFM tip is scanning it does not get deviated from the position. For soil sample analysis usually the grains are pressed into pressure-sensitive adhesive putty to provide suitable support during the scanning process thus this allows for retrieval of the grains afterwards or realignment if necessary during analysis [14–16].

The hair samples are priorly washed before being examined under microscope using solvent namely sodium dodecyl sulfate solution or double distilled water. The substrate like metal discs or glass slide can be used as they are stable and shown negligible drift or creep. Adhesives such as conductive sticky carbon pads or double-sided tape are used to fix the sample at its position. If conductive sticky carbon pads are used as an adhesive then the hair sample are lowered onto the pads and pressed into place using tweezers, so that the fibers did not roll on the pad and hence pick up any contamination from the adhesive [14, 17, 18]. Researchers have also used epoxy as an adhesive at the sample ends to ensure that no interference with the top surface occurs and the adhesion between the hair sample and AFM disc keeps the middle of the sample fixed to the disc during AFM measurements [19].

3. Application of AFM in forensic science

This section recapitulates a number of AFM studies that illustrates applicability of AFM in relation forensic traces evidence analysis and its potential for crime investigations or reconstruction.

3.1 Determination of the age bloodstains

Blood stains are the most common type of forensic evidence found on the crime scene. The blood stains play very important role in the time determination of the actual criminal activity, hence determination of the age of bloodstains can prove to be highly effective in solving the crimes in shorter time duration. This information can provide a good perception regarding the victim time of death or to create a link between the suspects to the crime scene at the time when crime was committed. This area has attracted much attention worldwide over the years of various researchers since very few techniques such as electron paramagnetic resonance, high-performance liquid chromatography, quantification of RNA degradation and hyperspectral imaging [20–22]. In the review published by Bremmer et al. [23] they mention about the invasive techniques such as HPLC method, RNA analysis and EPR. Hyperspectral imaging are applied for the same problem. Even though HSI is a promising technology it has high error rate of about 2.7 days as per Edelman et al. [22].

Research has been done where the application of AFM is explored to study morphological changes of red blood cells (RBCs) to determine the relation with the time of death of individual. Wu et al. [24] has studied, the time-dependent, morphological changes of RBC in three different conditions such as room-temperature condition (controlled), outdoor environmental condition (uncontrolled) and low-temperature condition (controlled) using AFM on clean glass or newly peeled mica. They found that the substrate types have different effects on cellular morphology of RBC. Further, the RBC showed typical biconcave shape on mica and biconcave shape or flattened shape on glass, also the mean volume of RBCs on mica was significantly larger than that of cells on glass. In relation to the time, the changes in cell volume and adhesive force of RBC under the controlled room-temperature condition were similar to those under the uncontrolled outdoor-environmental condition as the time lapse. However, under the controlled low-temperature condition, the changes in cell volume happened mainly due to the RBCs collapse and the adhesive force curves exhibited the high alternations in RBC viscoelasticity. They concluded that AFM has significant application in forensic medicine or investigations, in relation to the estimation of age of bloodstain. **Figure 2** shows the morphological comparison of RBCs on mica (a) and glass.

Chen and Cai did study on the morphological changes in a whole erythrocyte and of the erythrocyte membrane surface ultrastructure using tapping mode atomic force microscopy (TM-AFM) on mica substrate exposed in air over a 5-day period. They observed that the erythrocyte showed deformation of whole cell and membrane surface of unfixed erythrocytes as the time lapse. After 0.5 days of exposure, the fissures and cell shrinkage was observed and at 2.5 days of exposure, the development

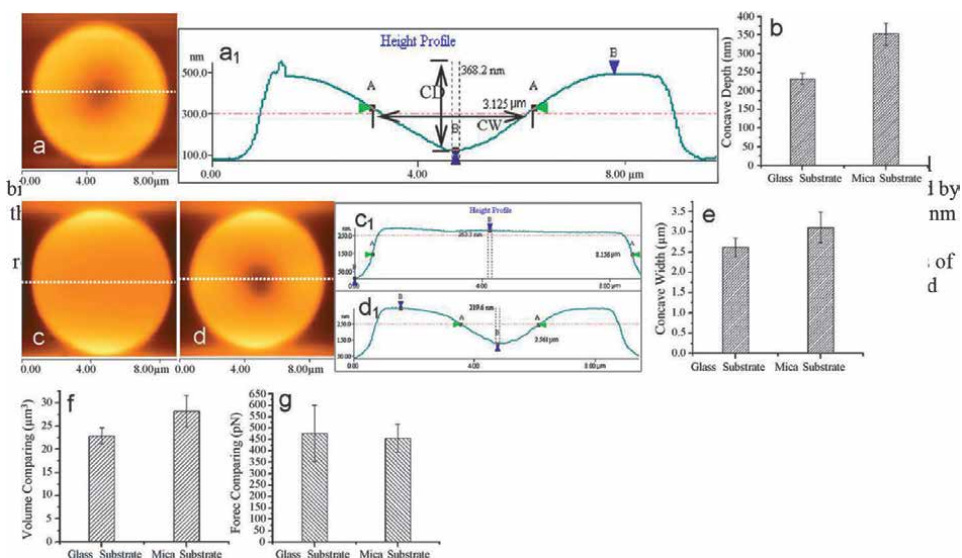


Figure 2. Morphological comparison of RBCs on mica (a) and glass (c) and (d). (a) and (d) RBCs in typical biconcave shape. (c) A flattened RBC. (a1) presents a height profile extracted from the cross section indicated by the dashed line in (a). The AFM-measured concave depth (CD) and width (CW) (FWHM) of RBC are 368.2 nm and 3.125 μm, respectively. (c1) and (d1) present the height profiles from the dashed lines in (c) and (d), respectively. The CD and CW in (d) are 219.6 nm and 2.561 μm, respectively. (b) and (e) present histograms of CD (b) and CW (e) of RBCs on various substrates. (f) and (g) indicate the differences of cell volume (f) and adhesive force (g) between RBCs on mica and on glass.

of nanometer-scale protuberances was observed, also the protuberances number increases with increasing time. Hence the present study presented the application that the changes of cell shape and cell membrane surface ultrastructure can prove to be helpful to estimate the time of death [25].

Lamzin and Khayrullin in their work studied the changes of RBC membranes stiffness in sRBC and the form and size of RBC probed using AFM by storing samples for 35 days at standard temperature conditions as shown in **Figure 3**. Their research revealed that statistically significant increase of YM values of RBC were observed as well as alteration of their form to echinocytes and spherocytes of sRBC within 35 days at +4°C was noticed. They mentioned that this work can prove to be useful as an immediate criteria for applicability of sRBC for blood transfusion [26]. Marco Girasole et al. has exploited the full potential of atomic force microscopy (AFM) to investigate various characteristic of the erythrocytes' life, death and interaction with the environment. As per Marco Girasole et al. [27] AFM is still a continuously growing technique which can be applied for studying more variant information in relation to the RBCs biochemical or biophysical status at different environmental conditions.

Threes Smijs et al. applied atomic force microscopy to investigate the elasticity of RBCs from the peripheral zone of 4–8 day old bloodstains. They observed that the elasticity of six RBCs from a 5 day old bloodstain seemed homogenous with a mean Young's modulus of 1.6 ± 0.4 GPa. As the time lapse, a significant age effect was observed in RBC elasticity that is on 4 days: 0.8 ± 0.1 GPa; 5 days: 1.7 ± 0.9 GPa; 6 days: 2.3 ± 0.6 GPa; 7 days: 4.5 ± 0.6 GPa; 8 days: 6.0 ± 1.8 GPa; probe spring constants 25.16–67.48 N/m. They found that a bloodstain age determination with a 24 h precision only for 6–7 day old stains can be done. The silicon tip condition was regularly checked using scanning electron microscopy as an increase in bluntness was noticed after four to six cell indentations [28].

Cavalcanti and Silva studied biophysical properties that is morphology and elasticity of RBCs using atomic force microscopy. They aimed to investigate the time since death (TSD) from blood smears by analyzing changes occurring in the RBCs of a group of voluntary. Further, they also investigated that whether any difference in TSD analysis occurs on three different surfaces such as glass, metal, or ceramic after

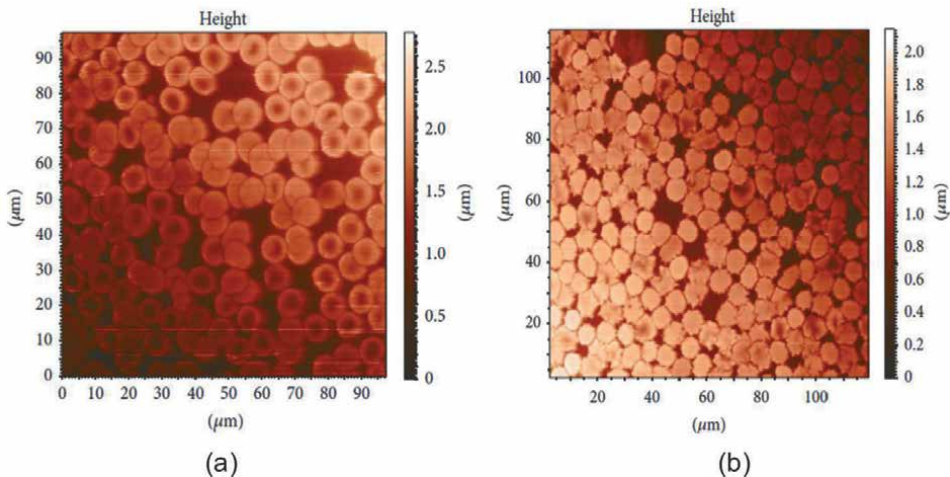


Figure 3. The AFM image of the dry specimen prepared from sRBC after 1 day (a) and 35 days (b) of storage.

blood smears deposition occurs on these surfaces. They calculated force \times distance curves obtained from RBCs membrane surface deformation as a function of time. They observed that there is no appreciable difference in the structure of RBCs over 28 days but significant differences were noticed on glass, metal, or ceramic surfaces. They concluded that the use of AFM in crime scenes still requires the development for accurate estimation of the TSD for blood spots [29]. Strasser et al. also explored erythrocytes in a blood sample to study elasticity changes in a fresh blood spot on a glass slide. At first they found presence of several RBCs in “doughnut-like” structure, which could easily be detected due to their typical “doughnut-like” appearance further the elasticity pattern showed a decrease over time which may be due to alteration of the blood spot during the drying and coagulation process. They concluded that these preliminary data can demonstrate the capacity for development of calibration curves, which have potential in estimation of bloodstain ages during forensic investigations [30]. Different body fluids are also been utilized for the extraction of DNA because of its use as a forensic tool during investigation. AFM can add in the characterization of the “trace DNA” deposited on various surface during any mutual contact. The stiffness of DNA's double strand can be discriminated from its single strand and counting of the copied DNA can be done by using AFM [31].

3.2 Document forgery

Document examination involves techniques which causes less or no damage to the documents and allows maximum retrieval of data from it. The determination of the sequence of strokes is still a big problem in the field of forensic document examination. Till today the optical microscope are used with different illumination methods and magnifications in determination of sequence of strokes. But the use of same does not provide a reliable results in every cases because of the interaction of the light with crossing ink lines, the depth of focus, low resolving power as well as low magnification range of the optical microscopes. Kasas et al. [32] studied line crossing problem on paper printed form dot matrix printers and different ball-point pens on plain paper. They found that AFM produces qualitatively similar results and overcomes some of the scanning electron microscope limitations, i.e., vacuum and specimen's conductive coating. **Figure 4** shows the cut-outs of crossings of ball-point pen strokes on dot matrix printed letters in newer printer ribbon and worn printer ribbon. They concluded that AFM is a powerful alternative to the SEM for line crossing problem. Brandao et al. in their work has focused on the problem of counterfeiting which involves making an imitation or copy manufactured without the legal sanction of the government. They explored AFM and Raman techniques for the examination of both authentic and counterfeit Brazilian driver licenses, and national and international banknotes. The AFM results showed that the parameters, such as roughness and topographic profiles of the chalcographic region of banknotes and Brazilian driver licenses, can be successfully visually discriminate between authentic and counterfeit documents. They also showed the application of statistical analysis using the Student's t-test which showed that the asymmetry values obtained from series numbers and micro-letter regions can help in identifying the counterfeiting. They also indicated that the paper used to counterfeit the Brazilian driver license and the real banknote was an “office” type with inkjet printing by the use of the AFM technique [33]. Further the combination can also help to recognize the crossing lines between ball-point pens, and ballpoint pens and printers, to discriminate between genuine and counterfeit medicines, to identify counterfeit documents produced from washing

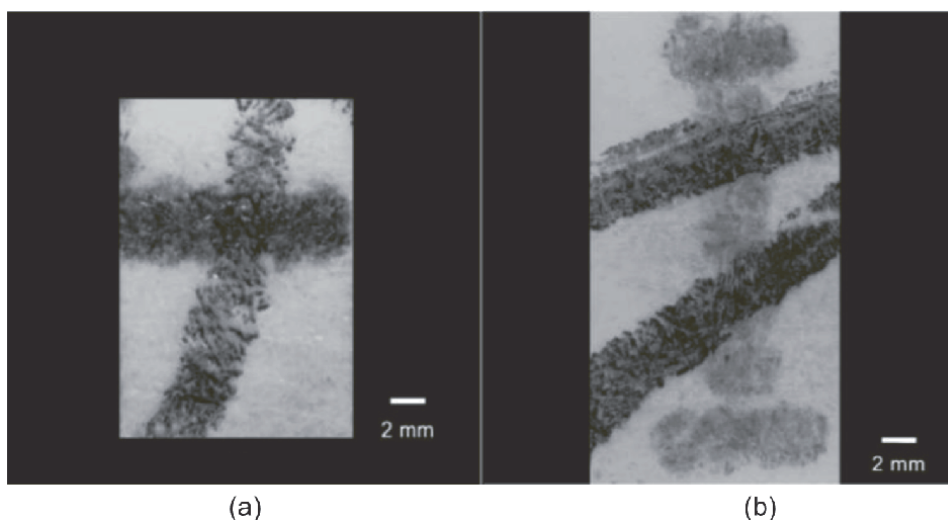


Figure 4. Cut-outs of crossings of ball-point pen strokes on dot matrix printed letters. (a) Newer printer ribbon; (b) worn printer ribbon.

methods, to determine the microstructural information on textile fibers (discriminate between carpets, clothes, cars, etc.) in a crime scene investigation. The combination provides fast, very reliable, and reproducible analysis.

Chen et al. in their work highlighted the quality of AFM compared to SEM for forensic forgery investigations in relation to crossing lines. They examined topographic features of four papers namely duplicator, copper printing, glassine and kraft paper on which crossing lines were done with three different types of oil-based pens as shown in **Figure 5**. For all pens they establish similar differences in height profiles analogous to the inks accumulations at the places where the first pen stroke overlay with the edge of second pen stroke. The work do showed the usefulness of AFM imaging to detect crossing lines under the selected test conditions [15]. As per Ellen, AFM imaging technique can provide high potential in forensic document examination especially in cases to study crossing lines and document forgery cases which can further be explored [34]. Although the many research is been done to prove the usefulness of AFM imaging to detect crossing lines but the overall paper surface roughness hampers the detection of erased, partially erased lines or slightly printed ink patterns on the pages. The height profiles of ink streaks on documents differs on the different types of the paper as the absorption differs. These hinder the correct interpretation of the height images. Though if AFM imaging is applied in these types of investigations the confirmation can only be achieved by usage of other instruments such as Raman spectroscopy to convey the final crucial decisive information.

3.3 Hair analysis

Hair can prove to be a useful evidence in crimes in relation to determine the history of drug intake and abuse as well as exposure to toxins as the chemical composition of hair does not change by the external environment. Hair is the most encountered evidence in a forensic investigation and can act as a good source of DNA. The mitochondrial DNA present in the hair shaft and nuclear DNA is mostly within

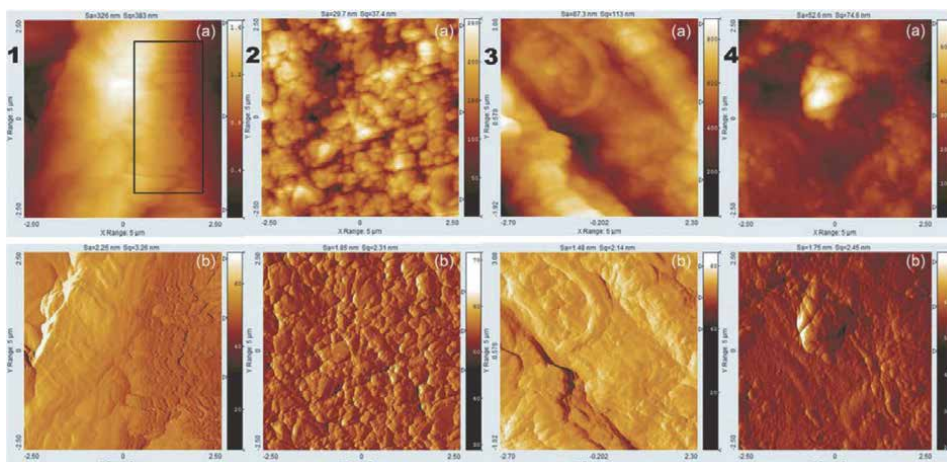


Figure 5. Duplicator paper (1), copper printing paper (2), glassine paper (3) and kraft paper (4); (a) topographic image, (b) amplitude image.

the root sheath play important role in DNA examination [35]. AFM offers unique advantages for analysis of hair surface, primarily due to the high image resolution as well as an ease of sample preparation. Durkan and Wang employed atomic force microscopy in a forensic approach to distinguish between different hair care products on the basis of the deposits left behind. They studied AFM techniques on hair samples that which were washed/treated with a number of different shampoos/conditioners and 2-in-1 products as shown in **Figure 6**. They found that the exocuticle carries a negative charge and gets deposits on unwashed hair with a mean roughness of up to 50 nm. Further they found that washing hair with shampoos reduces the roughness of hair + deposits to typically below 10 nm also the 2-in-1 products, conditioners or shampoos shows deposits that cover the entire surface, with roughness up to 30 nm. They concluded that the measurement of surface roughness combined with images of the resulting surface deposits can prove effective to distinguish between the effects of different hair care products [17].

The surface topography of human hair is defined by the cuticles which helps in cosmetic properties determination of the hair. The cuticles condition has the potential to aid in the medical diagnosis and forensic sciences. AFM offer unique advantages in hair surface analysis as it provides high resolution image and the simplicity of sample preparation. Gurden used an algorithm for the automatic examination of AFM images of human hair. By using a series of descriptors such as tilt angle, step height and cuticle density, the cuticular structure of hair was characterized and quantitatively investigated. They studied 38 AFM images consisting of hair samples untreated and bleached hair samples along with examination of the root and distal ends of the hair fiber. The multivariate classification technique partial least squares discriminant analysis was used to test the capability of the algorithm for further characterization of the images according to the hair properties. They were able to classify 86% hair images correctly. They study the classification of hair properties based on several cuticular descriptors by calculating it form the height images of various hair parts. The cuticular descriptors provided information on hair surface properties which can be correlate between the hair structure characteristics and environmental conditions

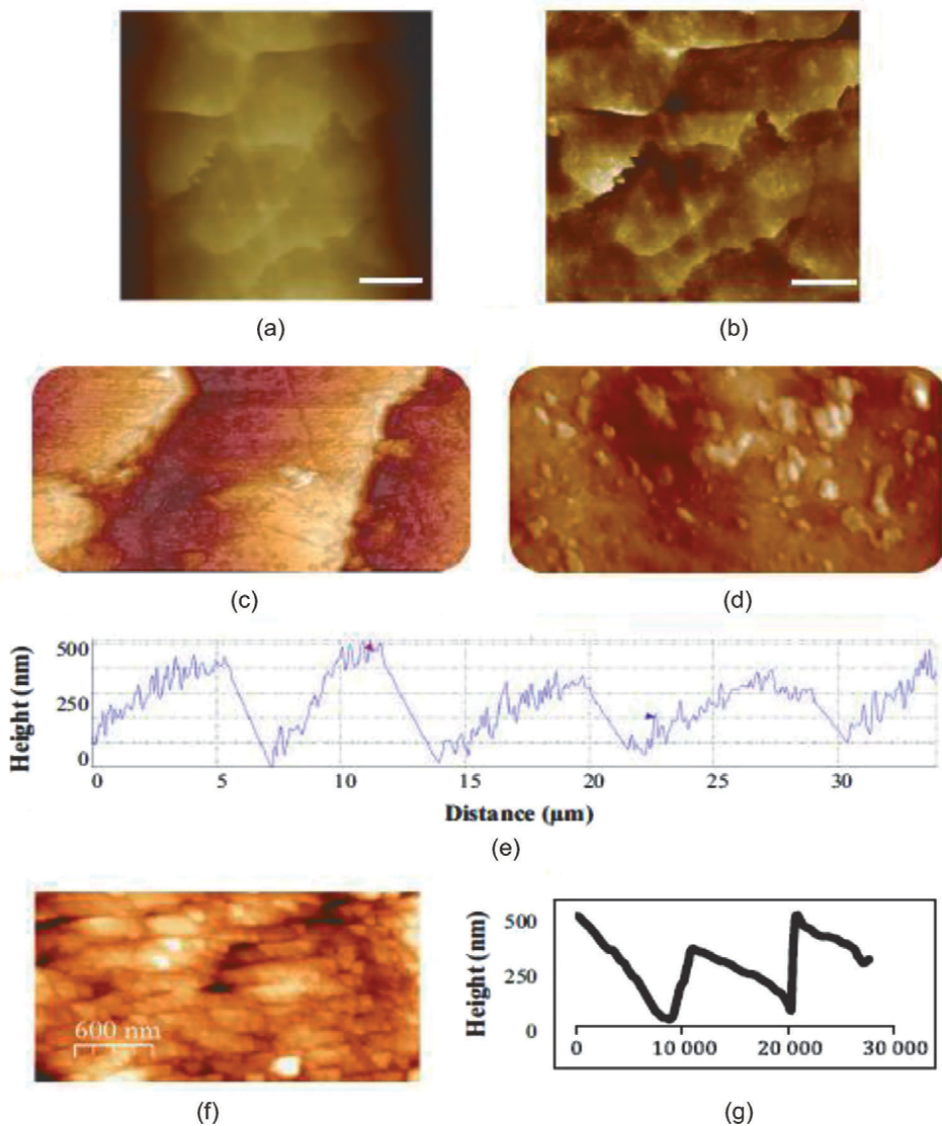


Figure 6.
 (a) AFM image of unwashed human hair. Scale bar is 5 μm . (b) The same image after flattening, where the debris on the hair is now more prominent. (c) Side-lit 3D representation of an area of hair revealing that particulates and deposits are relatively uniformly distributed across the hair surface. Scale bar is 3 μm . (d) Smaller scale image showing deposits on hair, away from particulates and cuticle edges. Scale bar is 200 nm. (e) Cross-section through topography of a 35 μm long section of hair with four cuticle edges in the range 200–500 nm thick with a lateral spacing approximately 7 μm , and where the deposits can be seen as ripples/bumps. (f) AFM topography image revealing woodgrain striations, characteristic of the exocuticle. (g) Cross-section through a clean hair devoid of deposits, for comparison to **Figure 3e**.

the hairs are exposed to. Though the direct forensic relevance of this work was not established but the study do created extensive database of hair image along its mechanical properties [36].

Jeong et al. [18] have given an interesting contribution by studying the effects of aging on normal Korean hair diameter and surface features using AFM. They

examine 60 Korean volunteers of various ages who had no hair diseases and studied hair diameter, hair surface, cuticular descriptors and micro-scale mechanical properties to determine their associations with aging. They found that hair diameter increases for the first 20–30 years of life and later showed decrease. AFM images of most of the younger subjects showed clear scale edges of hair while of older subjects revealed dilapidated structures, poorly defined scale edges and undulated surfaces. The cuticular descriptors, surface roughness showed increase significantly with age. Also the force to distance analysis confirmed its dependence on age. They concluded that aging causes changes in hair diameter and surface structure. These work done by Jeong et al. do contribute in estimating the age from forensic trace evidences like hair. The hair surface area studies were done by Tomes et al. using both SEM and AFM which showed little difference in quality of surface profiles obtained. For forensic hair imaging, the minimally invasive AFM technique can be preferred over SEM [37].

AFM is also used to investigate the effects of ethnicity, fatigue and water absorption on the tensile strength of hair and found in different ethnic hair types namely Caucasian, Asian and African and the results indicated that they have different mechanical properties [38]. Seshadri did the similar study on the tensile strength of hair by imaging the cuticular structure of hair. They found that hair shows stress-strain curve for keratinous fiber. Also the chemical, mechanical damage and conditioner treatment does not have any effect on the stress-strain curve or its tensile properties [39]. DelRio and Cook [19] provided interesting data of hair samples untreated virgin hairs and conditioned and bleached hairs. They stated an indentation modulus of 2.4 ± 1.1 GPa and 1.8 ± 0.9 GPa respectively for virgin and the bleached hairs samples while for the conditioned hairs, the indentation modulus varied between 0.05 and 0.5 GPa. They performed all the measurements on a 5 by 5 μm area.

3.4 Diatom test

Diatoms are a group of algae found in oceans and fresh waters possessing tough silica wall (SiO_2) which is resistant to decay. Diatoms plays very crucial role in cases of drowning to determine whether it is antimortem or postmortem drowning, hence proving useful in forensic investigation. The recovery of diatoms from different organs, their quantitative and qualitative composition examination prove to be very trustworthy proof to determine the place and time of drowning in many cases [40]. They are studied in forensic geoscience in relation to transfer from different environments to clothing to obtain information of the crime scene and the perpetrator [41]. Newer techniques namely nuclear magnetic resonance, AFM, inductively coupled plasma (ICP) hyphenated technologies, fluorimetry and automatic diatom identification and classification are also been used for diatom study. AFM is used to study the diatoms morphological characteristics which can act as an indicator of its location, its growth cycle henceforward demonstrating its usefulness in forensic application. AFM has the potential to differentiate diatoms on the basis of its feature and can individualized atoms by scanning the objects that are 8" long and having a diameter of 0.5". Even the largest diatoms can be scanned in this range also the technique has the additional advantage of scanning the object in vertical and horizontal axis [42].

Almqvist et al. explored the possibilities of AFM to study diatoms in relation to its biomineralization and micromechanical properties. They studied the silica shell of the diatom *Naviculapellucosa* (Bréb.) Hilse. The structure was imaged and the shell's micromechanical properties were studied in semi-quantitatively manner. The results indicated that the diatom's overall hardness and elasticity are same as that of silicas.

Figure 7 shows the separated epitheca and hypotheca of one cell. They also showed that certain areas of the shell were significantly harder or more elastic which can be detected in different crystalline phases [43].

3.5 Finger print

In most the crime, fingerprints are the most common type of evidence found on to the crime scene. A fingerprints are impression of friction ridges on human finger. The discovery, visualization of latent fingerprints constitutes an important part of any crime investigation. Finger prints consist of exogenous and endogenous compounds. The endogenous part mainly includes the skin remnants, sweat gland and sebaceous secretions along with many different inorganic and organic substances. The finger prints remains unchanged throughout the life of an individual hence they play very important role in person identification. Usually visible and latent fingerprints are found at the crime scene. The visible prints do not require any aid to be visualized while the latent prints are invisible thus require physical, chemical and instrumental techniques to be visualized [44]. Very few researchers have tried to explore the use of AFM in fingerprint investigation.

Atomic force microscopy technique highlight its use to study the deposition characteristics and detection efficiency of fingerprint details. Direct application of the AFM is not soon in the examination of comparison of the fingerprint but the use of AFM is shown in the fingerprint cases by some researchers. Jones et al. used AFM to characterize the various substrates erstwhile of fingermark deposition in relation to the surface roughness, maximum height variation, skew and kurtosis. The finger prints were developed using iron oxide powder on formica, polyethylene and unplasticised polyvinylchloride surfaces [45]. As per Goddard et al. the limitation of the AFM height imaging to study the fingerprint ridge is the surface roughness when it is in the same order of magnitude as the height of the ridges as shown in **Figure 8** [46]. The same problem avail with lifted finger prints as well as the prints present on the metal surfaces. The roughness of the surface on which the finger prints are present is main obstacle for routine applications of AFM in fingerprint analyses. In case were the surface roughness can be reduced atomic force microscopy can be useful in recovering

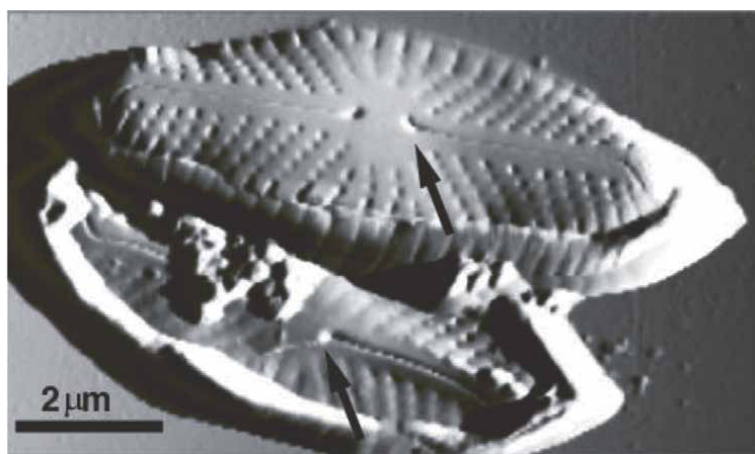


Figure 7.
The separated epitheca and hypotheca of one cell [43].

the missing details that are essential to reconstruct a fingerprint. This problem was overcome by using scanning Kelvin probe force microscopy performed by Williams and McMurray. They studied the fingerprints deposited on metallic surfaces. They were able to retrieve sufficient ridge detail of fingerprint which were physically removed. Furthermore they demonstrated the use of Volta potential mapping to examine the fingerprint present on planar brass substrates [47].

3.6 Gunshot residues

Gunshot residues (GSR) mainly contains unburned or partially burnt propellant powder, particles from the ammunition primer, grease, smoke, metal residues and lubricants from the fired cartridge while the organic compounds in GSR originate from propellant and firearm lubricants [48, 49]. The analysis of the inorganic GSR can evidence to be useful in forensic reconstruction of shooting incidents. Techniques such as neutron activation analysis, ICP, atomic absorption spectrometry (AAS), and SEM combined to energy dispersion analysis are used for inorganic GSR analysis [50–53]. Neutron activation analysis are used for analysis of barium and antimony and for lead analysis conventional AAS and ICP are useful. High-resolution ICP-MS are reported to identify lead, barium and bismuth concentrations upto 1 ng/mL [54]. SEM-EDX is considered as golden standard of forensic GSR analysis as it has the ability to characterize GSR both chemically and morphologically. The SEM analysis is a time-consuming process. The organic GSR analysis are done by using gas chromatography, HPLC or GS-MS [55]. For both inorganic and organic GSR characterization time-of-flight secondary ion mass spectrometry, Raman micro-spectroscopy and ablation-ICP/MS are reported [56, 57]. Apart from these, AFM technique have shown a great applicability in forensic GSR analysis on the basis of its morphological structure in relation to solving the crime [58].

The estimation of shooting distance plays a vital role in firearm cases also when combined with other evidence it helps in reconstructing shooting events. The bullet entrance hole appearance and the GSR patterns around the wound are usually used

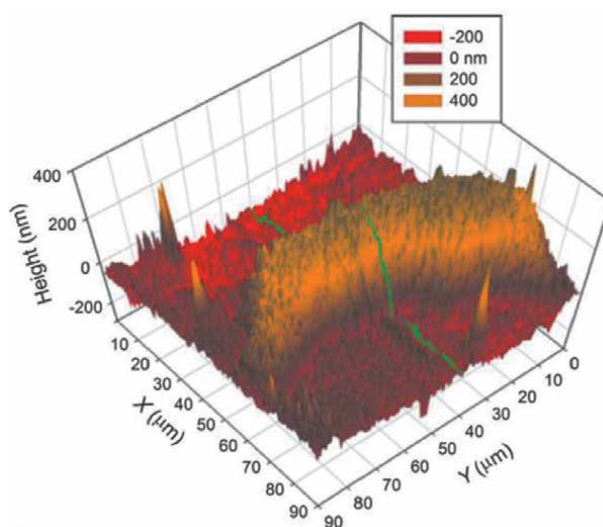


Figure 8.
AFM images from the polished and printed brass surface showing 3D image of part of ridge detail.

to estimate the firing distance [59–61]. Most commonly used color test Griess test along with series of modified and improved Griess tests are used to determine the presence of nitrites and hence for estimation of muzzle to target distance. Mou et al. reported the application of atomic force microscopy and Fourier transform infrared attenuated total reflectance spectroscopy. They use the techniques for firing distance estimation or muzzle-to-target shooting distance as well as the manufacturers of the cartridge and its powder. In their work, standard procedures contain test firing at various distances along with the evidence pattern comparison. They observed that for the samples the Winchester SuperX and CCI cartridges GSR particle sizes increased as the shooting distance decreased. From the AFM images of GSR they found that particles size distribution is inversely proportional to the shooting distance. AFM can be applied for the investigation of various materials unrelatedly to their conductivity. AFM is a non-destructive technique which helps in measurements in either air, liquid, or controlled atmospheres thus allowing the intact sample to be characterized without any pretreatments of the samples. The AFM images of GSR particles showed with different shapes like spherical, twins-like, irregular, boomerang-like, non-spherical, heart-like, rod-like and cube/rectangular-like as shown in **Figure 9**. The results indicated that the particles size distribution was inversely proportional to the shooting distance [62]. As per Jones when AFM is used for the GSR particles analysis the powder get stuck on the probe tip, thus drastically changing the shape and size of the powder particles resulting into the newer shape formation hence significantly alters the subsequent analysis [63]. This could be considered as a drawback of AFM for the analysis of fine GSR particles. But these same was overcome by Mou et al. which prove to be useful in firing distances determination.

D’Uffizi et al. in their work examine the GSR particles deposited on the bullet and on the shooter hands using combination of scanning electron microscopy + energy-dispersive spectroscopy, atomic force microscopy and selected-area X-ray photoelectron spectroscopy. The GSR samples were collected using double-sided tape. They studied the micromechanical and micromorphological features of gunshot residue particles. Of importance in this investigation the use of AFM itself (Nanoscope IIIa Digital Instruments microscope, tapping mode, frequency: 250–390 kHz) was done to examine the height and phase imaging [64]. Some research has shown the applicability of AFM in context to forensic gunshot and explosive investigation with regards to physicochemical characterization that can be detected on hairs and in between the ridges of fingermarks.

The mechanical properties of the organic and inorganic particles present in GSR and explosives, were studied by Xu et al. They showed the application of AFM techniques, including force volume mode, phase imaging as well as Kelvin probe force microscopy with resonance enhancement for dielectric property mapping was used to map the local physical properties of mock explosive materials. These work will allow the identification of sub-micrometer heterogeneities in relation to their electrical and mechanical properties [65].

3.7 Explosion

One of the recent advancements showed the use of AFM as a characterization technique for explosives detection. The surface morphology of explosives such as triamino-trinitro-benzene, plastic-bonded explosives, ammonium perchlorate was analyzed through AFM [66–68]. The surface morphology of such explosives helps in understanding the different characteristics of explosives which can help in identification [69].

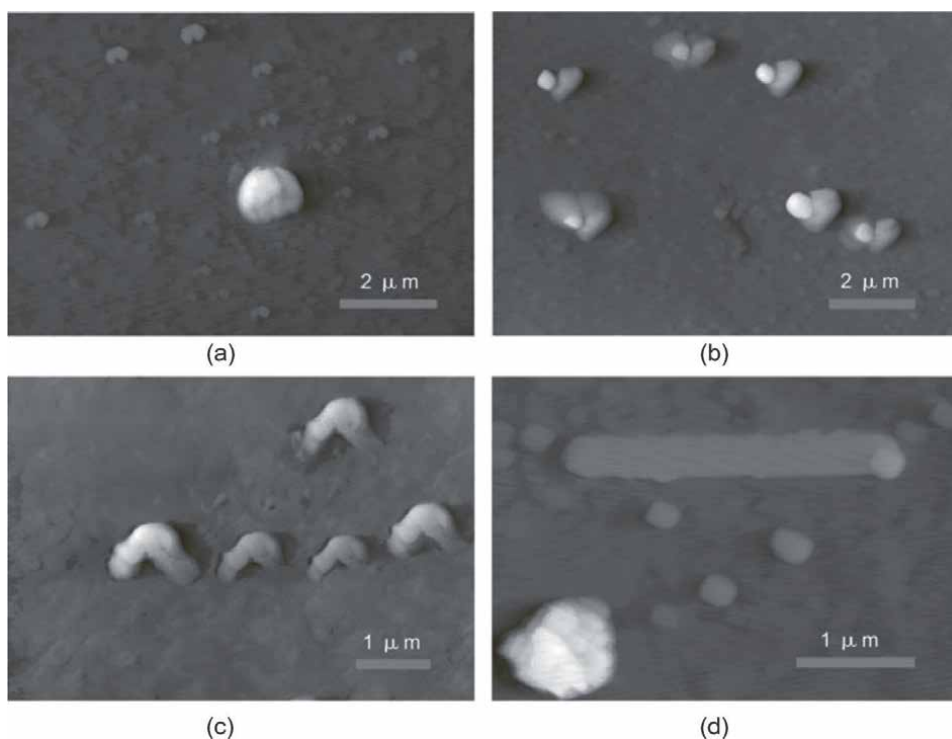


Figure 9. AFM images of GSR particles showing various particle shapes, twins-like (a), heart-like (b), boomerang-like (c), and rod and cube like (d). The bullet type is CCI and the shooting distance is 10 ft.

Accumulation of explosives namely 2,4,6-trinitrotoluene (TNT) and triacetone triperoxide (TATP) in chemically treated hair sample was studied by Oxley et al. [70] using AFM and SEM. The interaction of TNT and TATP as a function of chemical pretreatment with acetonitrile, neutral and alkaline hydrogen peroxide, methanolic potassium hydroxide and potassium permanganate was studied and further the morphological changes which resulted from these treatments were studied. Hair examination surface showed different degrees of smoothening. Density functional theory calculations were employed to know the possible nucleation sites of TATP microcrystals on the hair samples. From their calculations study they concluded that the dark hair adsorbs explosives better than light hair. The authors have showed the use of AFM on their previously described applications of AFM in hair structure investigations [17, 36, 71]. Studied reported shows that AFM play a vital role in trace evidence analysis in post-explosion cases. These studies indicate that recently the potential of the AFM technology has been explored in relation to the forensic evidences analysis and the full potential of technology is yet to be discovered. The possibility of mapping a number of physical and chemical material properties prove to be a worthy contribution in distinguishing the different components in complex heterogeneous structure of explosive residues samples. The AFM technology is only a complementary technique its use can be enhanced if combined with other analytical technique which can prove to be of great importance in forensic context for not only examination of GSR or post explosives residues but also for other trace evidences found on to the crime scene.

Valle et al. [72] used AFM to investigate and identify several characteristics of firearms. Replica molding of the head of these cases was done using the fired cartridge cases and the surface morphology of replicated areas at the breech faces were studied. In this framework, the method showed reproducibility of different copies of the similar sample indicating that they are indistinguishable over all the accessible length scales.

Researchers have also shown the utility of AFM in fire investigation cases. In fire cases the determination of source of fires plays very important role in order to validate [73, 74]. In fire cases, molten electric marks are found on the electric arc bead. Examination of these marks can help to determine the source of the fire. Gao et al. used OM and AFM to examine a molten mark on copper wire by artificially creating the molten mark inflicted on the wire under laboratory conditions. The AFM results showed that the technique is an brilliant add-on to examine the copper molten mark and thus provide excellent data to confirm the actual causes of fire [75].

3.8 Soil sample analysis

Soils vary among different areas and possess characteristics due to their natural effects and transfers made by human being and other living beings with time. Examination of soil in forensic context can help in determination of crime location. Investigative and interpreting the soil or sediment can help in their origin determination [76]. Konopinski et al. studied the grain surface texture of quartz sand using AFM. AFM analysis provide topographical data from the grain surface that permits statistical analysis, 3D reconstruction and quantitative valuations of the microscopic surface textures. AFM offers numerous statistical methods which can discriminate between grain surface textures and also helps in creating automated database to compile and generate reports. AFM has great potential to be used for forensic analysis where sample preservation is extremely valuable. As per Konopinski et al. using AFM helps in quantifiable measurement of quartz grain surface textures which opens up a number of possibilities for forensic quartz grain surface texture analysis as it provides a corroborative independent verification of quartz type classifications as shown in **Figure 10** [14].

Sullivan et al. in their work investigated the surface characteristics of plastic wrapping materials of forensic interest in soil environments in order to determine the environmental factors that influence the degradation process of such polymers. They buried polyethylene bags and poly (vinyl chloride) sheeting in model environments surrounding different soil types, moisture content, pH and temperature. Atomic force microscopy was used to study the changes which results on the polymer surface at a nanometre level. They found that over a 2-year burial period, the degradation of polyethylene was greater by an increased moisture content and a raised soil pH. The plasticizer content of poly (vinyl chloride) was got affected by burial, thus leaching of the same was observed in all environments continually over the burial period. The surface roughness measurement of plastics using atomic force microscopy was sensitive to the burial environment and demonstrates the potential of technique to measure relatively subtle changes to burial items when exposed to different environments conditions [77].

3.9 Pressure sensitive adhesives analysis

Pressure sensitive adhesive tapes are utilized for various purposes in criminal activities such as packaging of controlled drugs, the restraint of an individual during robbery and offences against a victim, the enclosure of explosive devices and for

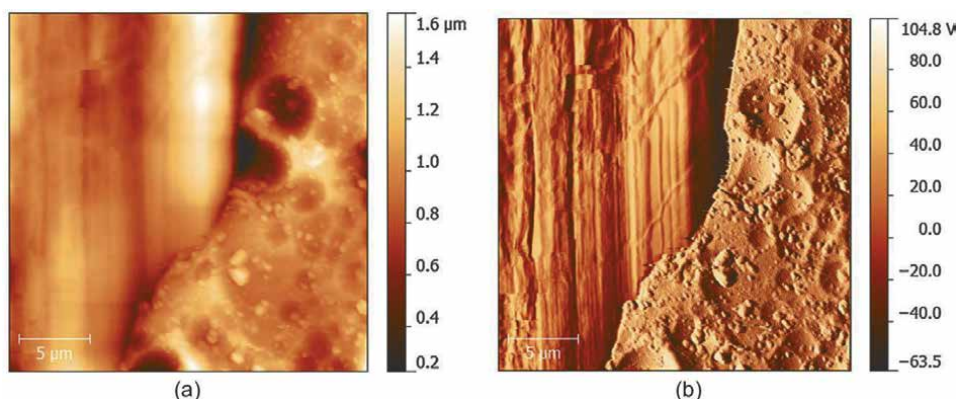


Figure 10. Topography (a) and amplitude (b) maps offset from clearly visible is the interface between two different surface textures.

concealment. To identify chemical constituents techniques such as Fourier transform infrared spectroscopy and pyrolysis–gas chromatography–mass-spectrometry are applied in forensic science laboratories for the discrimination of PSAs. However, AFM can offer supplementary and useful analytical data on PSAs as it has the capability to map the adhesives surface morphological and mechanical properties also AFM can give nanoscopic information. With respect to forensic application it holds the ability to interpret the physical data obtained from evidence found at a crime scene and linking it to a particular suspect [16]. **Figure 11** shows the AFM phase images for transparent cello, brown packaging tape and electrical insulation tape.

3.10 Forensic analysis of fibres

Fibers are an important trace evidence that can provide valued evidence to support an association of individual to a crime scene. Standard forensic examinations of man-made fibers usually involves microscopic techniques such as visible, polarized light and fluorescence microscopy as well as micro-spectrophotometry. Infrared spectroscopy is also used to identify the fiber polymer type present if two fibers are indistinguishable by microscopic techniques. Man-made fibers namely polyamides, polyacrylics and polyesters are analyzed using techniques such as FTIR, circular dichroism, Raman spectroscopy, differential scanning calorimetry, transmission electron microscopy and wide angle X-ray diffraction [78]. Forensic comparison of fibers is mainly focused on morphological analysis and spectral analysis. Shady Farah et al. in their study, analyzed polyethylene terephthalate (PET) fiber on three different materials such as plain fibers of pet, a common textile fiber and plastic material. They studied the morphological feature of the fiber using AFM [79].

The ability of the AFM to reconnoiter the nanoscopic morphological changes in the surfaces of fabrics was studied by Canetta et al. This study was focused on two natural namely cotton and wool and a regenerated cellulose (viscose) textile fibres. All the fiber samples were exposed to different environmental stresses for different lengths of times. The surface texture parameters of the environmentally stressed fabrics was measure quantitatively as a function of the exposure time from the obtained AFM images. In the AFM images the nanoscale the finest details of the surfaces of three weathered fabrics was clearly distinguishable between the detrimental

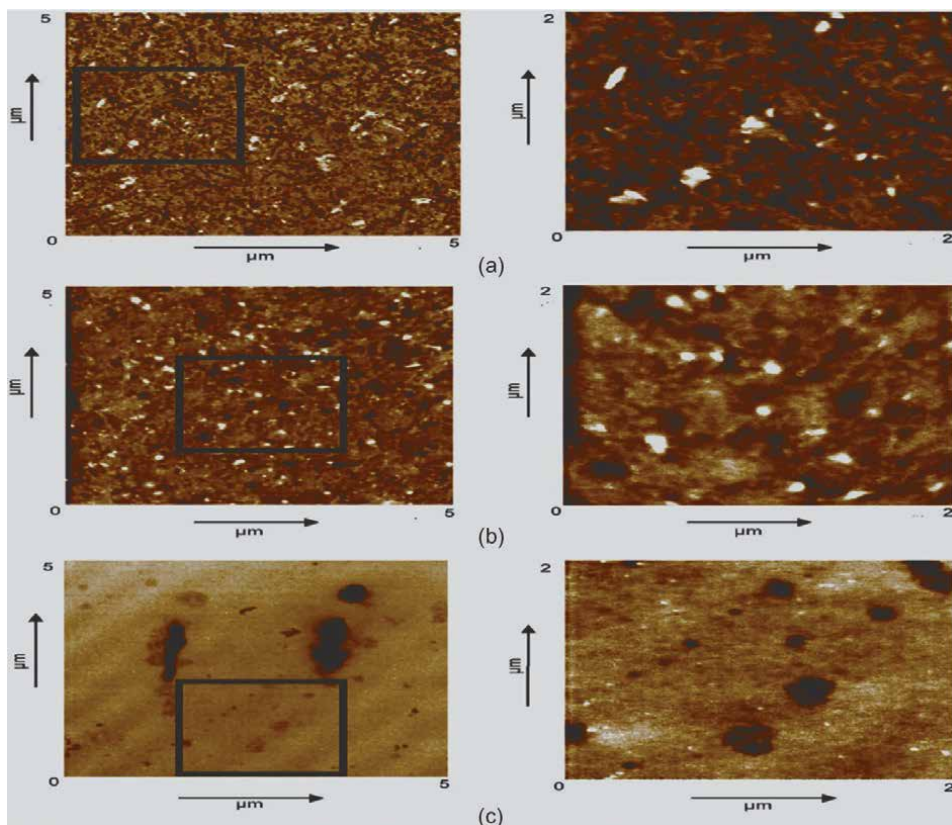


Figure 11. AFM phase images for (a) transparent cello, (b) brown packaging tape and (c) electrical insulation tape.

effects of the executed environmental conditions. The heights and roughness's of the unexposed and exposed fiber surfaces was measured by analyzing the obtained AFM images. **Figure 12** shows the AFM height images of cotton fibre exposed to loam and riverside soils, and pond and sea waters for 2 and 6 weeks. This study confirmed that the AFM can prove to be a very powerful tool in forensic examination of textile fibers to provide significant fiber examination as an evidence due to its proficiency of distinguishing between different environmental exposures or forced damages to fibers [80].

3.11 Data recovery from damaged SIM cards

In crimes involving digital evidences the data recovery plays very crucial role. Damaged SIM cards are highly useful evidence in such cases. The data obtained from such SIM cards give insights about the link between criminal and aids in future investigation. Nardi et al. used AFM for the enhancement and characterization of a forensically authenticated technique for sample processing and data extraction from a damaged SIM card. They develop a process to view the underside of the embedded EPROM/flash memory arrays present in smart card microcontrollers [81–83].

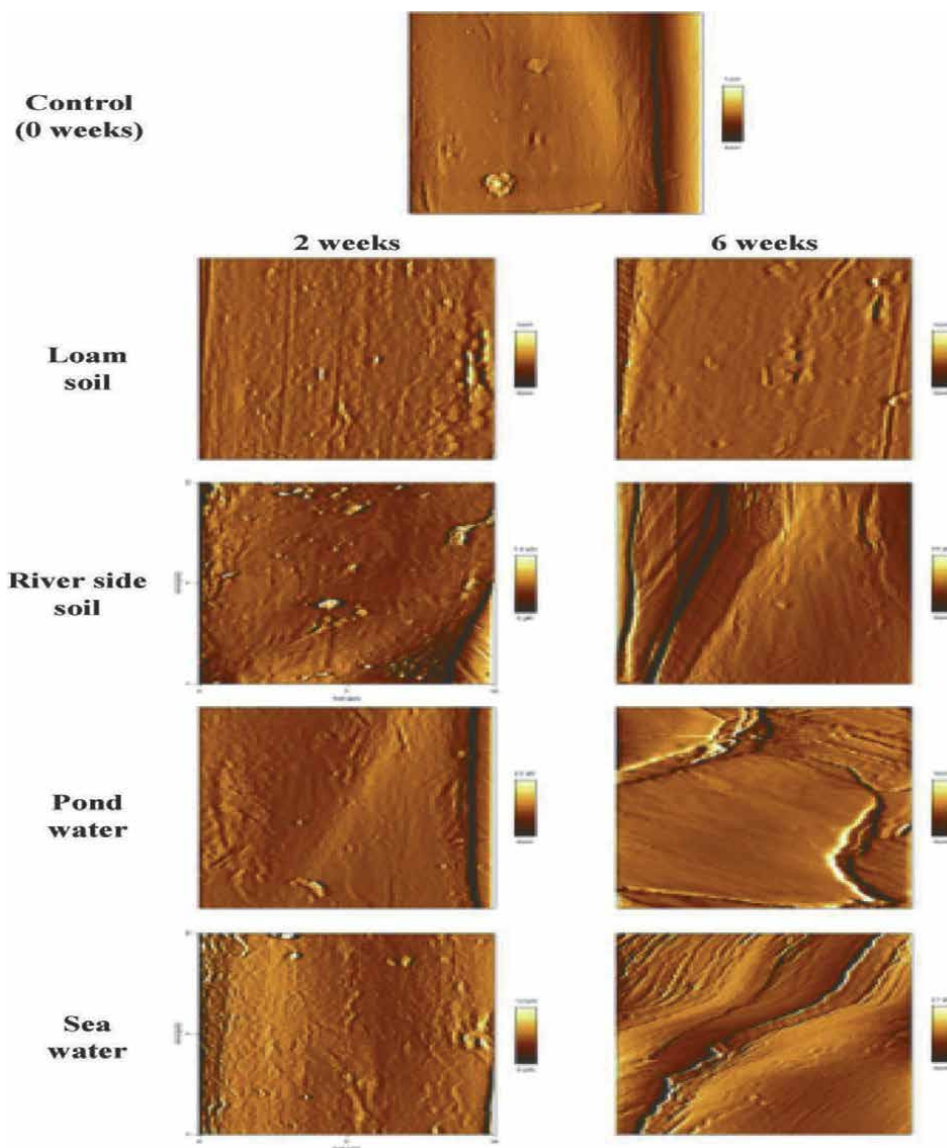


Figure 12.
AFM height images of cotton fibre exposed to loam and riverside soils, and pond and sea waters for 2 and 6 weeks.

4. Advantages and limitations

Atomic force microscopy works by running a sharp tip attached to a cantilever and sensor over the sample surface and measures the surface forces between the probe and the sample. As the cantilever runs laterally the sample surface, it moves up and down due to the surface features and the cantilever deflects accordingly. This deflection is computed using an optical sensor, with the laser beam being reflected on the back of the cantilever onto the light detector. AFM provides various advantages over other

techniques. AFM can operate in ambient air or under liquid, it does not need to be operated in a vacuum hence it is increasingly being used to image biological samples as well as nanoparticles. AFM has resolution in the order of fractions of a nanometer and provide a 3D imaging technique. The AFM allows the topographic characterization of surfaces at resolutions not attainable by optical microscopy. The lateral resolution of the AFM is limited by the tip size and shape and is typically on the order of a few nanometers. The height (z) resolution in AFM is nearly 1 Å, limited only by electronic and thermal noise in the system. AFM can only scan a single nanosized image at a time of about 150 × 150 nm and possess chances of damaging the tip and the sample during detection. Further it has a limited magnification and vertical range. Furthermore the speed of scanning of AFM is very slow compared to SEM and sample analysis cannot be done for areas greater than 100 μm. The images also gets affected by non-linearity, hysteresis, and creep of the piezoelectric material. Another drawback is that the images are generated because of the interaction of probe with sample which might not be the true topography of the sample. Also the probe tip can results in shape changes in samples like fine powder. The surface roughness over which a forensic traces are deposited may obstruct a proper examination of an image height. This problem could partly be overcome by use of phase imaging. Nevertheless, the addition of optical microscopy and Raman spectroscopy or surface enhanced Raman spectroscopy along with the AFM can prove to be useful for forensic examinations.

5. Conclusion

Undeniably, the AFM power to measure topography, morphology, adhesion forces, elastic modulus, dielectric properties and energy dissipation characteristics via minimal invasion. Furthermore, the 3-Dimensional multi-parameter function provide information add-on in cases of trace fusion imaging. Considering the practicality, sampling and sample logistics are still remains desirable in AFM, though with respect to SEM the tedious work of sample preparation as well as high vacuum settings are not required. AFM has its advantages while studying, optimizing, understanding and validating techniques for examination of trace evidences found at the scene of crime. Also, microtraces evidences physiochemical features imaging can be done which can assist in classification and comparison. Though it has such advantages, roughness of substrate do hamper one or other way while studying the sample height measurements. Certain researchers have answer to this solution by accompanying surface roughness along with larger scan areas in supplementary phase imaging. In practice, AFMs can image rough surfaces as long as the roughness does not surpass the limit of scanner in vertical, Z -direction. But the probe will crash if the surface roughness surpasses the scanning limit. To grip the forensic applicability of AFM in real case work superfluous research as well as laboratory and crime scene authentication studies are prerequisite. AFM could yield surplus possibilities for forensic association and reconstruction, assisting in forensic analysis at activity level.

Conflict of interest


The authors declare no conflict of interest.

Author details

Niha Ansari
National Forensic Sciences University, Gandhinagar, India

*Address all correspondence to: niha.ansari@nfsu.ac.in

IntechOpen

© 2022 The Author(s). Licensee IntechOpen. This chapter is distributed under the terms of the Creative Commons Attribution License (<http://creativecommons.org/licenses/by/3.0>), which permits unrestricted use, distribution, and reproduction in any medium, provided the original work is properly cited. 

References

- [1] Binning G, Quate CF, Gerber C, Weibel E. Surface studies by scanning tunneling microscopy. *Physical Review Letters*. 1982;**49**:57-61
- [2] Binning G, Quate CF, Gerber C. Atomic force microscope. *Physical Review Letters*. 1986;**56**:930-933
- [3] Starostina N, West P. Part II: Sample Preparation for AFM Particle Characterization. 3350 Scott Blvd., Suite 29, Santa Clara, CA 95054: Pacific Nanotechnology, Inc.; 2016
- [4] Pitkethly M. Nanotechnology and forensics. *Materials Today*. 2009;**12**:6
- [5] Chen Y. Forensic applications of nanotechnology. *Journal of the Chinese Chemical Society*. 2012;**58**:828-835
- [6] Inman K, Rudin N. Principles and Practice of Criminalistics—The Profession of Forensic Science. Boca Raton, Florida, USA: CRC Press; 2001
- [7] Inman K, Rudin N. The origin of evidence. *Forensic Science International*. 2002;**126**:11-16
- [8] Saadat S, Pandey G, Tharmavaram M. Microscopy for forensic investigations. In: *Technology in Forensic Science: Sampling, Analysis, Data and Regulations*. 2020. pp. 101-127
- [9] Bailey SW. *Micas*. Washington, DC: Mineralogical Society of America; 1984
- [10] Lyubchenko YL, Gall AA, Shlyakhtenko LS, Harrington RE, Oden PI, Jacobs BL, et al. Atomic force microscopy imaging of double stranded DNA and RNA. *Journal of Biomolecular Structure & Dynamics*. 1992;**9**:589-606
- [11] Cullen DC, Lowe CR. AFM studies of protein adsorption. 1. Time-resolved protein adsorption to highly oriented pyrolytic-graphite. *Journal of Colloid and Interface Science*. 1994;**166**:102-108
- [12] Yang J, Takeyasu K, Shao Z. Atomic force microscopy of DNA molecules. *FEBS Letters*. 1992;**301**:173-176
- [13] El Kirat K, Burton I, Dupres V, Dufrene YF. Sample preparation procedures for biological atomic force microscopy. *Journal of Microscopy*. 2005;**218**:199-207
- [14] Konopinski DI, Hudziak S, Morgan RM, Bull PA, Kenyon AJ. Investigation of quartz grain surface textures by atomic force microscopy for forensic analysis. *Forensic Science International*. 2012;**223**:245-255
- [15] Chen S-Z, Tsai T-L, Chen Y-F. Forensic application of atomic force microscopy-questioned document. *Journal of the Chinese Chemical Society*. 2012;**59**:283-288
- [16] Canetta E, Adya AK. Atomic force microscopic investigation of commercial pressure sensitive adhesives for forensic analysis. *Forensic Science International*. 2011;**210**:16-25
- [17] Durkan C, Wang N. Nanometre-scale investigations by atomic force microscopy into the effect of different treatments on the surface structure of hair. *International Journal of Cosmetic Science*. 2014;**36**:598-605
- [18] Jeong KH, Kim KS, Lee GJ, Choi SJ, et al. Investigation of aging effects in human hair using atomic force microscopy. *Skin Research and Technology*. 2011;**17**:63-68

- [19] DelRio FW, Cook RF. Quantitative scanning probe microscopy for nanomechanical forensics. *Experimental Mechanics*. 2017;**57**
- [20] Fujita Y, Tsuchiya K, Abe S, Takiguchi Y, Kubo S, Sakurai H. Estimation of the age of human bloodstains by electron paramagnetic resonance spectroscopy: Long-term controlled experiment on the effects of environmental factors. *Forensic Science International*. 2005;**152**:39-43
- [21] Anderson S, Howard B, Hobbs GR, Bishop CP. A method for determining the age of a bloodstain. *Forensic Science International*. 2005;**148**:37-45
- [22] Edelman G, van Leeuwen TG, Aalders MC. Hyperspectral imaging for the age estimation of blood stains at the crime scene. *Forensic Science International*. 2012;**223**:72-77
- [23] Bremmer RH, de Bruin KG, van Gemert MJ, van Leeuwen TG, Aalders MC. Forensic quest for age determination of bloodstains. *Forensic Science International*. 2012;**216**:1-11
- [24] Wu Y, Hu Y, Cai J, Ma S, Wang X, Chen Y, et al. Time-dependent surface adhesive force and morphology of RBC measured by AFM. *Micron*. 2009;**40**:359-364
- [25] Chen Y, Cai J. Membrane deformation of unfixed erythrocytes in air with time lapse investigated by tapping mode atomic force microscopy. *Micron*. 2006;**37**:339-346
- [26] Lamzin IM, Khayrullin RM. The quality assessment of stored red blood cells probed using atomic-force microscopy. *Anatomy Research International*. 2014;**2014**:869683
- [27] Girasole M, Dinarelli S, Boumis G. Structure and function in native and pathological erythrocytes: A quantitative view from the nanoscale. *Micron*. 2012;**43**:1273-1286
- [28] Smijs T, Hosseinzoi A, Galli F. Forensic application of atomic force microscopy for age determination of bloodstains. *Journal of Forensic Investigation*. 2017;**5**(1):6
- [29] Cavalcantia DR, Silva LP. Application of atomic force microscopy in the analysis of time since deposition (TSD) of red blood cells in bloodstains: A forensic analysis. *Forensic Science International*. 2019;**301**:254-262
- [30] Strasser S, Zink A, Kada G, Hinterdorfer P, Peschel O, Heckl WM, et al. Age determination of blood spots in forensic medicine by force spectroscopy. *Forensic Science International*. 2007;**170**:8-14
- [31] Yadavalli VK, Ehrhardt CJ. Atomic force microscopy as a biophysical tool for nanoscale forensic investigations. *Science & Justice*. 2021;**61**(1):1-12. DOI: 10.1016/j.scijus.2020.10.004
- [32] Kasas S, Khanmy-Vital A, Dietler G. Examination of line crossings by atomic force microscopy. *Forensic Science International*. 2001;**119**:290-298
- [33] Brandao JM, Almeida NSM, Dixini PVM, et al. Documentoscopy by atomic force microscopy (AFM) coupled with Raman microspectroscopy: Applications in banknote and driver license analyses. *Analytical Methods*. 2016;**8**:771-784
- [34] Ellen D. *Scientific Examination of Documents Methods and Techniques*. Boca Raton, USA: CRC Press; 2006
- [35] LinacLinacre A, Ottens R. *DNA: Hair Analysis, Encyclopedia of Forensic and Legal Medicine*. 2nd ed. Elsevier; 2016. pp. 337-342

- [36] Gurden SP, Monteiro VF, Longo E, et al. Quantitative analysis and classification of AFM images of human hair. *Journal of Microscopy*. 2004;**215**:13-23
- [37] Tomes C, Jones JT, Carr CM, et al. Three-dimensional imaging and analysis of the surface of hair fibres using scanning electron microscopy. *International Journal of Cosmetic Science*. 2007;**29**:293-299
- [38] Seshadri IP, Bhushan B. Effect of ethnicity and treatments on in situ tensile response and morphological changes of human hair characterized by atomic force microscopy. *Acta Materialia*. 2008;**56**:3585-3597
- [39] Seshadri IP, Bhushan B. In situ tensile deformation characterization of human hair with atomic force microscopy. *Acta Materialia*. 2008;**56**:774-781
- [40] Krstica S, Dumab A, Janevskab B, Levkova Z, Nikolovab K, Noveska M. Diatoms in forensic expertise of drowning—A Macedonian experience. *Forensic Science International*. 2002;**127**:198-203
- [41] Scott KR, Morgan RM, Jones VJ, Cameron NG. The transferability of diatoms to clothing and the methods appropriate for their collection and analysis in forensic geoscience. *Forensic Science International*. 2014;**241**:127-137
- [42] Kumar M, Deshkar J, Naik SK, Yadav PK. Diatom test – past, present and future: A brief review. *Indian Journal of Research and Reports in Medical Sciences*. 2012;**2**(3):28-32
- [43] Almqvist N, Delamo Y, Smith BL, Thomson NH, Bartholdson A, Lal R, et al. Micromechanical and structural properties of a pennate diatom investigated by atomic force microscopy. *Journal of Microscopy*. 2001;**202**(3):518-532
- [44] Dutelle AW. Fingerprint evidence. In: *An Introduction to Crime Scene Investigation*. Burlington, USA: Jones & Bartlett Learning; 2014. pp. 169-202
- [45] Jones BJ, Downham R, Sears VG. Effect of substrate surface topography on forensic development of latent fingerprints with iron oxide powder suspension. *Surface and Interface Analysis*. 2010;**42**:438-442
- [46] Goddard AJ, Hillman AR, Bond JW. High resolution imaging of latent fingerprints by localized corrosion on brass surfaces. *Journal of Forensic Sciences*. 2010;**55**:58-65
- [47] Williams G, McMurray N. Latent fingermark visualisation using a scanning Kelvin probe. *Forensic Science International*. 2007;**167**:102-109
- [48] Dalby O, Butler D, Birkett JW. Analysis of gunshot residue and associated materials—A review. *Journal of Forensic Sciences*. 2010;**55**:924-943
- [49] Saverio RF, Margot P. Identification of gunshot residue: A critical review. *Forensic Science International*. 2001;**119**:195-211
- [50] Abrego Z, Ugarte A, Unceta N, Fernandez-Isla A, Goicolea MA, Barrio RJ. Unambiguous characterization of gunshot residue particles using scanning laser ablation and inductively coupled plasma-mass spectrometry. *Analytical Chemistry*. 2012;**84**:2402-2409
- [51] Aliste M, Chavez LG. Analysis of gunshot residues as trace in nasal mucus by GFAAS. *Forensic Science International*. 2016;**261**:14-18

- [52] Aksoy C, Bora T, Senocak N, Aydin F. A new method to reduce false positives due to antimony in detection of gunshot residues. *Forensic Science International*. 2015;**250**:87-90
- [53] French J, Morgan R. An experimental investigation of the indirect transfer and deposition of gunshot residue: Further studies carried out with SEM-EDX analysis. *Forensic Science International*. 2015;**247**:14-17
- [54] Sarkis JE, Neto ON, Viebig S, Durrant SF. Measurements of gunshot residues by sector field inductively coupled plasma mass spectrometry – Further studies with pistols. *Forensic Science International*. 2007;**172**:63-66
- [55] Taudte RV, Beavis A, Blanes L, Cole N, Doble P, Roux C. Detection of gunshot residues using mass spectrometry. *BioMed Research International*. 2014;**2014**:965403
- [56] Coumbaros J, Kirkbride KP, Klass G, Skinner W. Characterisation of 0.22 caliber rimfire gunshot residues by time-of-flight secondary ion mass spectrometry (TOF-SIMS): A preliminary study. *Forensic Science International*. 2001;**119**:72-81
- [57] Abrego Z, Grijalba N, Unceta N, Maguregui M, Sanchez A, Fernandez-Isla A, et al. A novel method for the identification of inorganic and organic gunshot residue particles of lead-free ammunitions from the hands of shooters using scanning laser ablation-ICPMS and Raman microspectroscopy. *Analyst*. 2014;**139**:6232-6241
- [58] Smijs T, Galli F, van Asten A. Forensic potential of atomic force microscopy. *Forensic Chemistry*. 2016;**2**:93-104
- [59] Bailey JA, Casanova RS, Bufkin K. A method for enhancing gunshot residue patterns on dark and multicolored fabrics compared with the modified Griess test. *Journal of Forensic Sciences*. 2006;**51**:812-814
- [60] Atwater C, Durina ME, Durina JP, Blackledge RD. Visualization of gunshot residue patterns on dark clothing. *Journal of Forensic Sciences*. 2006;**51**:1091-1095
- [61] Zeichner A, Glattstein B. Recent developments in the methods of estimating shooting distance. *Scientific World Journal*. 2002;**2**:573-585
- [62] Mou Y, Lakadwar J, Rabalais JW. Evaluation of shooting distance by AFM and FTIR/ATR analysis of GSR. *Journal of Forensic Sciences*. 2008;**53**:1381-1386
- [63] Jones BJ. Commentary on: Mou Y, Lakadwar J, Rabalais JW. Evaluation of shooting distance by AFM and FTIR/ATR analysis of GSR. *J Forensic Sci* 2008;**53**:1381-1386. *Journal of Forensic Sciences*. 2009;**54**:502
- [64] D'Uffizi M, Falso G, Ingo GM, Padeletti G. Microchemical and micromorphological features of gunshot residue observed by combined use of AFM, SA-XPS and SEM + EDS. *Surface and Interface Analysis*. 2016;**34**:502-506
- [65] Xu X, Mres J, Groven LJ, et al. Nanoscale characterization of mock explosive materials using advanced atomic force microscopy methods. *Journal of Energetic Materials*. 2015;**33**:51-65
- [66] Yang GC, Nie F, Huang H, Zhao L, Pang WT. Preparation and characterization of nano-TATB explosive. *Propellants, Explosives, Pyrotechnics*. 2006;**31**:390-394
- [67] Kumari A, Jain MS, Jain MK, Bhattacharya B. Nano-ammonium perchlorate: Preparation,

characterization, and evaluation in composite propellant formulation. *Journal of Energetic Materials*. 2013;**31**:192-202

[68] Van der Heijden AEDM, Creighton YLM, Marino E, Bouma RHB, Scholtes GJHG. Energetic materials: Crystallization, characterization and insensitive plastic bonded explosives. *Propellants, Explosives, Pyrotechnics*. 2008;**33**:25-32

[69] Tourné M. Developments in explosives characterization and detection. *Journal of Forensic Research*. 2014;**S12**:1-10

[70] Oxley JC, Smith JL, Kirschenbaum LJ, Marimiganti S, Efremenko I, Zach R, et al. Accumulation of explosives in hair – Part 3: Binding site study. *Journal of Forensic Sciences*. 2012;**57**:623-635

[71] Chen N, Bhushan B. Morphological, nanomechanical and cellular structural characterization of human hair and conditioner distribution using torsional resonance mode with an atomic force microscope. *Journal of Microscopy*. 2005;**220**:96-112

[72] Valle F, Bianchi M, Tortorella S, Pierini G, Biscarini F, D'Elia M. Nanotechnology for forensic sciences: Analysis of PDMS replica of the case head of spent cartridges by optical microscopy, SEM and AFM for the ballistic identification of individual characteristic features of firearms. *Forensic Science International*. 2012;**222**:288-297

[73] Pan G, Gao W, Zhao CZ, Di M. Comprehensive identification technology about electric fire. *The Journal of Fire Sciences*. 2005;**24**(4):495-497

[74] Shea JJ. Identifying causes for certain types of electrically initiated fires in

residential circuits. *Fire and Materials*. 2011;**35**:19-42

[75] Gao A, Zhao C, Di M, Gao W, Zhang M, Xia D. Microscopic investigation of a copper molten mark by optical microscopy (OM) and atomic force microscopy (AFM). *Procedia Engineering*. 2011;**11**:100-106

[76] Ritz K, Dawson L, Miller D, editors. *Criminal and Environmental Soil Forensics*. Dordrecht: Springer+Business Media BV; 2009

[77] Sullivan C, Thomas P, Stuart B. An atomic force microscopy investigation of plastic wrapping materials of forensic relevance buried in soil environments. *Australian Journal of Forensic Sciences*. 2018;**51**(5):596-605

[78] Steinmann W, Glauss B, Walter S, Wulfhrost J, Seide G, Gries T. Modern methods in fiber analysis for advanced quality control and process development. *Chemical Fibers International*. 2012;**62**:95-97

[79] Farah S, Tsach T, Bentolila A, Domb AJ. Morphological, spectral and chromatography analysis and forensic comparison of PET fibers. *Talanta*. 2014;**123**:54-62

[80] Canetta E, Montiel K, Adya AK. Morphological changes in textile fibres exposed to environmental stresses: Atomic force microscopic examination. *Forensic Science International*. 2009;**191**:6-14

[81] Nardi CD, Desplats R, Perdu P, Beaudoin F, Gauffier J. Oxide charge measurements in EEPROM devices. *Microelectronics and Reliability*. 2005;**45**:1514-1519

[82] Jose S. EEPROM failure analysis methodology–Can programmed

charges be measured directly by electrical techniques of scanning probe microscopy?. Proceedings of the 31 International Symposium for Testing and Failure Analysis. McEnery Convention Center, California, USA. November 6-10;2005. pp. 256-261

[83] Nardi CD, Desplats R, Perdu P, Gauffier J, Guerin CC. Descrambling and data reading techniques for flash-EEPROM memories. Application to smart cards. *Microelectronics and Reliability*. 2006;**46**:1569-1574

The Cytological Mechanism of Apospory in *Paspalum notatum* Analyzed by Differential Interference-Contrast Microscopy

Lanzhuang Chen and Liming Guan

Abstract

Bahia grass (*Paspalum notatum* Flugge) is an important tropical forage grass and sets seed by apospory. I) To clarify the mechanisms of aposporous embryo sac initial cell (AIC) appearance and apomictic embryo sac formation, and II) to make it clear the mechanism of multiple embryo seed set a development in polyembryonic ovules, several apomictic and sexual varieties of bahia grass were studied cytologically and quantitatively by Nomarski differential interference-contrast microscopy. The results were I) there was no difference between sexual and apomicts to megasporogenesis; and then, the megaspore degenerated in apomicts; at the same time, AIC originated from nucellar tissue appeared and its numbers increased as the ovary grew before anthesis; II) at anthesis, the sac derived from AIC located in the micropylar end (first sac) were 92.5 to 100%, and those in the chalazal ends (other sacs) were 40.4 to 86.0% among the apomicts; the first sac divided dominantly and were 56 to 87% comparable to 0 to 1% of the other sacs at 4 days after anthesis; however, 4 to 17% of the other sacs also showed embryo formations but endosperm. In final, the first sac occupied the whole space of the ovule, in which the embryos in the other sacs coexisted.

Keywords: apospory, aposporous embryo sac initial cell appearance (AIC), differential interference-contrast microscopy, *Paspalum notatum* Flugge, polyembryonic seed set

1. Introduction

Apomixis provides a method for cloning plants through seeds, so that it is of value for agriculture used to fix hybrid vigor and other hopeful breeding materials that are positioned in the middle breeding process [1, 2]. Apomixis is usually classified into three major mechanisms, apospory, diplospory and adventitious embryogeny [1]. Among the three mechanisms, apospory is considered as the most important one in agriculture because it does not undergo meiosis to propagate through the seed. Bahia grass (*Paspalum notatum* Flugge) is an apomictic perennial that sets seed by apospory, a form of gametophytic apomixis [3–6]. Studies on chromosome, cytology,

cross-compatibility, and colchicine treatment have been done in bahia grass [7–9]. However, studies in the field of molecular level have not been developed yet and still need more research.

Recently, some challenges using differential interference-contrast microscopy (DIC) technology have been conducted in all organs of plants. For example, in the meiotic chromosome [10], in petal development and ethylene biosynthesis [11], in nucleolus morphological changes [12], in pharmacology and cell biology [13], in xylem differentiation [14], in single microtubules [15]. In particular, near field DIC provides the ability to illuminate two neighboring points on the sample simultaneously, which shows that by modulating the two wavelengths employed in exciting such a probe, phase difference information can be retrieved through measuring the near field photoinduced force at the difference of the two modulation frequencies [16]. And more, two phases (cell structure and fluorescence) that appeared concurrently in the same sample and could be observed in *ASG-1* transgenic rice [17], and *Arabidopsis* (Chen et al. in contribution) while using the general DIC system. From the above description, it is understood that DIC shows a bright future for the clarification of not only the structures but also the mechanisms, and not only in plants but also in animals, as well as the microbes.

We choose bahia grass as a monocotyledons species as that would be particularly amenable to a molecular study of apomixis. It is shorter a plant and easily to cultivate among the important forage grasses. Recently, the somatic embryogenesis and plant regeneration system of bahia grass has been established in developing gene introduction techniques [18]. To clarify the molecular process controlling apomixis in *P. notatum*, it is important to determine the developmental timing and location of apomictic events in suitable laboratory strains that are currently available. It is a fact that the timing of apomictic gene expression, the key to cloning the apomixis genes has not been identified in bahia grass. Recently, it is reported in guinea grass (*Panicum maximum*) analyzed ultrastructurally and cytologically by DIC and Transmission electron microscopy (TEM) that, aposporous embryo sac initial cell (AIC) appearance is related with the increasing of ovary length [19–21]. And based on the ovary length as an index, AIC-specific clones have been obtained named as Apomixis-specific gene-1 (*ASG-1*) [22–24]. In the other species, molecular approaches to apomixis research have also been reported, i.e., *Citrus aurantium* [25], *Arabidopsis thaliana* [26], *Brachiaria brizantha* [27], *Tripsacum* [28], *Pennisetum* [29]. That bahia grass has or has not the same mechanisms should be understood for the molecular studies. In *P. notatum*, Quarin [8] reported the method to observe the effect of pollen source and pollen ploidy on endosperm formation and seed set in pseudogamous apomict. However, an efficient embryo sac analysis method cannot be found in bahia grass. Therefore, it is essential for the analysis of genetic and breeding in apomixis that the mechanism of embryo sac formation in apomict gets clear using an efficient analysis method [30].

In this study, the major objectives were, using the microscopy method of DIC I) to make it clear the cytological and quantitative observations of AIC appearance and its development in bahia grass, and to estimate the period of AIC appearance using ovary length as an index; and II) to clarify the process of polyembryonic seed set in facultatively apomictic ovules, and to provide information for estimation of the degree of apomixis or sexual of *P. notatum*. And the multiple embryo formation and the balance of maternal and parental to endosperm formation were also discussed.

2. The mechanism of AIC appearance and its development

2.1 The process of AIC appearance

Four apomictic bahia grass varieties and two obligate sexual varieties were chosen for this study. These materials were kindly provided from Osumi breeding branch, Kagoshima Prefecture Agricultural Experiment station, Japan. For the 2 obligate sexual materials, Nangoku and C 1, the former is a diploid ($2n = 20$) variety [31], and the latter is a diploid ($2n = 20$) trace. About four apomictic varieties, they are tetraploid [32].

One hundred to over 300 buds or flowers before and at anthesis were collected for each variety for embryo sac analysis. The buds and flowers were fixed in FPA50 (formalin propionic acid: 50% ethanol = 5: 5: 90) for 5–7 days at 4°C [20, 21, 33, 34]. Ovaries were picked out carefully from fixed buds or flowers under microscope by using needle and tweezers, placed in 70% ethanol followed dehydration series (70, 80, 90, 100% ethanol), and cleared in Herr's benzyl-benzoate-four-and-a-half fluid [35] for over 2 h at 0–4°C. The observations were conducted using DIC.

The frequencies of apospory and sexual were calculated at anthesis according to the schematic of **Figure 1** [36]. Here, apospory was classified into two types, *Panicum* type (PN) and *Paspalum* type (PS). PN type represents 4-nucleate embryo sac with one polar nucleus, one egg cell and two synergids [20, 37–39]. PS type represents 4- (or 5-) nucleate embryo sac with two polar nuclei, one egg cell and one (or two) synergid(s). Sexual means *Polygonum* type (S) 8-nucleate embryo sac with one egg cell, two polar nuclei, two synergids and three antipodals [40]. Therefore, the frequency of apospory in this study was estimated according to the total percentage of PN and PS types.

Until megasporogenesis there showed similar behaviors in both sexual and apospory varieties. After megasporogenesis, however, different events from sexual varieties were observed in apospory varieties. While the formed megaspore became almost unfunctional and degenerated with the membrane disappeared, AIC-derived from enlarged unreduced nucellar cells appeared from a different direction and usually entered the space around the degenerated or surviving megaspore (**Figure 2(1)**, [36]). In **Figure 2(2)** and (3), there showed coexistence of AIC and degenerated or surviving megaspore.

2.2 The process of AIC-derived aposporous embryo sac formation

In general, the AIC forms the embryo sac through a special process. The AIC undergoes mitosis two times and forms 2-, 4-nucleate. And no antipodal was found (**Figure 2(4)**). The cell division only occurred in the half-space of the embryo sac in the micropylar end. It is different from the sexual one which usually occupied the whole space of the sac. And then, the 4 nucleates developed to complete their parts in order (**Figure 2(5)**). In common, a mature embryo sac formed with one egg cell, one synergid and two polar nuclei (**Figure 2(6)**). In some rare cases, *Panicum* type 4-nucleate embryo sac with one polar nucleus was observed. In most ovules multiple apomictic embryo sacs were observed from one to six (**Figure 2(7)**). The distinctive features of mature embryo sacs were observed. 1) There is one egg cell, the nucleolus, ca 8 μm in diameter, being visible and surrounded with bright starch grains. With which sometimes the nucleus and its membrane could be distinguished, and the

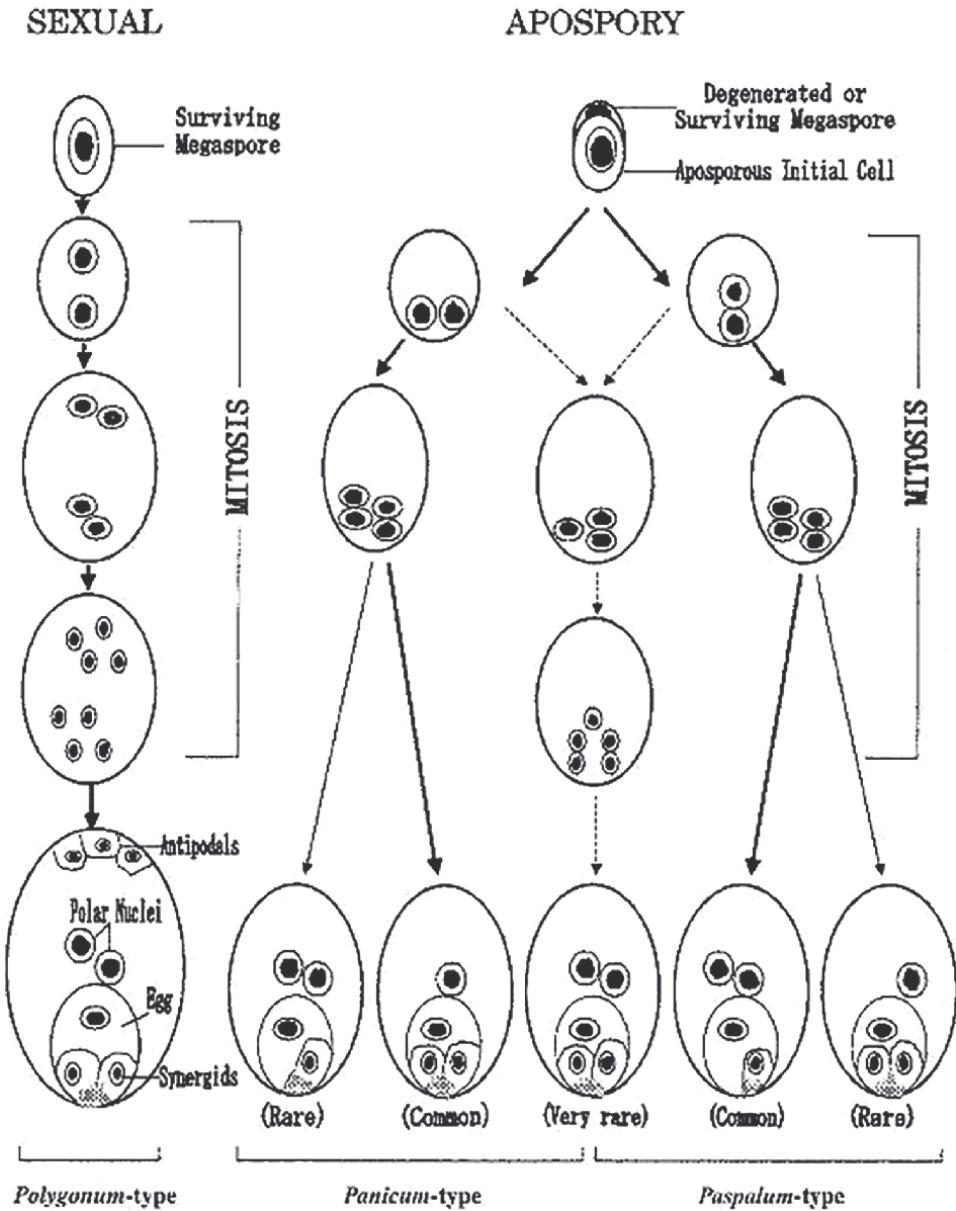


Figure 1.
Schematic representation of embryo sac development during sexual gametogenesis and the apospory forms in *P. maximum* and *P. notatum*.

cytoplasm was denser than the other cells. 2) In most of the embryo sacs, there is one synergid cell with the nucleolus, ca 4 μm in diameter, usually observed. And the cytoplasm was very few and the cell was occupied with bigger vacuoles. Moreover, near the synergid filiform apparatus usually were observable. 3) Two polar nuclei were almost observed with the nucleolus, ca 12 μm in diameter, surrounded by a nuclear membrane, and the cytoplasm was few; 4) No antipodal. The appearance of filiform apparatus is also evidence of embryo sac maturity in both of sexual and apomictic plants. The nucleoli are stained deeply with the clearing fluid, so that we can easily

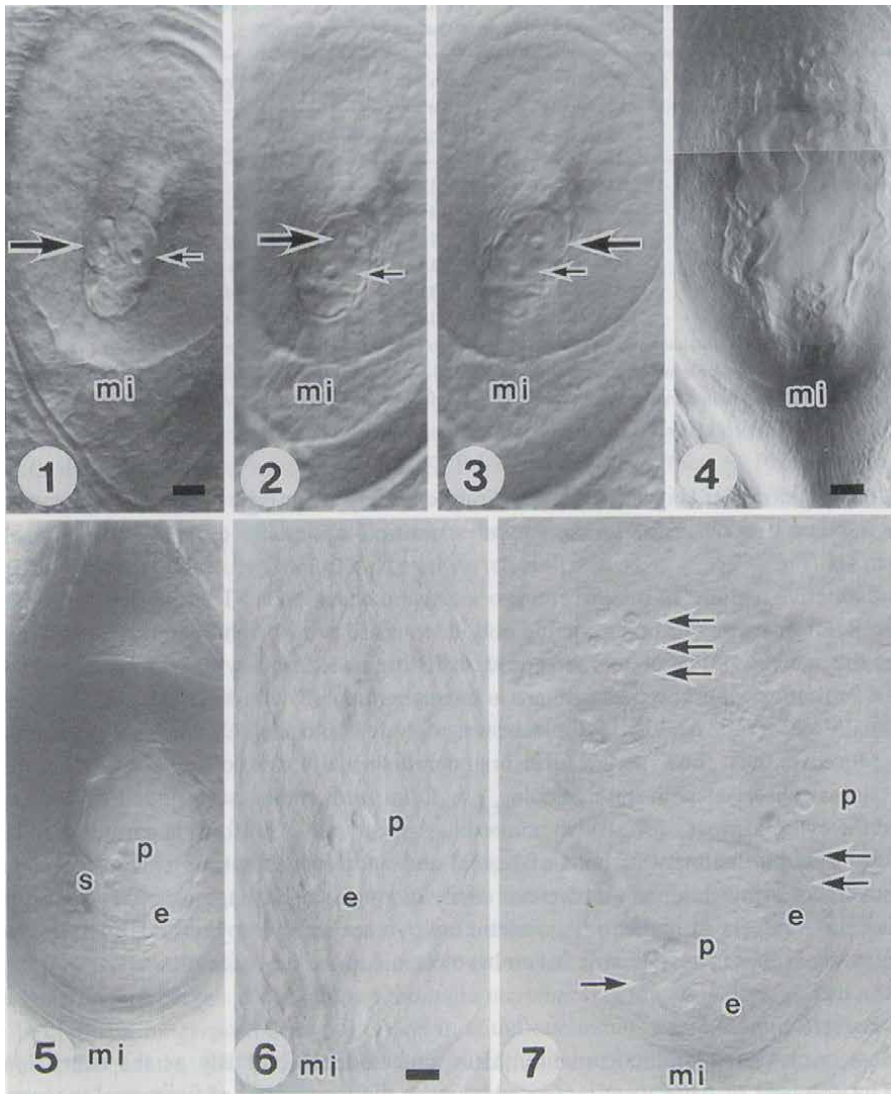


Figure 2. Aposporous embryo sac initial cell (AIC) appearance and AIC-derived embryo sac maturity in apomictic bahia grass (*P. notatum*). (1) AIC appearance (big arrow) and degenerating megaspore remained (small arrow). Big arrow indicates AIC derived from nucellar cells, with a pointed (sharp) cell wall inserting into the space where only one megaspore without nuclear membrane remaining. 2 and 3 are 2 focal planes of same specimen. (2) Megaspore degenerated (small arrow). (3) Functional AIC formation (big arrow) with a circular cell wall in chalazal end in one ovule. (4) Four-nucleate aposporous embryo sac formation after AIC underwent two times of division. The nucleates were gathered up from each other in the micropylar end. (5) Differentiation of four-nucleate nuclei, an egg cell firstly formed (e), one synergid cell (s) and two polar nuclei (p). (6) Aposporous embryo sac maturity with one egg cell (e), two nuclei (p) and one synergid cell (usually invisible) in micropylar end. (7) Polyembryonic ovule containing three aposporous embryo sacs marked with single, double and third arrows, respectively. e: egg cell; p: polar nucleus; s: synergid cell; mi: micropylar end. Bar = 30 μm in Fig. 2(1)–(3), Bar = 45 μm in Fig. 2(4) and (5), Bar = 25 μm in Fig. 2(6) and (7).

distinguish the stage of embryo sac formation by counting the numbers of nucleoli. Apomictic embryo sac in the micropylar end, matured about one day before anthesis, but in sexual varieties embryo sac did at the day of anthesis.

In most ovules of apomictic plants, AICs appeared continuously as the ovary length increased. The numbers of AICs were increased between the formations of functional megaspore and mature 4- or 8-nucleates according to the ovary length. For example, the ovary length in "competitor" was ca 520 μm when the first AIC appeared, and ca 496 μm when the third one did. However, 5 AICs appeared between 520 μm to 624 μm (688 μm) in ovary length. So were the other varieties. These values of ovary length indicated that AICs in the same ovule did not seem to differentiate synchronously.

From the length of ovaries, the stages of the ovary containing degenerated embryo sac were from 4-nucleate to their embryo sac maturity in apomictic plants, and from 4- and 8-nucleate to embryo sac maturity in sexual plants, respectively. On the other hand, the stage of functional megaspore showed a range of ovary length so wide it became very close to the value of degenerated ovaries.

2.3 The types of embryo sacs appeared in apomictic plants

Ten types of embryo sacs were observed and most of the embryo sacs belonged to PS type (Table 1, [36]). In apomicts, most ovules showed the number of embryo sacs more than one. And the ovules with different embryo sacs (5PS to 2PS, PS +PNn to 4PS +PNn, S, PNn) were observed. The percentage of S type (*Polygonum* type) was 13.6% (8/59), 9.1% (3/33), 12.9% (4/31) and 5.4% (2/37) in competitor, Nanou, Tifton and Common, respectively. PNn type (*Panicum* type) was only observed in one ovule among the tested varieties.

Among the 4 varieties, the frequencies of PN type were from 5.0% to 30.3%, and that of PS type were from 60.7% to 90.0%. Total frequencies of apospory were 86.4%, 91.1%, 87.1% and 95.0% in competitor, Nanou, Tifton and Common, respectively.

2.4 The general discussions concerning the appearance of AIC and AIC-derived embryo sac formation

There are no differences observed between obligate sexual and apomictic plants until megasporogenesis in bahia grass. After megasporogenesis, however, different events are followed in embryo sac formation. Sexual ovules proceeded in a manner typical of the Gramineae family, i.e., functional megaspores divided and formed a mature 8-nucleate embryo sac as reported in *P. notatum* [6] and in *P. maximum* [20, 40]. In contrast, megaspore does not divide in apomictic ovules and becomes degenerated (Figure 2(2) and (3)). Consequently, AIC (2n) derived from nucellus tissue, different from megaspore (n) appeared, divided, and directly formed mature 4-nucleate embryo sac. Most of the embryo sacs contain one egg cell, one synergid cell and two polar nuclei. It is different from that reported in *P. maximum*, i.e., one egg cell, two synergids and one polar nucleus [20, 38]. Here, it was called as *Paspalum* type of 4-nucleate embryo sac. Koltunow [2] indicated that in *Hieracium* MMC (mother megaspore cell) and AIC appeared together. It is different from *Paspalum* reported here and *Panicum* [20]. That means apospory has different reproductive process in different species, genus, or families. In this study, however, when megaspore developed normally, AIC appearance was not observed. By the way, after AIC appeared megaspore coexisted with AIC for a movement, and finally, degenerated. In any case, once AIC appeared, megaspore did not develop. This also differs from *Panicum* type reported by Chen and Kozono [20]. AICs appearance stage is distinctly different from sexual ones, and AIC occurs only in apomictic varieties. So, the stage

| Varieties | No. ovules observed | No. sterile ovules | Types of embryo sacs ¹ | | | | | | | | | | |
|------------|---------------------|--------------------|-----------------------------------|-----|-----|-----|---|--------|---------|---------|---------|-----|---|
| | | | 5PS | 4PS | 3PS | 2PS | S | PS+PNn | 2PS+PNn | 3PS+PNn | 4PS+PNn | PNn | |
| Competitor | 60 | 1 | 4 | 7 | 14 | 14 | 8 | 4 | 4 | 4 | 1 | 2 | 1 |
| Nanou | 35 | 2 | 1 | 2 | 7 | 11 | 3 | 3 | 3 | 2 | 1 | 3 | |
| Tifron | 44 | 14 | 2 | 1 | 4 | 13 | 4 | 2 | 2 | 2 | 1 | 1 | |
| Common | 43 | 6 | 3 | 5 | 10 | 13 | 2 | | | | 3 | 1 | |

¹PS: *Paspalum* type 4- (or 5-) nucleate with 2 polar nuclei, PN: *Panicum* type 4-nucleate with one polar nucleus, PNn: number of PN embryo sac (one or more PN), S: *Polygonum* 8-nucleate embryo sac.

Table 1.
 Number of ovules with different types of embryo sacs at anthesis in aponictic varieties of *P. notatum*.

could be considered as a stage related to apomixis gene expression. Here, we can set up a hypothesis that, AIC gene existed and usually waited for a chance to express, only when the megaspore gave out a signal not fulfilling its mission to form embryo sac. AIC appearance and the embryo sac formation also have an important evolution meaning to protect from any unforeseen happenings.

The earliest AIC that appeared in ovule always located in micropylar end, as the ovary grows, the later appeared are located along with the first AIC and being apart from it. To understand the mechanism of AIC appearance, we selected ovary length as an index and measured the ovaries when they were observed in different AIC appearance. From the range of ovary length, AICs do not appear together in same time. Instead, they seemed following a continuous course and appeared one by one during the period from megasporogenesis even to the first embryo sac maturity. According to the ovary length compared with the morphology of spikes, AICs appeared in the period of spike emerging to open at anthesis. With regard to the ovary length measured we could collect every stage of embryo sac to apply apomixis gene cloning. Sterile ovules with degenerated embryo sac appeared in both sexual and apomictic varieties based on the observation and quantitative analysis of ovary length. The ovary length of the ovary in which the first AIC appeared was longer than that of ovary the functional megaspore appeared in all varieties, indicating that the aposporous phenomenon of AIC appearance is initiated after megasporogenesis. Further, the ovary length of the ovary staged in functional megaspore was wide and close to the ovary lengths of the ovaries showing degeneration of megaspores in different developed stages. These results indicated indirectly that the development of sexual embryo sac derived from megaspore is often terminated accompanied by AIC appearance in many aposporous apomicts around the stage of megasporogenesis [41, 42]. Which one of megaspore or AIC firstly showed the signal to terminate or to appear will be interesting to further researches of apomixis. In the present study, 10 types of embryo sac formation were observed in *Paspalum notatum* (Table 1). Here we must issue that "S" types (sexual embryo sacs) observed were almost 4- or 5- nucleate embryo sacs. Except S type, the ovules with over 2S types contain only the same, 8-nucleate ones were not observed. For the case of ovules containing one, two or more 4-, 5- (8)-nucleate embryo sacs in one ovule, two pathways could be considered as follows. 1) The sexual embryo sac formation results from the direct division of one, two or over two megaspore(s) though the AIC(s) appeared (or not) in the same ovules. 2) They are derived from AIC(s). In particular, as the ovules with two megaspores in chalazal end were not observed in this study while AIC(s) appeared in the micropylar end, the former pathway could be hardly considered as a putative one. So, the later pathway seems reasonable based on that AICs develop into not only 4-nucleate [39] but also, at a low frequency, 5- nucleate embryo sacs in *Panicum* [38], or 8-nucleate ones in *Hieracium* [42]. In *Panicum*, the 4- nucleate embryo sac formation with an egg cell, one synergid and two nuclei, was reported by Bashaw and Hanna [37]. And 5- nucleate one with an egg cell, two synergies and two nuclei reported by Nakajima and Mochizuki [38]. For the mechanism of 5-nucleate embryo sac formation in *Panicum*, Chen and Kozono [20] set up a hypothesis. That is, after megaspore or AIC, whether which is located in micropylar end or not, divided firstly into two nuclei, only the micropylar nucleus continued to divide twice secondly and to form 4-nuclei, and in final, 5 nuclei formed totally in an embryo sac. For the distribution of the 5 nuclei, the chalazal nucleus derived from the first division of megaspore or AIC, and one of four micropylar nuclei derived from the second division of megaspore or AIC, pair with each other to form two polar nuclei, and for the remaining three nuclei, one becomes

one egg cell and two being synergies. From the above reports, we could conclude that facultatively apomictic bahia grass prefers to produce *Paspalum* type 4-(or 5-) nucleate (one egg cell, one (or two) synergid(s), and two polar nuclei) rather than to produce *Panicum* type 4-(or 5-) nucleate (one egg cell, two synergids, and one (or two) polar nucleus). Especially, there may be no *Polygonum* type (8-nucleate) embryo sac in polyembryonic ovules. Why did the two different apospory reproductive processes in the same 4-nucleate types of *Paspalum* and *Panicum* occur? This question means what should be clarified in the next future experiments.

3. The mechanism of polyembryonic seed set in facultatively apomictic ovules

3.1 The dominantly developmental process of the embryo sac formed in micropylar end by parthenogenesis

At 0 DAA, most of the embryo sac located in micropylar end became typical ones. In the accessions tested, the percentage of the typical embryo sacs in micropylar end was 90.9–100% higher than that in the other end (40.4–86.0%) (Table 2, [43]). If the typical one is S type, it consists of 8-nucleates of egg cell, 2 synergids and 3 antipodal. If the typical one is PN or PS type, it consists of 4-nucleates of egg cell, synergid and 2 polar nuclei.

At 6 h after anthesis, polar nuclei firstly started to divide to mean 9.0 cells in 55 of 59 ovules of Competitor. At 1 DAA, first division of egg cell was observed while the endosperm had reached mean 38.8 cells. This phenomenon is same to *P. maximum* that after the fertilization between the sperm and polar to form endosperm, with stimulation of the fertilization, the egg cell automatically divides into an embryo by parthenogenesis [20, 21]. Here, the endosperm always appeared as free-nuclear endosperm during 0–2 DAA. From 1 to 4 DAA, the mean numbers of egg embryo and endosperm cells were increased ca. 4 times per day, respectively. The number of ovules containing developed egg embryo and endosperm were increased as the days after anthesis increased. However, the ovules unfertilized remained in a certain number showed in Table 2. At 2–4 DAA, formation of endosperm cell wall started from the position farthest and nearest to the embryo, respectively. At 4 DAA, egg cell has undergone 6 cycles of division and became an embryo containing mean >64 cells. The endosperm was well-developed and almost occupied the whole space of the sac where it is in. After 4 DAA, the endosperm and young embryo developed so fast that the numbers of both cells could not be counted under the microscope. On the other

| Varieties | No. ovules observed (A) | No. embryo sacs (B) | Mean no. (B/A) | No. embryo sacs | |
|------------|-------------------------|---------------------|----------------|-----------------|-------------|
| | | | | Micropylar | Others |
| Competidor | 59 | 171 | 2.9 | 59 (100%) | 112 (78.6%) |
| Nanou | 33 | 85 | 2.6 | 30 (90.9%) | 52 (40.4%) |
| Tifton | 31 | 51 | 1.6 | 31 (96.8%) | 20 (80.0%) |
| Common | 40 | 90 | 2.3 | 40 (92.5%) | 50 (86.0%) |

Table 2. Distribution of matured embryo sacs at anthesis in facultatively apomictic varieties of *P. notatum*.

hand, during 1–4 DAA, nucellar cells were changed to be vacuolated, as endosperm cells changed from free-nuclear to cell-wall-formed with well-developed cytoplasm. No morphological differences were observed between the developed sacs either derived from sexual sac or apomictic sac.

In polyembryonic ovules, the embryo sac in micropylar end developed dominantly when compared with that in the other ends. **Figure 3** showed the developments of

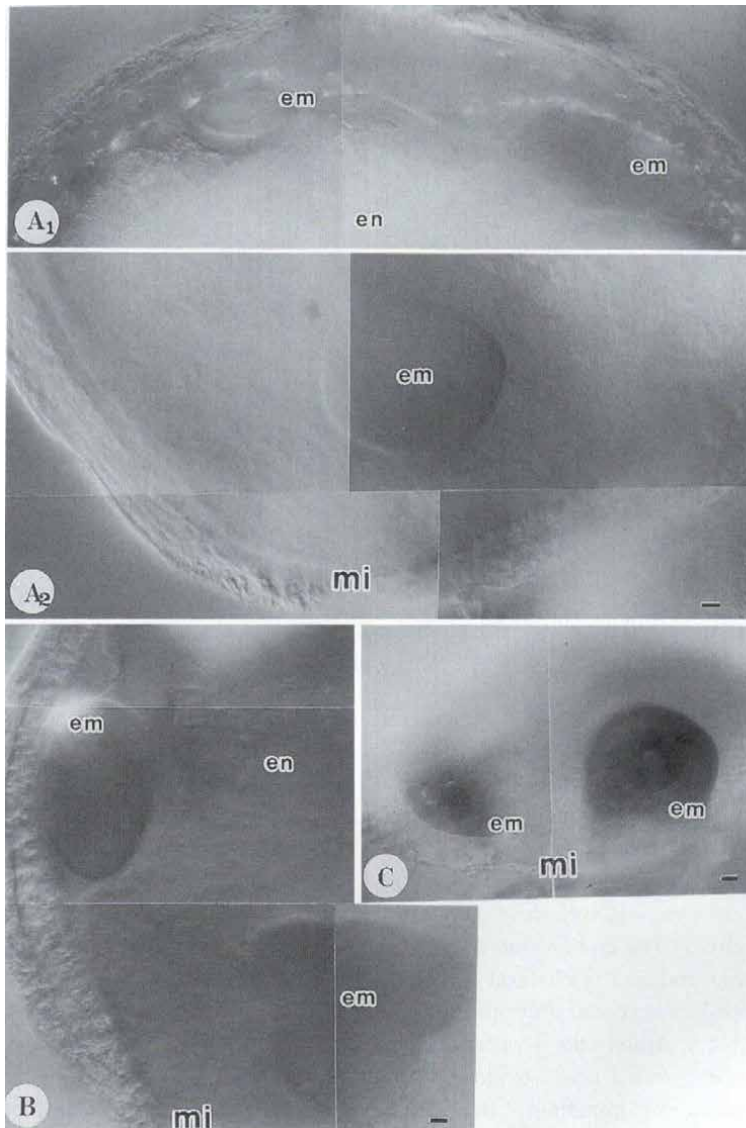


Figure 3. Multiple embryo formation in the same embryo sac in *P. notatum* flowers at 7–10 d after anthesis (DAA). A1. Two embryos with well-developed endosperm appeared in the chalazal end. A2. A globular-stage embryo around by endosperm in micropylar end at 7 DAA. (A1 and A2 are the same specimen). B) One embryo around by endosperm in micropylar end and one embryo in the side of ovule tissue were observed at 8 DAA. C) Two embryos side by side are located in the micropylar end. e = egg cell, p = polar cells, s = synergid, em = embryo, en = endosperm, mi = micropylar end. Bar = 45 μ m.

| Varieties | No. ovules observed A | No. embryo sacs B | ES in micropylar end | | | ES in the other end | | |
|------------|-----------------------|-------------------|-----------------------------|-------------|----------------|-----------------------------|--------------------|----------------|
| | | | embryo and endosperm C(C/A) | embryo only | endosperm only | embryo and endosperm D(D/A) | embryo only E(E/B) | endosperm only |
| Competitor | 30 | 41 | 26 (87%) | 0 | 4 | 0 (0%) | 7 (17%) | 0 |
| Nanou | 27 | 28 | 15 (56%) | 1 | 0 | 0 (0%) | 1 (4%) | 0 |
| Tifton | 30 | 35 | 21 (66%) | 0 | 2 | 0 (0%) | 3 (9%) | 0 |
| Common | 30 | 38 | 23 (77%) | 0 | 0 | 1 (3%) | 5 (13%) | 0 |

Table 3. Development of embryo sac (ES) in the flowers 4 d after anthesis in facultatively apomictic varieties of *P. notatum*.

both embryo and endosperm of the sac in micropylar end, and the other sacs were crowded out to chalazal end, with dividing egg embryo and polar nuclei [36].

The ovules containing dominantly developed embryo sacs were investigated at 4 DAA in 4 varieties. The results showed in **Table 3** indicated that, 56–87% of the ovules contained developed sacs in micropylar end in all the accessions, and in contrast, on other ends, 0% in 3 varieties and 3% in one variety.

3.2 The developmental process of other types of embryo sacs formed in chalazal end

Some other cases appeared different from the above. 1) A single embryo sac in micropylar end contains a well-developed embryo and unfertilized 2 nuclei. 2) A single embryo sac contains 2 embryos and well-developed endosperm. 3) The embryo sac degenerated in micropylar end, and in chalazal end, the sac with developed embryo and unfertilized 2 nuclei. And the data of other types could be known from **Table 3**. Among the 4 varieties, the number of the embryo sac in micropylar end containing only embryo was 1 of 27 ovules in Nanou, and the numbers containing only endosperm were 4 of 30 ovules in Competitor, 2 of 30 ovules in Tifton, respectively. In contrast, in the other end, the numbers of the sacs containing only embryo were 4–17% in all the varieties, and the number containing only endosperm was 0% in the varieties.

3.3 The mechanism of seed forming embryo development in polyembryonic embryo sacs

At 6 DAA, the developed embryo and endosperm of the sac in micropylar end occupied the embryo sac it located in, and at the same time, the space of the whole ovules was almost occupied by the developed sac (**Figure 3a**). The embryo usually exists with near globular shape, and it is surrounded by well-developed endosperm. For the embryo sacs in the other ends, they usually were squeezed out to outside of the developed sac. However, those sacs showed continuous development. Some egg cells divided well, and formed embryos usually located in opposite side to micropylar end (**Figure 3a**), or the neighbor (**Figure 3b** and **c**). At 10 DAA, the formed 2 embryos showed the same morphology (**Figure 3c**), and it is difficult to distinguish their origins between them. From **Table 3** [36], we can find that about 4–17% of ovules observed contain two or more embryos in the same ovule.

In emasculated ovules observed at 4 DAA, no developed embryo sac distinguished in 60 ovules of 4 varieties. The parthenogenesis rate was 0% in all the 4 varieties. At 15 DAA, the inflorescences that were emasculated and then isolated from any pollen source failed to produce seed. So, pseudogamous is essential for seed set in *P. notatum*.

3.4 The general discussion concerning the dominant development of the sac in micropylar end and seed formation by parthenogenesis

In facultative apomictic bahia grass, AICs appeared one by one, and then, they became multiple embryo sacs in same ovule, as the ovary length increased [36]. And as the first AIC usually appeared and located in the micropylar end, 92.5 to 100% of embryo sacs closest to micropylar end of ovule matured at anthesis observed in this study (**Table 2**). On the other hand, the embryo sacs located in other end showed 40.4 to 86.0% mature rates at anthesis. The AIC appearance age (order) maybe influence

the mature of apomictic embryo sacs themselves. It could be considered that the first appeared AIC in micropylar end has the temporal dominant in formation and maturity of the embryo sac when compared with the other sacs. And for the fertilization chance, the sac has also the positional dominant, as it was closest to synergid cell through which pollen tube penetrates and finishes fertilization. Therefore, the sac derived from first AIC located in micropylar end has the advantage of fertilization. On the observations of ovules at 4 DAA, the rates of developed embryo sacs with embryo and endosperm were from 56 to 87% in the sacs of micropylar end (**Table 3**). On the other hand, the other sacs were 0% in 3 varieties, and one variety was 3%. Therefore, the sac in micropylar end has the advantage of seed set. This result also supported the hypothesis that the embryo of developed sac in micropylar end, in final, became a seed-forming embryo [20]. Using this method, we can estimate the degree of apomixis or sexual of any facultative apomictic materials used, based on the analysis of embryo sacs in micropylar end at anthesis.

Different events were observed on the seed set between guinea grass and bahia grass. In guinea grass, the other embryo sacs were crowded out to the chalazal end by the developed micropylar sac, and in final, they were completely degenerated after 10 DAA [21]. In contrast, the rates of embryos formed in the other embryo sacs were 4–17% in 4 accessions of bahia grass used in this study. These are higher than that (0%) in 5 accessions and that (2%) in one accession of guinea grass [21]. This evident was also observed from embryo sac analysis (**Figure 3**). As the sac derived from AIC contains $2n$ level reproductive cells, egg cell does not need fertilization. However, for the endosperm formation, fertilization between central cell and sperm cell is needed. And egg cell usually starts division followed the endosperm cell formation. The other sacs also follow the same manner. As the embryo sac developed advantageously in micropylar end, it could be considered that the egg cells in the other sacs were developed vigorously in different places of ovules. In that case, only embryo formed but no endosperm. In the polyembryonic ovules, the embryos located in the other sacs usually presented close to the well-developed endosperm of the micropylar sac. The 2 kinds of embryos in the same ovule seemed sharing the endosperm of the micropylar sac. Maybe that is why the embryos in different embryo sacs could coexist in the same ovule. At the germination experiment, twines, or multiple seedlings (>5%) were observed (data not shown). This means the different embryos have the same germination capacity. For the endosperm balance number, some reporters have discussed the requirement for balance between maternal and paternal contributions to the endosperm formation [44–48]. When they used different ploidies and sexual materials, endosperm balance in terms of maternal to paternal ratio, 2:1 was considered balanced and should produce normal endosperm. And they indicated that unreduced embryo sacs with one central-cell nucleus (4 factors), when fertilized by a sperm (2 factors), would result in the proper endosperm ratio of $2m:1p$, and the closed percentages were obtained between embryo sacs with a single central-cell nucleus and ovaries with endosperm developing 6 and 8 d after pollination. The result of aposporous guinea grass reported by Chen and Kozono [21] also supported the above explanation. In grasses, the most common type of unreduced embryo sac is the 4-nucleates *Panicum* type (PN) developing into one egg, two synergids, and one polar nucleus or, more rarely, one egg, one synergid, and two polar nuclei [2, 42]. In *Paspalum notatum*, Chen et al. [36] reported that the percentages of unreduced embryo sacs with 2 central-cell nuclei (PS) were 60.7–90.0%, and that with one central cell nucleus (PN) were 5.0–30.3% in 4 varieties observed, respectively. However, the percentages of ovaries with endosperm developing 4 DAA

were 56–87% in the same 4 varieties in this study. If we follow the report of Morgan et al. [47], only 5.0–30.3% of developed endosperm should be obtained. Recently, Quarin [8] reported the related information about the endosperm balance number that, apomictic 4x *P. notatum* is a pseudogamous species with effective fertilization of the 2 unreduced ($2n = 4x$) polar nuclei by a reduced ($n = 1x$) sperm. In that case, endosperm development and seed set occurred independently in the species. In that case, endosperm development and seed set occurred independently of the species or the ploidy level of the pollen donor. In his explanation, as sexual *Paspalum* plants fit the endosperm balance number (EBN), the EBN insensitivity is observed in apomictic apomixis. The EBN insensitivity could have arisen as an imprinting consequence of a high maternal contribution.

Recently, the mechanisms of reproductive characterization [49], molecular and genetic regulation [50–52], and its utilization [53, 54] have been discovered consequently in *P. notatum*. Together with the clarification of the mechanisms of aposporous embryo sac initial cell appearance and the cell-derived aposporous embryo sac formation described, here, in *P. notatum* and previous and similar report in *P. maximum* [19], this study will provide the essential and important information for successful cloning of apospory genes in *P. notatum*. And therefore, the *P. notatum* as one of the main players will be chosen in apomixis research and give another extension for the breeding program and productive utilization in agriculture and forage grasses.

4. Conclusion

In this study, using the plant materials of several apomictic and obligately sexual varieties of bahia grass (*Paspalum notatum*) and the method of differential interference-contrast microscopy (DIC), we have clarified the mechanisms of aposporous embryo sac initial cell (AIC) appearance, the numbers of AICs increased as the ovary length grew before anthesis and AIC-derived apomictic embryo sac formation at anthesis, and after the anthesis, the process of polyembryonic seed formation by parthenogenesis. With the DIC technique giving the 3-D image recognition, AIC appearance, a different event from obligate sexual one, was firstly observed and recognized in *P. notatum*, so it could be expected as a related candidate with apomixis gene expression, as the *ASG-1*, an apomixis-specific gene-1 as reported in *P. maximum* based on the ovary length as an index to sample the AIC stage ovaries according to DIC observations [22, 24]. Therefore, the results of this study will be useful to provide the information on isolation of apomixis gene from apomictic varieties and the production of gene transgenic plants [17].

Acknowledgements

This study was partly supported by the Grant-in-Aid for Scientific Research (C) of the Ministry of Education, Culture, Science and Sports of Japan, No. 10660010.

Conflict of interest

Authors have declared that no competing interests exist.

Author details


Lanzhuang Chen^{1*} and Liming Guan²

1 Faculty of Environmental and Horticultural Science, Minami Kyushu University, Miyakonojo, Miyazaki, Japan

2 Faculty of Education, Miyazaki University, Miyazaki, Japan

*Address all correspondence to: lzchen@nankyudai.ac.jp

IntechOpen

© 2022 The Author(s). Licensee IntechOpen. This chapter is distributed under the terms of the Creative Commons Attribution License (<http://creativecommons.org/licenses/by/3.0>), which permits unrestricted use, distribution, and reproduction in any medium, provided the original work is properly cited. 

References

- [1] Hanna WW, Bashaw EC. Apomixis: Its identification and use in plant breeding. *Crop Science*. 1987;27:1136-1139
- [2] Koltunow AM. Apomixis: Embryo sacs and embryos formed without meiosis or fertilization in ovules. *Plant Cell*. 1993;5:1425-1437
- [3] Burson BL, Bennett HW. Cytology, method of reproduction and fertility of Brunswick grass, *Paspalum nicorae* Parodi. *Crop Science*. 1970;10:184-187
- [4] Burton GW. The method of reproduction in common bahia grass, *Paspalum notatum*. *Journal of American Society of Agronomy*. 1948a;40:443-452
- [5] Burton GW. Method for producing chance crosses and polycrosses of *Pensacola* bahia grass, *Paspalum notatum*. *Journal of American Society of Agronomy*. 1948b;40:469-472
- [6] Burton GW, Forbes I. The genetics and manipulation of obligate apomixis in common bahia grass (*Paspalum notatum* Flugge). *Proceeding of the Eighth International Grassland Congress*. Great Britain. 1960. pp. 66-71
- [7] Norrmann GA, Quarin CL, Burson BL. Cytogenetics and reproductive behavior of different chromosome races in six *Paspalum* species. *The Journal of Heredity*. 1989;80:24-28
- [8] Quarin CL. Effect of pollen source and pollen ploidy on endosperm formation and seed set in pseudogamous apomictic *Paspalum notatum*. *Sexual Plant Reproduction*. 1999;11:331-335
- [9] Quarin CL, Burson BL, Burton GW. Cytology of intra- and interspecific hybrids between two cytotypes of *Paspalum notatum* and *P. cromyorrhizon*. *Botanical Gazette*. 1984;145:420-426
- [10] Yang F, Fernández-Jiménez N, Tučková M, Vrána J, Cápál P, Díaz M, et al. Defects in meiotic chromosome segregation lead to unreduced male gametes in Arabidopsis SMC5/6 complex mutants. *The Plant Cell*. 2021;33(9):3104-3119
- [11] Sam WE, Silveira SR, Diego I, Roche DI, Andrea Bimbo A, Martinelli AP, et al. Novel functions of the Arabidopsis transcription factor *TCP5* in petal development and ethylene biosynthesis. *The Plant Journal*. 2018;94(5):867-879
- [12] Hayashi K, Matsunaga S. Heat and chilling stress induce nucleolus morphological changes. A comparative study on the use of microscopy in pharmacology and cell biology research. *Journal of Plant Research*. 2019;132:395-403
- [13] Reigoto AM, Andrade SA, Seixas MCRR, Costa ML, Mermelstein C. A comparative study on the use of microscopy in pharmacology and cell biology research. *PLoS One*. 2021;22:e0245795. DOI: 10.1371/journal.pone.0245795
- [14] Yoshimoto K, Takamura H, Kadota I, Motose H, Takahashi T. Chemical control of xylem differentiation by thermosensitive auxin. *Scientific Reports*. 2016;6:21487
- [15] Mahamdeh M, Simmert S, Luchniak A, Schäffer E, Howard J. Label-free high-speed wide-field imaging of single microtubules using interference reflection microscopy. *Journal of Microscopy*. 2018;272(1):60-66

- [16] Heydarian H, Yazdanfar P, Zarif A, Rashidian B. Near field differential interference contrast microscopy. *Scientific Reports*. 2020;**10**:9644
- [17] Chen LZ, Guan LM, Toyomoto D, Sugita T, Hamaguchi T, Okabe R. Plant regeneration and its functional analysis within transgenic rice of *ASG-1*, an apomixis-specific gene isolated from apomictic guinea grass. *Biotechnology Journal of International*. 2016;**16**(3):1-13
- [18] Shatters RG, Wheeler RA, West SH. Somatic embryogenesis and plant regeneration from callus cultures of 'Tifton 9' bahia grass. *Crop Science*. 1994;**34**:1378-1384
- [19] Chen LZ, Guan LM. Ultrastructural mechanisms of aposporous embryo sac initial cell appearance and its developmental process in gametophytic apomicts of Guinea grass (*Panicum maximum*). In: Maaz K, editor. *The Transmission Electron Microscope*. Rijeka: InTech; 2012. DOI: 10.5772/34912
- [20] Chen LZ, Kozono T. Cytology and quantitative analysis of aposporous embryo sac development in guinea grass (*Panicum maximum* Jacq.). *Cytologia*. 1994a;**59**:253-260
- [21] Chen LZ, Kozono T. Cytological evidence of seed-forming embryo development in polyembryonic ovules of facultatively apomictic guinea grass (*Panicum maximum* Jacq.). *Cytologia*. 1994b;**59**:351-359
- [22] Chen LZ, Guan LM, Sio M, Hoffmann F, Adachi T. Developmental expression of *ASG-1* during gametogenesis in apomictic guinea grass (*Panicum maximum*). *Journal of Plant Physiology*. 2005;**162**:1141-1148
- [23] Chen LZ, Guan LM, Miyazaki C, Kojima A, Saito A, Adachi T. Cloning and characterization of a cDNA expressed at aposporous embryo sac initial cell appearance stage in guinea grass (*Panicum maximum* Jacq.). *Apomixis Newsletter*. 1999a;**11**:32-34
- [24] Chen LZ, Miyazaki C, Kojima A, Saito A, Adachi T. Isolation and characterization of a gene expressed during early embryo sac development in apomictic guinea grass (*Panicum maximum*). *Journal of Plant Physiology*. 1999b;**154**:55-62
- [25] Carimi F, Pasquale FD, Puglia AM. In vitro rescue of zygotic embryos of sour orange, *Citrus aurantium* L., and their detection based on RFLP analysis. *Plant Breeding*. 1998;**117**:261-266
- [26] Chaudhury AM, Ming L, Miller C, Craig S, Dennis E, Peacock J. Fertilization-independent seed development in *Arabidopsis thaliana*. *Proceedings of the National Academy of Science USA*. 1997;**94**:4223-4228
- [27] Leblanc O, Armstead I, Pessino S, Ortiz JPA, Evens C, Valle CD, et al. Non-radioactive mRNA fingerprinting to visualize gene expression in nature ovaries of *Brachiaria* hybrids derived from *B. brizantha*, an apomictic tropical forage. *Plant Science*. 1997;**126**:49-58
- [28] Leblanc O, Grimaneli D, Gonzalez-de-Leon D, Savidan Y. Detection of the apomictic mode of reproduction in maize *Tripsacum* hybrids using maize RFLP markers. *Theoretical and Applied Genetics*. 1995;**90**:1198-1203
- [29] Lubbers EL, Arthur L, Hanna WW, Ozias-Akins P. Molecular markers shared by diverse apomictic *Pennisetum* species. *Theoretical and Applied Genetics*. 1994;**89**:636-642
- [30] Savidan Y. Apomixis: Genetics and Breeding. In: Janick J, editor.

Plant Breeding Reviews. London: John Wiley & Sons, Inc; 2000. pp. 13-86

[31] Houman M, Tsurumi Y, Mochidome N, Tsuyushige M, Hayasaki T, Tsushima Y, et al. Breeding a new bahia grass variety “Nangoku” (In Japanese). In: Kagoshima Prefect. Agri. Exper. Stan. Report. 1984. pp. 13-24

[32] Komatsu T, Yamakata M, Hakuzan R, Doi O, Ueno K, Nagatani T, et al. A new variety ‘an-ou’ Bahiagrass (*Paspalum notatum* Flugge). Kyushu Agricultural Research. 1991. p. 159

[33] Kojima A, Nagato Y. Diplosporous embryo-sac formation and the degree of diplospory in *Allium tuberosum*. Sexual Plant Reproduction. 1992;5:72-78

[34] Kojima A, Nagato Y. Discovery of highly apomictic and highly amphimictic dihaploids in *Allium tuberosum*. Sexual Plant Reproduction. 1997;10:8-12

[35] Herr JM Jr. An analysis of methods for permanently mounting ovules cleared in four-and-a-half type clearing fluids. Stain Technology. 1982;57:161-169

[36] Chen LZ, Guan LM, Kojima A, Adachi T. The mechanisms of appearance of aposporous initial cell and apomictic embryo sac formation in *Paspalum notatum*. Cytologia. 2000;65:333-341

[37] Bashaw EC, Hanna WW. Apomixis reproduction. In: Chapman GP, editor. Reproductive Versatility in the Grasses. Cambridge: Cambridge University Press; 1990. pp. 100-130

[38] Nakajima K, Mochizuki N. Degrees of sexuality in sexual plants of guinea grass by the simplified embryo sac analysis. Japanese Journal of Breeding. 1983;33:45-54

[39] Warmke HE. Apomixis in *Panicum maximum*. American Journal of Botany. 1954;41:5-11

[40] Hanna WW, Powell JB, Millot JC, Burton GW. Cytology of obligate sexual plants in *Panicum maximum* Jacq and their use in controlled hybrids. Crop Science. 1973;13:695-697

[41] Asker SE, Jerling L. Apomixis in Plants. Boca Raton: CRC Press; 1992

[42] Nogler GA. Gametophytic Apomixis. In: Johri BM, editor. Embryology of Angiosperm. New York: Springer-Verlag; 1984. pp. 475-518

[43] Chen LZ, Guan LM, Kojima A, Adachi T. The mechanisms of polyembryonic seed set in *Paspalum notatum*. Cytologia. 2001;66:157-165

[44] Brink RA, Cooper DC. The endosperm in seed development. The Botanical Review. 1947;13:423-477

[45] Haig D, Westoby M. Genomic imprinting in endosperm: Its effect on seed development in crosses between species, and between different ploidy levels of the same species, and its implications for the evolution of apomixis. Philosophical Transactions of the Royal Society of London B. 1991;333:1-13

[46] Johnston SA, Den Nijs TPM, Peloquin SJ, Hanneman RE. The significance of genic balance to endosperm development in interspecific crosses. Theoretical and Applied Genetics. 1980;57:5-9

[47] Morgan RN, Ozias-Akins P, Hanna WW. Seed set in an apomictic BC3 pearl millet. International Journal of Plant Sciences. 1998;159:89-97

[48] Nishiyama T, Yabuno T. Triple fusion of the primary endosperm nucleus as a

cause of interspecific incompatibility in Avena. Euphytica. 1979;28:57-65

[49] Ortiz JPA, Quarin CL, Pessino SC, Acuña CA, Martínez EJ, Espinoza F, et al. Harnessing apomictic reproduction in grasses: What we have learned from *Paspalum*. Annals of Botany. 2013;112(5):767-768

[50] AcuñaCA, BlountAR, QuesenberryKH, Hanna WW, Kenworthy KE. Reproductive characterization of Bahiagrass Germplasm. Crop Science. 2007;47:1711-1717

[51] Felitti SA, Acuña CA, Ortiz JPA, Quarin CL. Transcriptome analysis of seed development in apomictic *Paspalum notatum*. The Annals of Applied Biology. 2015;167:36-54. DOI: 10.1111/aab.12206

[52] Pozzi FI, Pratta GR, Acuña CA, Felitti SA. Xenia in bahiagrass: Gene expression at initial seed formation. Seed Science Research. 2018;29:29-37

[53] Kaushal P, Dwivedi KK, Radhakrishna A, Srivastava MK, Kumar V, Roy AK, et al. Partitioning apomixis components to understand and utilize gametophytic apomixis. Frontiers in Plant Science. 2019;10:256. DOI: 10.3389/fpls.2019.00256

[54] Pupilli F, Barcaccia G. Cloning plants by seeds: Inheritance models and candidate genes to increase fundamental knowledge for engineering apomixis in sexual crops. Journal of Biotechnology. 2012;159:291-311

Analysis of Osteoporosis by Electron Microscopy

Neng Nenden Mulyaningsih and Rum Sapundani

Abstract

Osteoporosis is a skeletal disorder characterized by decreased bone strength which affects the increased risk of fracture. Emerging evidence discovered that osteoporosis is associated with reduced bone density and bone quality. Therefore, analysis of bone morphology can afford insight into the characteristics and processes of osteoporosis. Electron microscopy, one of the best methods, can directly provide ultrastructure evidence for bone morphology. Here, we describe an experimental procedure for electron microscopy preparation and analysis of the resulting images, especially scanning and transmission electron microscopes, to analyze bone morphology in animal models of rats. Compared to other bone analyzers such as atomic absorption spectrophotometer, ultraviolet–visible spectroscopy, Fourier transform infrared spectroscopy, Raman spectroscopy, and X-ray diffraction, scanning and transmission electron microscopes are still important to strengthen visual analysis, and a better understanding of this method could be significant to examine bone morphology.

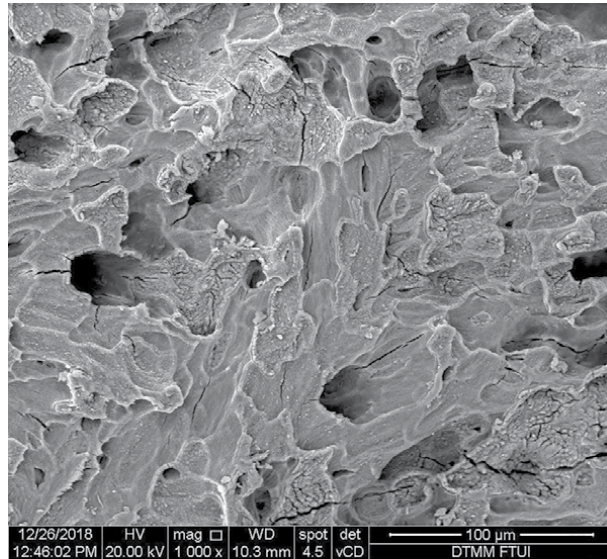
Keywords: osteoporosis, bone strength, fractures, electron microscopy, bone morphology

1. Introduction

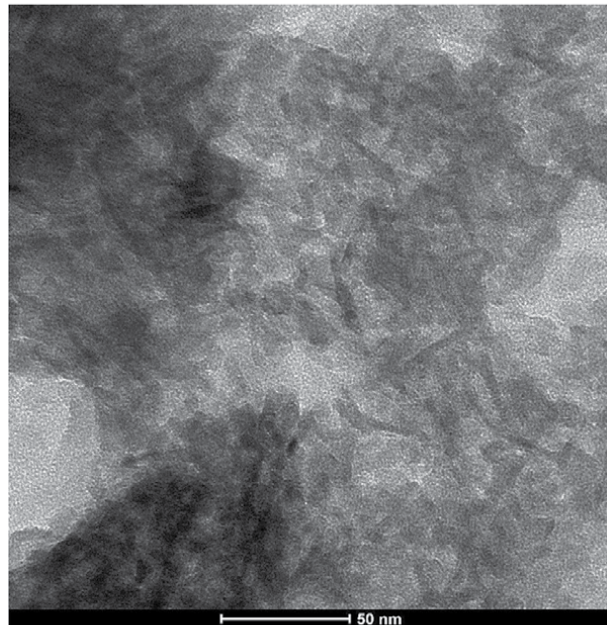
Osteoporosis is a metabolic disorder causing bone mineral density to decrease and changing the bone structure [1]. It is a degenerative disease whose initial symptoms are not known with certainty. Someone who suffers from osteoporosis will usually experience complaints if the stage is severe [2, 3]. Bones with osteoporosis will experience a decrease in mechanical strength so they are prone to fracture, and will easily crack or become brittle if exposed to a hard object. It is characterized by low bone mass and structural breakdown of bone tissue. Some parts of the body that are at risk for osteoporosis include the spine, pelvis, femur, tibia, pelvic bones, wrist bones, and other bone parts dominated by the trabecular bone [4–6].

Osteoporosis can be diagnosed clinically using bone mineral density measurements. At present, bone densitometry is the standard method for diagnosis and treatment monitoring. However, it still possesses significant drawbacks because it cannot give information about the structural manifestations of the disease. Frequently, bone mineral density is analyzed using x-ray or ultrasound imaging methods. In x-ray imaging such as dual-energy x-ray absorptiometry (DEXA) and quantitative computer tomography (QCT), the intensity of the image is correlated to the mineral density of

the tissue. In ultrasound, the intensity of the image reflects changes in the frequency and amplitude of sound waves traveling through tissue. X-ray procedures employ ionizing radiation, which can have a damaging impact in sufficient doses. Ultrasound, although harmless, offers only a small field of view, which can restrict measurement accuracy. In addition to bone density, bone quality which includes bone microarchitecture is also a concern. Recent developments in imaging, especially electron microscopy,



(a)



(b)

Figure 1.
(a) Image of SEM scans, and (b) image of TEM scans on femoral bones of rats from the osteoporosis group.

can now give detailed information about the effects of architecture on disease progression and regression in response to treatment. However, before the diagnosis is made, of course, it is necessary to study and research in a sample or biological material to determine the process of bone remodeling and osteoporosis. The samples analyzed generally use rats as animal models. It takes a long time to make rats osteoporosis naturally. Therefore, rats were given treatment to condition the occurrence of osteoporosis. Some of the common actions taken to condition osteoporosis rats are by giving them a calcium-deficient diet or by performing ovariectomy on these rats [7–10].

Several characterization tools that can be used to analyze mouse bones include X-ray Diffraction (XRD), Fourier Transform Infrared Spectroscopy (FTIR), Ultraviolet (UV)-visible Spectroscopy, or Atomic Absorption Spectroscopy (AAS). However, these tools provide information in the form of numbers or graphs. A promising imaging modality for morphological analysis of both cortical and trabecular bone is electron microscopy. The types of electron microscopes commonly used to analyze bone morphology are Scanning Electron Microscope (SEM) and Transmission Electron Microscope (TEM). **Figure 1** illustrates the different imaging modalities, between SEM and TEM, which were used to analyze the morphology of the rat femur bone.

This review focuses on the emerging methodology of quantitative electron microscopy to assess the bone structure and morphology of osteoporotic rats. For more than 10 years, numerous approaches have been investigated to obtain quantitative image-based information on bone architecture, both trabecular bone, and cortical bone. An indirect method that does not require resolution at individual trabecular scales and can therefore be performed at any skeletal location, a recoverable component of the degree of total transverse relaxation. Therefore, electron microscopy-based structure analysis is technically demanding in terms of the required image acquisition. Other requirements that must be fulfilled involve motion correction and image registration, both of which are important to achieve the reproducibility required in repeated studies. The main targeted clinical application involves the prediction of fracture risk in femoral rats conditioned by osteoporosis due to ovariectomy.

2. Electron microscopy basics

An electron microscope is a type of microscope in which the illumination source is an electron beam. Illumination itself is a process of light coming to an object. There are electron microscopes that have high image resolution, even magnifying objects on the nanometer scale, which are produced by the controlled use of electrons in a vacuum captured on a fluorescent screen. The first electron microscope was introduced by an engineer and professor from German, Ernst Ruska (1906-1988), in 1931, and the same principles behind his prototype still dominate modern Ems [11, 12].

2.1 Principle

Electron microscopy uses signals generated by the interaction of the electron beam with the sample to gain information about its structure, morphology, and composition. The process and major parts of an electron microscope are:

1. Electrons are produced by the electron gun
2. The electron beam is concentrated on the sample by condenser lenses.

3. About 100 kV – 1000 kV accelerating voltage is employed between the tungsten filament and anode to move electrons down the column.
4. The sample to be observed should be fabricated very thin, or minimal 200 times thinner than that observed in optical microscopes. A very thin sample with a size of 20-100 nm was sliced and put in the sample holder.
5. The electronic beam traverses the sample and electrons are scattered relying on the thickness or refractive index of different areas of the sample.
6. The denser sample areas will scatter more electrons so that the image displayed in these areas will be darker because fewer electrons hit this area of the screen. Contrarily, the transparent areas will look brighter.
7. The electron beam leaving the sample is transferred to the objective lens which will make a magnified image.
8. The eyepiece then renders the final image for further magnification.

2.2 Types of electron microscope

Electron microscopes are categorized into three types based on operating styles:

2.2.1 Scanning electron microscope (SEM)

Nowadays, scanning electron microscopy (SEM) is a robust and effective imaging instrument. It is employed for scanning surfaces with a magnification from 1 m to 1 nm which depends on the hardware used to create the electron beam with various lenses and vacuum systems. Further, it is integrated with an energy dispersion spectrometer to combine the elemental analysis potential on the sample surface. SEM imaging has new characteristics those are backscattering electrons and secondary electrons which increase the scanning potential. The electron gun includes the main parts of the SEM components. With the existence of different magnetic lenses and vacuum systems, SEM has become a unique imaging tool [13].

The characterization method with SEM can deliver visual information on the morphology of the bone surface. SEM images can also be analyzed with an image processing program such as ImageJ, with the output in the form of a histogram of pixels that can provide information about the cavities in the bone and their distribution. From the histogram, bone quality can be known quantitatively by looking at the average pixel value and the percentage of cavity intensity. Schematically, the scan with SEM is shown in **Figure 2**.

From **Figure 2**, Electron Microscopes utilize electrons beam to illuminate a sample and construct an image with high magnification. The electrons from the electron source passing through the condenser lenses, aperture, scanning coil, objective lens, detectors and hit the gold-coated sample positioned on its holder. The condenser lenses center the electron beam in a specific area corresponding to the sample and thus generate the image. Electrons hit the sample surface thereby producing the secondary electrons which are detected by the secondary electron detector and transformed into a signal delivered to a monitor scanner.

Conventional SEM relies on the emanation of auxiliary electrons from the sample surface. As its large focus depth, the SEM is the EM analog of the stereo light

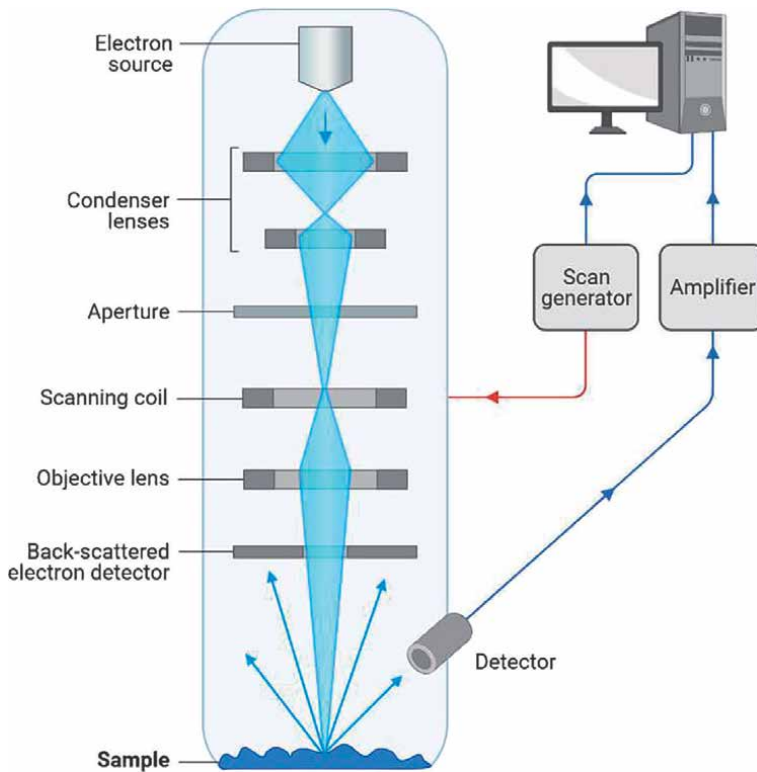


Figure 2.
Schematic flow diagram of a scanning electron microscope [14].

microscope. It gives nitty-gritty pictures of the cell surface and the whole life form. It can moreover be worked for molecule checking and measuring, and for handle control. A SEM, it is so called, because it forms the image by scanning a focused electron beam onto the sample surface in a raster design. The primary electron beam interacting with atoms nearby the surface induces particle emission at any location in the raster. The emissions, for instance, include low energy secondary electrons, high energy scattering electrons, X-rays, and photons that then can be gathered by distinct detectors, and their relative quantities are converted to brightness at every equivalence point on the cathode ray tube (CRT). Due to the considerably smaller raster size than the CRT screen display, the resulting image is the image magnification of the sample. SEMs are equipped with proper equipment such as secondary detectors, backscattering, and X-rays, which can be functioned to analyze the topography and atomic composition of the sample and the surface distribution of immune labels [15, 16].

2.2.2 Transmission electron microscope (TEM)

Transmission electron microscopes are exploited to examine thin samples (parts of tissue, molecules, etc.) that electrons can traverse to produce a projected image. TEM is analogous to a conventional light microscope. Schematically, the scan with TEM is presented in **Figure 3**.

In **Figure 3**, the TEM applies high-energy electrons for imaging. It has been developed since the 1938's. Its operation requires a very high voltage of about 500 – 1000 kV

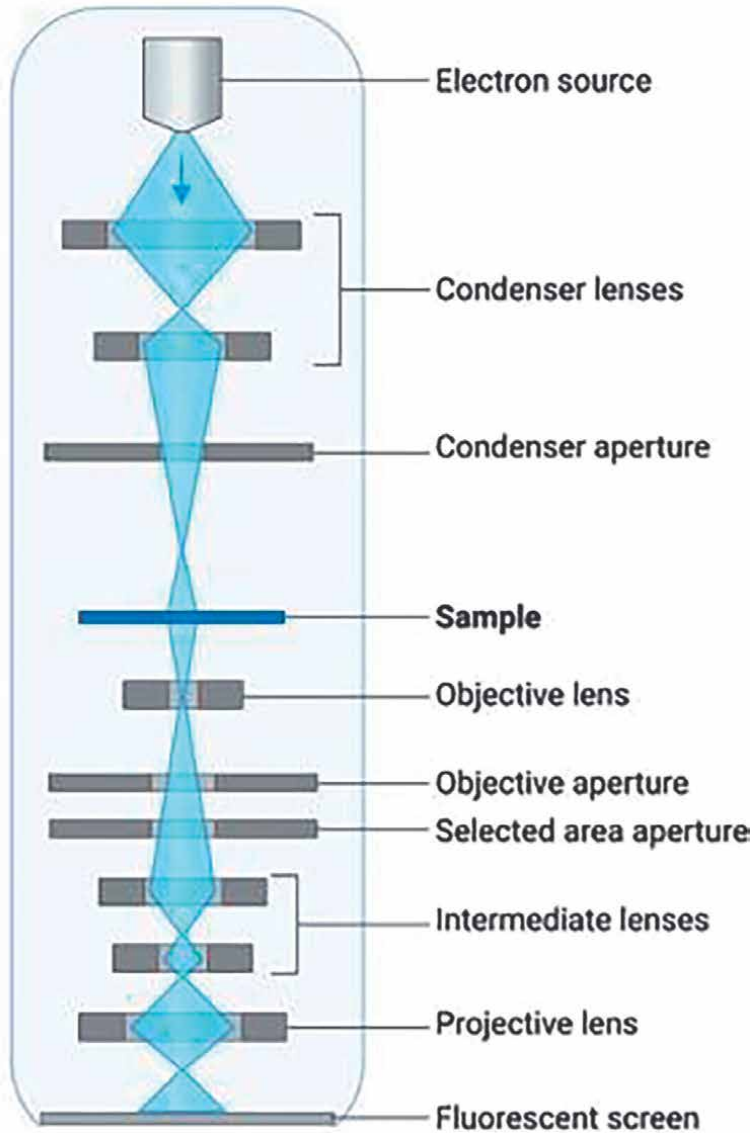


Figure 3. Schematic flow diagram of a transmission electron microscope [14].

with a resolution reaching 0.1 nm. During TEM operation, the electrons beam is generated and transmitted through an ultra-thin sample. Then, the unscattered electrons are transmitted through the sample and hit the fluorescent screen at the bottom of the microscope, thus producing an image. By changing the gun voltage, the electron velocity can be modified which in turn changes the image. Commonly, TEM generates a grayscale image that exhibits lighter and darker regions. The lighter regions demonstrate regions with a large number of transmitted electrons while the darker ones represent a lower number and denser regions in the sample. The sample used in TEM should be prepared thin enough for electrons to be transmitted [17].

2.2.3 Reflection electron microscope (REM)

Another type of development of the electron microscope is the reflection electron microscope (REM). The REM is an electron microscope that has almost the same way of working as TEM, the difference is that REM uses the detection of electron reflections on the object's surface. The sample is semi-infinite and the surface to be observed is almost parallel to the electron beam. The transmitted spot may or may not be observable, depending on the sample size as shown in **Figure 4**. This technique is specifically used in combination with the Reflection High Energy Electron Diffraction (RHEED) technique and the reflection high-energy loss spectrum (RHELS) technique.

REM could be a combination of imaging, diffraction, and spectroscopy procedures for the characterization of topography, crystal structure, and composition of surfaces of single crystals. High-energy electrons are occurring at looking points to the surface and reflected electrons are utilized to create a REM picture. Utilization of REM in analyzing osteoporosis in bone is still rarely done, because REM has several drawbacks including REM images are shortened in the direction of electron events and high resolution is only achieved in the normal direction, so that in analyzing surface topographic details more than one azimuth is needed. Meanwhile, bones that are not homogeneous can produce different images in each image. These

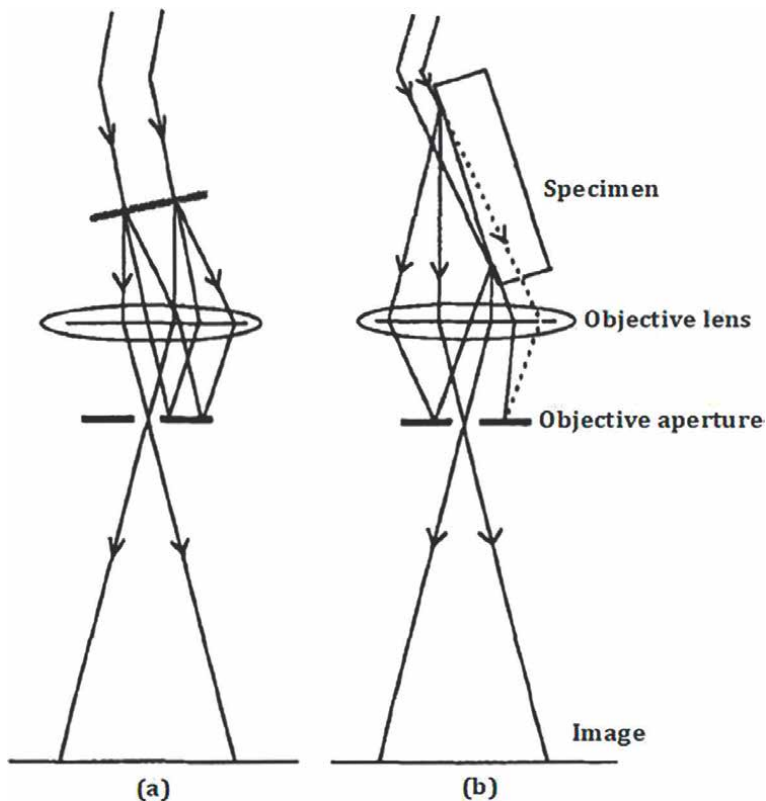


Figure 4.
These ray diagrams illustrate (a) TEM and (b) REM [18].

techniques are applicable to metal [19], semiconductor [20], crystal surfaces [21], surface reconstructions and phase transformations [22], correlation between topographical features and reconstructions, directions, distribution, and motion of surface steps, dislocations on surfaces, nucleation and growth of films, and surface reactions [23].

Sample preparation for REM is the same as for other types of electron microscopy, i.e., it must be ensured that the surface is sufficiently flat and clean. The size of the sample should fit the microscope sample holder by about 3 mm. Then inserted into the electron microscope with a surface normal perpendicular to the optical axis. The nominal size of a REM sample is no more than 1 mm³ for a sample holder which gets 3 mm grids. Hence, the perceptible surface is about 1 mm or less. The lower restraint of the surface area is approximately 10 μm in diameter.

3. Illustrative examples of information acquired

Electron microscopy (EM) is a method to obtain biological and non-biological samples' images with a high-resolution. This method is frequently employed in biomedical research to examine the detailed structure of tissues, cells, organelles, and macromolecular complexes. High-resolution EM images are produced from the use of electrons having very short wavelengths as the illumination source. EM is used in conjunction with numerous additional methods (e.g., thin cutting, immune labeling, and negative staining) to answer specific questions. EM images can deliver crucial information about the structural and morphological basis of bone. Several results of prior studies that investigated bone with EM are presented in **Table 1**.

| Scanning electron microscopy (SEM) | Transmission electron microscopy (TEM) |
|---|--|
| The SEM image exhibited that the longer the time after ovariectomy, the greater the degree of damage seen in the tibial cavity [24] | Acicular crystals of apatite with approximate dimensions of ~20–30 nm by 5 nm. Gap zones and overlap zones in collagen fibrils [25] |
| The group of ovariectomized rats had histograms that increasingly shifted more black areas. Areas that were black or dark relate to cavities in the bone [26] | Apatite crystals that resemble tablet form, in the control group have a longer size, and for groups of ovariectomized rats there was a decrease in size both length and width [26] |
| Network organization in trabecular bone showing topographical details [27] | Different calcium phosphate minerals morphologies in the bone extracellular matrix: dense granules, globular aggregates of needle-like apatite, and mature fibrous minerals [28, 29] |
| Canalicular network with residing osteocytes [30] | Woven arrangement of aligned collagen fibrils in the ordered phase of trabecular bone [31] |
| Osteons and cement line delineating osteonal and interstitial bones [32] | Characteristic collagen banding pattern with a periodicity of ~67 nm [33] |
| Cross-sectional photomontage of an entire human rib bone [34] | Disorganized, entangled collagen fibrils without characteristic banding pattern in the disordered phase of trabecular bone [35] |

Table 1.
Characterization of bone structure by SEM and TEM.

4. Image processing techniques

After obtaining the image from the electron microscope, the next step that needs to be done is to analyze the resulting image. Several applications that can be used to process the output image of an electron microscope, including ImageJ, Matlab, Python, OpenCV, Dragonfly, HyperSpy, and others. Each has its own advantages and disadvantages. However, on this occasion, we will review the analysis of images from

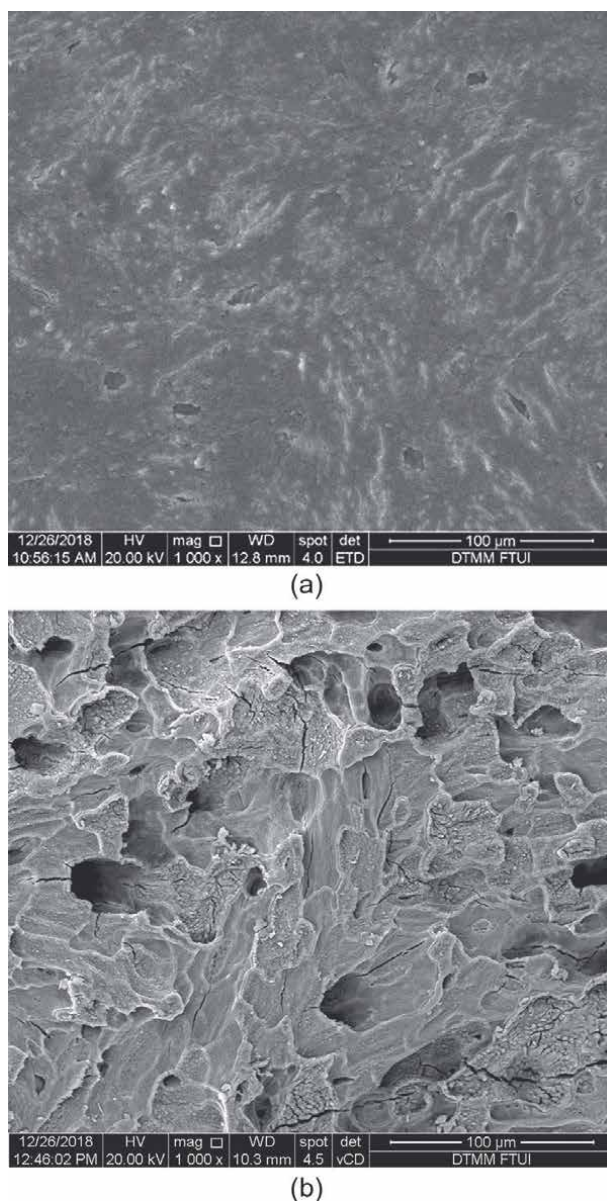
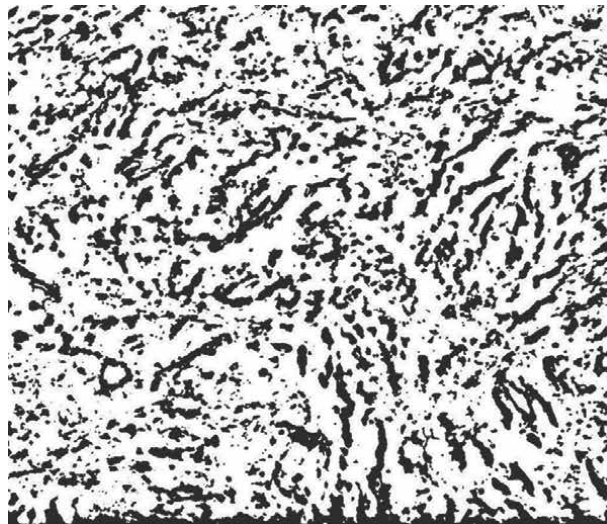


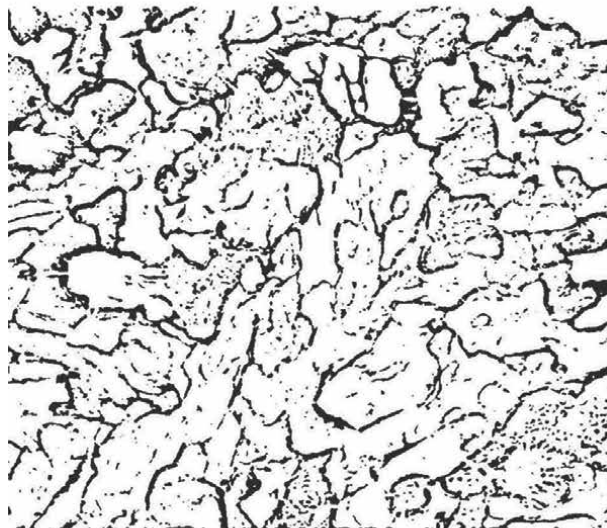
Figure 5. SEM image of the rat femur bone, (a) sham, (b) osteoporosis due to ovariectomy.

electron microscopy using the ImageJ application. **Figure 5** shows the results of SEM imaging of sham rat femur (a) and osteoporosis due to ovariectomy (b).

Figure 5 shows an SEM image of a rat bone taken from the femur at 1000x magnification. **Figure 5(a)** SEM image of the femur bone of a 13-week-old sham rat, visually it can be seen that the surface is denser, there are no large cavities found. This is different from the SEM image shown in **Figure 5(b)**, the image was taken from the femur bones of rats with osteoporosis due to ovariectomy treatment. The surface is clearly visible in the presence of wider cavities. The picture was taken when the rats were 21 weeks old or 9 weeks after being given ovariectomy. In accordance with the results of previous studies, the rats began to show the characteristics of osteoporosis at the ninth week since ovariectomy [36].



(a)



(b)

Figure 6. SEM image of rat femur after analysis with ImageJ, (a) sham, (b) osteoporosis due to ovariectomy.

The characteristics of osteoporosis are clearer from the SEM image that has been analyzed with the help of the ImageJ application as shown in **Figure 6**. **Figure 6(a)** results of the analysis of the sham femur, the black color is thicker and fused together, indicating that the bone is still solid. This is supported by the results of the [37] study which showed that the bones of sham rats contained minerals such as calcium, magnesium, and phosphorus which were still normal. Meanwhile in **Figure 6(b)** the results of the analysis of the femur bones of rats treated with ovariectomy, it appears that the color is lighter, with the black parts that have started to break off and are thinner. This is because ovariectomy treatment can cause a decrease in the hormone estrogen in the body. With a decrease in the hormone estrogen, bone resorption by osteoclasts increases, and conversely osteoblast activity becomes inhibited [38–40]. As a result, bone density will also decrease, and osteoporosis occurs [41]. In addition, a decrease in the hormone estrogen can also increase the resorption of calcium (Ca) in bone, so that bone mass will decrease [42, 43]. Even the absorption of Ca in the intestine also decreases and the excretion of Ca through the kidneys increases [44–46]. All these conditions cause parathyroid hormone activity to increase and bone density to decrease which in turn triggers osteoporosis [47, 48].

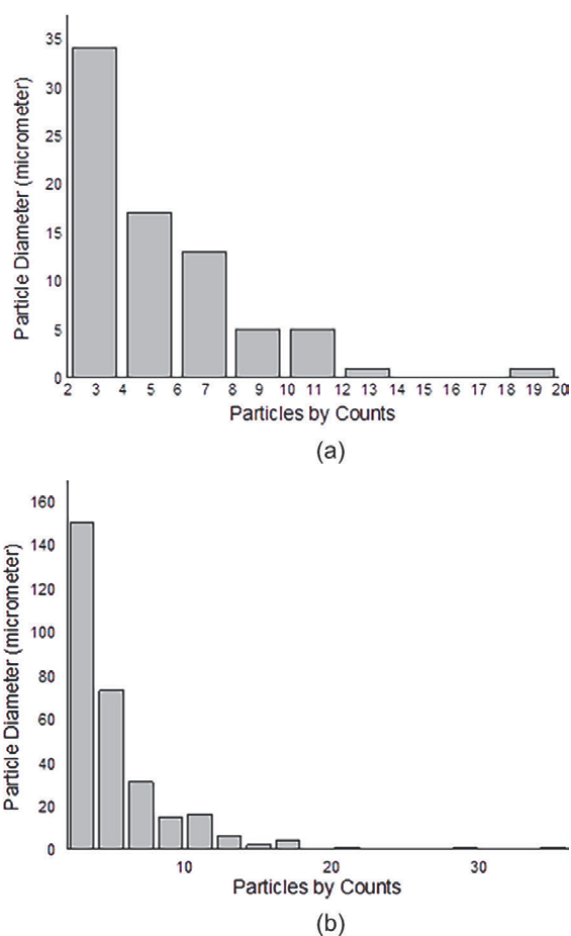


Figure 7. Particle diameter size of the rat femur bone, (a) sham, (b) osteoporosis due to ovariectomy.

Quantitatively several parameters that can be known from SEM image analysis with Image J application include particle diameter, percentage of voids, or porosity analysis. Particle diameter analysis for the same sample as previously mentioned is shown in **Figure 7**. **Figure 7(a)** shows the particle diameter size of the sham rat femur bone ranging from 1.5 to 34.4 μm . The particle diameter experienced a significant increase in the ovariectomized femur bone, the highest size reaching 150.2 μm as shown in **Figure 7(b)**. Larger particle sizes tend to be more porous, as a result, are more brittle [49].

Likewise, TEM images can be analyzed and obtained the same information as for images from SEM. The output of the porosity analysis can also be carried out, some quantitative data can be obtained from the results of the porosity analysis, namely the pore volume and the percentage of pores. Some of these parameters can be used as a reference for osteoporosis analysis in bone, especially in experimental animal models.

5. Conclusions

Imaging at the nanoscale is very important to analyze the quality and structure of bone morphology. This review examines the images produced by electron microscopy of the femur bones of rats under sham conditions and osteoporosis due to ovariectomy. The scanned electron microscopy image with the help of the ImageJ application provides information that the femur bones of ovariectomized rats show signs of osteoporosis. Some of the parameters that characterize the cavities in the ovariectomized femur appear wider, with the edges of the cavity appearing to be cracked. In addition, the particle diameter also increased by an average of 77.16%. Therefore, electron microscopy is one of the best approaches, which can directly provide ultrastructural evidence for bone morphology, and furthermore, the results of this bone morphology analysis can provide insight into the characteristics and processes of osteoporosis.

Acknowledgements

This project was partially funded by “Hibah TADOK Universitas Indonesia” No. 1331/UN2.R3.1/HKP.05.00/2018.

Conflict of interest

The author declares no conflict of interest.

Appendices and nomenclature

| | |
|------|---|
| AAS | Atomic Absorption Spectroscopy |
| DEXA | Dual-Energy X-Ray Absorptiometry |
| EM | Electron Microscopy |
| FTIR | Fourier Transform Infrared Spectroscopy |
| QCT | Quantitative Computer Tomography |
| REM | Reflection Electron Microscope |

SEM Scanning Electron Microscope
TEM Transmission Electron Microscope
UV Ultraviolet
XRD X-Ray Diffraction

Units

kV Kilovolt
nm Nanometer
 μm Micrometer

Author details


Neng Nenden Mulyaningsih^{1*} and Rum Sapundani²

1 Department of Physics Education, Universitas Indraprasta PGRI, Jakarta, Indonesia

2 Department of Electromedical Engineering, Universitas Muhammadiyah Purwokerto, Indonesia

*Address all correspondence to: nengnendenmulyaningsih@gmail.com

IntechOpen

© 2022 The Author(s). Licensee IntechOpen. This chapter is distributed under the terms of the Creative Commons Attribution License (<http://creativecommons.org/licenses/by/3.0>), which permits unrestricted use, distribution, and reproduction in any medium, provided the original work is properly cited. 

References

- [1] Rubin CD. Emerging concepts in osteoporosis and bone strength. *Current Medical Research and Opinion*. 2005;**21**(7):1049-1056. DOI: 10.1185/030079905X50525
- [2] Sözen T, Özışık L, Başaran NÇ. An overview and management of osteoporosis. *European Journal of Rheumatology*. 2017;**4**(1):46. DOI: 10.5152/eurjrheum.2016.048
- [3] Hirschfeld HP, Kinsella R, Duque GJ. Osteosarcopenia: Where bone, muscle, and fat collide. *Osteoporosis International*. 2017;**28**(10):2781-2790. DOI: 10.1007/s00198-017-4151-8
- [4] Krug R, Burghardt AJ, Majumdar S, Link TM. High-resolution imaging techniques for the assessment of osteoporosis. *Radiologic Clinics*. 2010;**48**(3):601-621. DOI: 10.1016/j.rcl.2010.02.015
- [5] Lorentzon M, Cummings SR. Osteoporosis: The evolution of a diagnosis. *Journal of Internal Medicine*. 2015;**277**(6):650-661. DOI: 10.1111/joim.12369
- [6] Tenforde AS, Parziale AL, Popp KL, Ackerman KE. Low bone mineral density in male athletes is associated with bone stress injuries at anatomic sites with greater trabecular composition. *The American Journal of Sports Medicine*. 2018;**46**(1):30-36. DOI: 10.1177/0363546517730584
- [7] Bae YJ, Kim MH. Calcium and magnesium supplementation improves serum OPG/RANKL in calcium-deficient ovariectomized rats. *Calcified Tissue International*. 2010;**87**(4):365-372. DOI: 10.1007/s00223-010-9410-z
- [8] El Khassawna T, Böcker W, Govindarajan P, Schliepke N, Hürter B, Kampschulte M, et al. Effects of multi-deficiencies-diet on bone parameters of peripheral bone in ovariectomized mature rat. *PLoS One*. 2013;**8**(8):e71665. DOI: 10.1371/journal.pone.0071665
- [9] Park B, Song HS, Kwon JE, Cho SM, Jang SA, Kim MY, et al. Effects of salvia miltiorrhiza extract with supplemental liquefied calcium on osteoporosis in calcium-deficient ovariectomized mice. *BMC Complementary and Alternative Medicine*. 2017;**17**(1):1-5. DOI: 10.1186/s12906-017-2047-y
- [10] Quintero-García M, Gutiérrez-Cortez E, Rojas-Molina A, Mendoza-Ávila M, Del Real A, Rubio E, et al. Calcium bioavailability of *Opuntia ficus-indica* cladodes in an ovariectomized rat model of postmenopausal bone loss. *Nutrients*. 2020;**12**(5):1431. DOI: 10.3390/nu12051431
- [11] Tripsas M. Surviving radical technological change through dynamic capability: Evidence from the typesetter industry. *Industrial and Corporate Change*. 1997;**6**(2):341-377. DOI: 10.1093/icc/6.2.341
- [12] Fisher RM. 2.13 highlights in the development of electron microscopy in the United States: A bibliography and commentary of published accounts and EMSA records. *Advances in Imaging and Electron Physics*. 1996;**96**:347-382. DOI: 10.1016/S1076-5670(08)70055-7
- [13] Akhtar K, Khan SA, Khan SB, Asiri AM. Scanning electron microscopy: Principle and applications in nanomaterials characterization. In: *Handbook of Materials Characterization*. New York: Springer International Publishing AG; 2018. pp. 113-145. DOI: 10.1007/978-3-319-92955-2_4
- [14] BioRender. What is Electron Microscopy? Principle, Types, and

Importance [Internet]. Available from: <https://researchtweet.com/what-is-electron-microscopy-principle-types/>. [Accessed: 2022-02-15]

[15] Bergmann U, Manning PL, Wogelius RA. Chemical mapping of paleontological and archeological artifacts with synchrotron X-rays. *Annual Review of Analytical Chemistry*. 2012;5:361-389. DOI: 10.1146/annurev-anchem-062011-143019

[16] Christopher ME, Warmenhoeven JW, Romolo FS, Donghi M, Webb RP, Jaynes C, et al. A new quantitative method for gunshot residue analysis by ion beam analysis. *Analyst*. 2013;138(16):4649-4655. DOI: 10.1039/C3AN00597F

[17] Inkson BJ. Scanning electron microscopy (SEM) and transmission electron microscopy (TEM) for materials characterization. In: *Materials Characterization Using Nondestructive Evaluation (NDE) Methods*. United Kingdom: Woodhead Publishing; 2016. pp. 17-43. DOI: 10.1016/B978-0-08-100040-3.00002-X

[18] Hsu T. Technique of reflection electron microscopy. *Microscopy Research and Technique*. 1992;20:318-332. DOI: 10.1002/jemt.1070200403

[19] Yamaguchi H, Ohkawa T, Yagi K. Surface electromigration of metal atoms on modified Si(111) surfaces studied by REM. *Ultramicroscopy*. 1993;52(3-4):306-311. DOI: 10.1016/0304-3991(93)90040-5

[20] Rogilo DI, Fedina LI, Ponomarev SA, Sheglov DV, Latyshev AV. Etching of step-bunched Si(111) surface by Se molecular beam observed by in situ REM. *Journal of Crystal Growth*. 2020;529:125273. DOI: 10.1016/j.jcrysgro.2019.125273

[21] Peng LM. Illumination of crystal surfaces in the electron microscope

under RHEED and REM geometry. *Ultramicroscopy*. 1990;32(2):169-175. DOI: 10.1016/0304-3991(90)90034-J

[22] Latyshev AV, Krasilnikov AB, Aseev AL. Application of ultrahigh vacuum reflection electron microscopy for the study of clean silicon surfaces in sublimation, epitaxy, and phase transitions. *Microscopy Research and Technique*. 1992;20(4):341-351. DOI: 10.1002/jemt.1070200405

[23] Kawarada H, Sasaki H, Sato A. Scanning-tunneling-microscope observation of the homoepitaxial diamond (001) 2×1 reconstruction observed under atmospheric pressure. *Physical Review B*. 1995;52(15):11351. DOI: 10.1103/physrevb.52.11351

[24] Mulyaningsih NN, Juwono AL, Soejoko DS, Astuti DA. Multi-hole spherical CT scan method to characterize large quantities of bones in rats. *Medical Journal of Indonesia*. 2021;30(3):182-190. DOI: 10.13181/mji.oa.215452

[25] Schwarcz HP, McNally EA, Botton GA. Dark-field transmission electron microscopy of cortical bone reveals details of extrafibrillar crystals. *Journal of Structural Biology*. 2014;188:240-248. DOI: 10.1016/j.jsb.2014.10.005

[26] Mulyaningsih NN, Juwono AL, Soejoko DS, Astuti DA. Morphology of proximal cortical epiphysis bone of ovariectomized *Rattus norvegicus*. *Turk Osteoporoz Dergisi*. 2021;26(3):169-174. DOI: 10.4274/tod.galenos.2020.36002

[27] Boyde A. Improved digital SEM of cancellous bone: Scanning direction of detection, through focus for in-focus and sample orientation. *Journal of Anatomy*. 2003;202:183-194. DOI: 10.1046/j.1469-7580.2003.00146.x

- [28] Nitiputri K, Ramasse QM, Autefage H, McGilvery CM, Boonrungsiman S, Evans ND, et al. Nanoanalytical electron microscopy reveals a sequential mineralization process involving carbonate-containing amorphous precursors. *ACS Nano*. 2016;**10**:6826–6835. DOI: 10.1021/acsnano.6b02443
- [29] Boonrungsiman S, Gentleman E, Carzaniga R, Evans ND, McComb DW, Porter AE, et al. The role of intracellular calcium phosphate in osteoblast-mediated bone apatite formation. *Proceedings of the National Academy of Sciences of the United States of America*. 2012;**109**:14170–14175. DOI: 10.1073/pnas.1208916109
- [30] Feng JQ, Ward LM, Liu S, Lu Y, Xie Y, Yuan B, et al. Loss of DMP1 causes rickets and Osteomalacia and identifies a role for osteocytes in mineral metabolism. *Nature Genetics*. 2006;**38**:1310–1315. DOI: 10.1038/ng1905
- [31] Tertuliano OA, Greer JR. The nanocomposite nature of bone drives its strength and damage resistance. *Nature Materials*. 2016;**15**:1195–1202. DOI: 10.1038/nmat4719
- [32] Skedros JG, Holmes JL, Vajda EG, Bloebaum RD. Cement lines of secondary osteons in human bone are not mineral-deficient: New data in a historical perspective. *The Anatomical Record Part A: Discoveries in Molecular, Cellular, and Evolutionary Biology*. 2005;**286**:781–803. DOI: 10.1002/ara.20214
- [33] Jantou-Morris V, Horton MA, McComb DW. The Nano-morphological relationships between apatite crystals and collagen fibrils in ivory dentine. *Biomaterials*. 2010;**31**:5275–5286. DOI: 10.1016/j.biomaterials.2010.03.025
- [34] Bereshiem AC, Pfeiffer SK, Grynypas MD, Alblas A. Use of backscattered scanning electron microscopy to quantify the bone tissues of midthoracic human ribs. *American Journal of Physical Anthropology*. 2019;**168**:262–278. DOI: 10.1002/ajpa.23716
- [35] Al-Barghouthi BM, Mesner LD, Calabrese GM, Brooks D, Tommasini SM, Bouxsein ML, et al. Systems genetics in diversity outbred mice inform BMD GWAS and identify determinants of bone strength. *Nature Communications*. 2021;**12**(1):1–9. DOI: 10.1038/s41467-021-23649-0
- [36] Mulyaningsih NN, Juwono AL, Soejoko DS, Astuti DA. Effect of giving Nano calcium phosphate diet on mineral content and function groups of ovariectomy tibia rats. *Asian Journal of Applied Sciences*. 2019;**7**(5):666–681. DOI: 10.24203/ajas.v7i5.5945
- [37] Ooi FK, Norsyam WM, Ghosh AK, Sulaiman SA, Chen CK, Hung LK. Effects of short-term swimming exercise on bone mineral density, geometry, and microstructural properties in sham and ovariectomized rats. *Journal of Exercise Science & Fitness*. 2014;**12**(2):80–87. DOI: 10.1016/j.jesf.2014.09.001
- [38] Chow J, Tobias JH, Colston KW, Chambers TJ. Estrogen maintains trabecular bone volume in rats not only by suppression of bone resorption but also by stimulation of bone formation. *The Journal of Clinical Investigation*. 1992;**89**:74–78. DOI: 10.1172/JCI115588
- [39] Majeska RJ, Ryaby JT, Einhorn TA. Direct modulation of osteoblastic activity with estrogen. *The Journal of Bone and Joint Surgery*. American Volume. 1994;**76**:713–721. DOI: 10.2106/00004623-199405000-00013
- [40] Qu Q, Perala-Heape M, Kapanen A, Dahllund J, Salo J, Vaananen HK, et al.

Estrogen enhances differentiation of osteoblasts in mouse bone marrow culture. *Bone*. 1998;**22**:201-209.
DOI: 10.1016/s8756-3282(97)00276-7

[41] Rocca WA, Grossardt BR, Shuster LT. Oophorectomy, menopause, estrogen treatment, and cognitive aging: Clinical evidence for a window of opportunity. *Brain Research*. 2011;**1379**:188-198.
DOI: 10.1016/j.brainres.2010.10.031

[42] Holzherr ML, Retallack RW, Gutteridge DH, Price RI, Faulkner DI, Wilson SG, et al. Calcium absorption in postmenopausal osteoporosis: Benefit of HRT plus kalsitriol, but not HRT alone, in both malabsorbers and normal absorbers. *Osteoporosis International*. 2000;**11**:43-51. DOI: 10.1007/s001980050005

[43] Van den Heuvel EG, Schoterman MH, Muijs T. Transgalactooligo-saccharides stimulate calcium absorption in postmenopausal women. *The Journal of Nutrition*. 2000;**130**:2938-2942.
DOI: 10.1093/jn/130.12.2938

[44] Hoenderop JG, Van der Kemp AW, Hartog A, Van de Graaf SF, Van Os CH, Willems PH, et al. Molecular identification of the apical Ca²⁺ channel in 1,25-dihydroxyvitamin D₃-responsive epithelia. *The Journal of Biological Chemistry*. 1999;**274**:8375-8378.
DOI: 10.1074/jbc.274.13.8375

[45] Van Abel M, Hoenderop JGJ, Dardenne O, Arnaud RST, Van Os CH, Van Leeuwen HJPTM, et al. 1,25-Dihydroxyvitamin D₃-independent stimulatory effect of estrogen on the expression of ECAC1 in the kidney. *Journal of the American Society of Nephrology*. 2002;**13**:2102-2109. DOI: 10.1097/01.ASN.0000022423.34922.2A

[46] Van Abel M, Hoenderop JGJ, Van Der Kemp AW, Van Leeuwen JP, Bindels RJM.

Regulation of the epithelial Ca²⁺ channels in small intestine as studied by quantitative mRNA detection. *American Journal of Physiology. Gastrointestinal and Liver Physiology*. 2003;**285**:978-985.
DOI: 10.1152/ajpgi.00036.2003

[47] Khosla S, Atkinson EJ, Melton LJIII, Riggs BL. Effects of age and estrogen status on parathyroid hormone levels and biochemical markers of bone turnover in women: A population-based study. *The Journal of Clinical Endocrinology and Metabolism*. 1997;**82**:1522-1527.
DOI: 10.1210/jcem.82.5.3946

[48] Notelovitz M. Estrogen therapy and osteoporosis: Principles & practice. *The American Journal of the Medical Sciences*. 1997;**313**(1):2-12. DOI: 10.1097/00000441-199701000-00002

[49] Noor Z, Sumitro SB, Hidayat M, Rahim AH, Taufik A. Assessment of microarchitecture and crystal structure of hydroxyapatite in osteoporosis. *Universa Medicina*. 2011;**30**:29-35.
DOI: 10.18051/UnivMed.2011.v30.29-35

Application of Transmission Electron Microscopy to Detect Changes in Pancreas Physiology

Maša Skelin Klemen, Jurij Dolensšek, Ismael Valladolid-Acebes, Andraž Stožer and Saška Lipovšek

Abstract

Insulin resistance in key target organs and beta cell dysfunction due to gluco- and lipotoxicity, are the two main factors driving type 2 diabetes mellitus pathogenesis. Recently, it has been suggested that ectopic fat deposition in the pancreas, named non-alcoholic fatty pancreas disease, occurs in metabolic syndrome, and may play an etiological role in islet dysfunction and damage the exocrine pancreas, increasing its susceptibility to pancreatitis and pancreatic cancer. In this chapter, we present transmission electron microscopy (TEM) as a valuable method to detect early changes in the ultrastructure of pancreatic cells during the development of the metabolic syndrome in mice fed with a western diet (WD). Mice fed with a WD develop pathological ultrastructural alterations in the exocrine and endocrine cells. We demonstrate how to use image segmentation methods and ultrastructural morphometry to analyze and quantify structural changes in cellular organelles and evaluate the presence of lipid droplets, autophagic structures, and vacuolization. Since ultrastructural lesions can be detected early during the progression of the metabolic syndrome, are in many aspects subtle, and by far precede cell apoptosis, necrosis, fat infiltration, and overt functional changes, TEM is not only a suitable but probably the crucial method for detecting early pancreas dysfunction.

Keywords: pancreas physiology, exocrine cells, endocrine cells, ultrastructure, metabolic syndrome, type 2 diabetes mellitus, western diet

1. Introduction

The number of people with type 2 diabetes mellitus (T2DM) is growing rapidly worldwide and has already exceeded 530 million in 2021 [1]. Because of the severe consequences of T2DM for patients and the enormous burden on the healthcare system, a lot of research is focused on understanding the development of T2DM. The healthy pancreatic beta cells secrete insulin at a basal rate throughout the day and increase secretion in response to stimulation with nutrients, especially glucose, and other neurohormonal secretagogues, such as acetylcholine and GLP-1, after a meal [2–4]. Understanding the pathophysiology of early phases of glucose tolerance

disruption associated with morphological and functional beta cell changes present in insulin-resistant people susceptible to the development of T2DM is especially important and has been the focus of many research groups [5–9]. However, to date very limited information is available about the ultrastructural alterations of beta cells during the early stages of T2DM development [10–13].

Thus, the aim of our chapter is to present the importance and illustrate the usefulness of transmission electron microscopy (TEM) in the research field of pancreas physiology through specific and easily reproducible examples. TEM is a technique used to obtain ultrahigh-resolution images of different samples. The prototype of the transmission electron microscope was developed by Ernst Ruska and Max Knoll in 1931. Since then, TEM has been extensively used in biomedical research, helping us deepen our knowledge about the ultrastructure of cells and understanding the cellular processes. TEM was first used to identify specific features of pancreatic endocrine and exocrine cells in the mid-1950s by Paul Lacy [14] and George Palade [15], respectively. TEM exploits the wavelength properties of electrons to provide greater spatial resolution than the resolution achieved using photons in light microscopy (LM). In TEM, a beam of high-voltage electrons is emitted by the electron gun and then passed through the sample. The most challenging part of TEM is the preparation of samples that are thin and robust enough to allow electrons to penetrate the sample on the one hand and survive the damage caused by the electron beam on the other. In this chapter, TEM is implemented as an appropriate research method that allows us to detect very subtle structural changes in pancreas cells of mice fed with a western diet (WD). Here, we focus on sample preparation, microscopy, and quantitative analysis of ultrastructure, together with some representative results, to illustrate the utility and emphasize the importance of TEM in pancreas research. A comprehensive analysis of ultrastructural changes in WD-fed mice with partly compensated diabetes mellitus will be present in detail elsewhere.

In the first part of this chapter, we briefly summarize the basic anatomical features of the pancreas in humans and mice and describe the main physiological characteristics of the endocrine and exocrine pancreas. Next, we describe the development of T2DM, focusing on the role of obesity and key pathophysiological events. In the central part of this chapter, we discuss the ultrastructural morphology and describe the methodology used for ultrastructural morphometry of the exocrine and endocrine pancreas during the early stages of WD-induced T2DM development.

2. Structure and function of the pancreas

The pancreas is an unpaired gland of the alimentary tract with two different but complementary functions: the production of digestive enzymes and alkaline fluid in exocrine cells that help with the breakdown of energy-rich nutrients and the synthesis by endocrine cells of hormones needed to control the storage and usage of energy-rich nutrients [16]. In humans, the pancreas is a well-defined organ with three major parts: the head, the body, and the tail, extending from the duodenum to the spleen [17, 18]. In mice, the pancreas is not as well-defined as in humans but is rather diffusely distributed in a dendritic manner while it is still composed of three major parts: the duodenal lobe, the largest splenic lobe, and the smallest gastric lobe [19]. A fibrous capsule surrounds the pancreas, and the connective tissue extending into the gland divides the parenchyma into larger lobes and smaller lobules [18, 20]. Each lobule is composed of acini that consists of pyramid-shaped acinar cells [21]. The exocrine part accounts for

96–99% and the endocrine islets of Langerhans for the remaining 1–4% of total pancreas parenchyma [22, 23]. In mice, the islets are mainly interlobular, while in humans they are usually intralobular, mostly on the edge of lobules [24, 25]. Despite some differences [26], islets of Langerhans from mice and men possess many structural and functional similarities [27, 28]. They are round to oval, vary in size, and range from a few to several thousand endocrine cells. Importantly, the islet size distributions are similar in humans and mice (and also many other species) [22]. At least five different types of endocrine cells can be found in islets in both species [27]. Most numerous are the beta cells that synthesize and secrete insulin. Alpha cells secrete glucagon, while delta cells and PP cells release somatostatin and pancreatic polypeptide, respectively. Finally, epsilon cells are the least abundant, synthesizing and secreting ghrelin [23–25].

As mentioned above, the exocrine pancreas plays a crucial role in the enzymatic digestion of carbohydrates, proteins, and lipids and secretes a bicarbonate-rich fluid [29–31]. The enzymes are stored in an inactive proenzyme form in the so-called zymogene granules located at the apical membrane of acinar cells and are released in response to stimulation by neurohormonal secretagogues, such as acetylcholine and cholecystokinin, via exocytosis. The fusion of granules with the apical plasma membrane releases the enzymes first into the acinar lumen, from where they pass via the ductal tree into the small intestine [32]. In contrast, islets release their hormones into the numerous islet blood capillaries that drain into the portal venous system. In the liver and other key target tissues, such as the skeletal muscle and adipose tissue, insulin acts as a key anabolic hormone, promoting glycogenesis, glycolysis, lipogenesis, and proteinogenesis, and suppressing gluconeogenesis, lipolysis, and proteolysis [33–35]. On the other hand, glucagon acts mainly in the liver, where it promotes glycogenolysis and gluconeogenesis, and inhibits glycolysis and glycogenesis [36, 37].

3. The role of obesity in the development of type 2 diabetes

The decrease in insulin action indicates insulin resistance, the main hallmark of T2DM [38]. Several factors play a role in the development of insulin resistance, with obesity probably being the most important one [39]. During the last three decades, obesity has reached an epidemic stage in all age groups [40]. Increased intake of energy-dense foods containing a high percentage of fat and carbohydrates, combined with a lack of physical activity, leads to a net positive energy balance and represents the primary cause of obesity. The first stages of obesity are hypertrophy and hyperplasia, where adipocytes try to meet the demand to store excessive energy. When levels of free fatty acids and triglycerides exceed the metabolic capacity of adipose tissue, they accumulate as ectopic fat in non-adipose tissue such as the liver, pancreas, skeletal muscles, and heart [41]. The regional distribution of adipose tissue is particularly important for the development of disorders of glucose and lipid metabolism [42, 43]. The fat infiltration in the liver and pancreas in the absence of excess alcohol intake is termed non-alcoholic fatty liver disease (NAFLD) and non-alcoholic fatty pancreas disease (NAFPD), respectively [44]. Due to fat accumulation in hepatocytes, NAFLD leads to inflammation, fibrosis, cirrhosis, and liver cancer and critically affects insulin sensitivity in the liver [44–46]. NAFPD plays a similar role in the dysfunction of the endocrine and exocrine pancreas leading to exacerbation of acute pancreatitis and increasing the susceptibility to pancreatic cancer [46–50]. Although the concept of the NAFPD was introduced only a few years ago [51], the correlation between fat infiltration and pancreas was first described almost a century ago on

obese cadavers having larger pancreata compared to non-obese cadavers [52, 53]. Importantly, over the last decade, it has been demonstrated convincingly that most of the morphological, functional, and clinical features of T2DM are reversible with sufficient weight loss and that these positive changes depend on the level of hepatic and pancreatic fat reduction [54–56].

Although insulin resistance is one of the main features of T2DM, it is not sufficient for the development of T2DM. Despite increasing insulin resistance, present long before the onset of diabetes, individuals with preserved beta cell capacity can stay normoglycemic for several years due to compensatory insulin hypersecretion. Furthermore, a certain proportion of individuals with insulin resistance never develop T2DM. The idea has been put forward that there may be a personal fat threshold or an individual level of susceptibility to developing T2DM at a given body mass index, with the main mechanisms behind this attractive hypothesis being varying degrees of fat accumulation in the liver and the pancreas, together with varying individual responses to this accumulation [57]. An obese subject with insulin resistance can secrete 2–5 times more insulin compared to lean non-diabetic individuals in response to a glycemic load, but when the adaptive capacity of the beta cells fails, T2DM occurs [58]. Several studies have shown that the first phase of insulin secretion is primarily affected, resulting in impaired glucose tolerance. During the progression of T2DM, the second phase of insulin secretion is further lost. Post-translational defects in insulin synthesis also occur, resulting in increased proinsulin secretion, and by the time the diagnosis of T2DM is made, the beta cell function is already typically reduced by 80% [59]. This beta cell failure is responsible for transitioning from an insulin-resistant compensated state to overt T2DM and remains to be elucidated in details. It probably involves an initially inadequate beta cell mass and an insufficiently increased response of the existing beta cells to increased insulin demand [60]. Noteworthy, the susceptibility of beta cells themselves to developing insulin resistance may play an important pathophysiological role [61]. Individuals with T2DM can display changes in beta cell mass, either due to a decrease in beta cell proliferation or/and an increase in cell apoptosis [62]. In T2DM patients, the apoptosis rate is increased severalfold compared to normoglycemic individuals [63], a phenomenon confirmed by ultrastructural analysis using TEM [64]. Furthermore, during T2DM gradual dedifferentiation of beta cells occurs in animal models, while the role of dedifferentiation during the development of human T2DM is controversial and less well-studied [63, 65–68]. Chronic exposure of islets to elevated levels of glucose, fatty acids, and amino acids results in ER stress due to increased insulin synthesis and secretion [69]. The protein folding capacity of ER becomes exceeded, which leads to the activation of the so-called unfolded protein response (UPR) and consequently to the inhibition of protein translation [70, 71]. Gluco- and lipotoxicity cause a vicious cycle of continuous deterioration of the glucometabolic state and eventually impair insulin secretion and increase apoptosis. In T2DM, not only the islet cells are affected, but also the pancreatic acinar cell viability and growth decrease, leading to increased apoptosis and replacement by fat [72, 73]. Importantly, intracellular fat in acinar cells may affect beta cell function in a paracrine manner through the release of adipokines. It is also likely to play a role in pancreatic carcinogenesis, seems to be associated with changes in innervation, and may initiate an acinar-to-adipocyte trans-differentiation [56].

4. Application of TEM in pancreas physiology

Glucose-induced insulin secretion is based on oxidative metabolism, thus mitochondrial function is of crucial importance for beta cells [74]. Mutations in mitochondrial

DNA result in reduced insulin secretion and hyperglycemia [75]. The genetic background is not the only factor affecting mitochondrial function. The diabetic environment, with chronic hyperglycemia, can also affect mitochondria [76]. Such a milieu could be responsible for the progression of T2DM and the reduced capacity of insulin release in these patients. Mitochondria appear round-shaped and hypertrophic in endocrine cells from T2DM islets [76–78]. Besides mitochondria, the structure of other cellular organelles is also altered [79]. The volume density of the endoplasmic reticulum is typically increased, and autophagic vacuoles are present [78, 80, 81]. TEM is also a very useful technique that enables us to identify apoptotic cells [82].

Several studies showed that TEM is suitable to detect morphological characteristics of the diabetic pancreas, but only a few studies have reported results in quantitative terms. Due to the large variability and plasticity of cells and their organelles, especially mitochondria, qualitative evaluations are not sufficient [83]. Furthermore, quantitative morphometry is needed to evaluate subtle structural changes early during the progression of the metabolic syndrome that may precede overt functional changes occurring during the development of T2DM.

Since mouse models of T2DM exhibit comparable developmental features and can provide significant insight into the mechanisms of T2DM development in humans [84], they are widely used in these studies. From several animal models, C57Bl/6 J mice have been the most susceptible to the development of the metabolic syndrome and diet-induced diabetes [85–89]. We performed the morphological and morphometric evaluation of pancreatic endocrine and exocrine tissue obtained from C57Bl/6J mice fed with control diet (CD) or western diet (WD). During 8 weeks on WD, these mice developed obesity, hyperglycemia, and hyperinsulinemia (data not shown). Pancreatic tissue samples were taken in parallel with the preparation of acute pancreas tissue slices intended for electrophysiological studies, confocal calcium imaging, and expression analyses. Although the functional response to glucose in terms of intracellular calcium concentration changes and sensitivity of the exocytotic machinery to calcium were well preserved in WD mice (data not shown), TEM revealed severe morphological changes in the endocrine and exocrine part of the pancreas. In the following section, we demonstrate how to use image segmentation methods and ultrastructural morphometry to analyze and quantify structural changes in the rough endoplasmic reticulum, mitochondria, and exocytotic vesicles and vacuolization in the endocrine and exocrine part of the pancreas from control animals and animals fed with WD. These ultrastructural lesions presented below can be detected early during the progression of the metabolic syndrome and precede cell apoptosis, necrosis, fat infiltration, and overt functional changes. Therefore, TEM enables a more direct assessment of the functional characteristics of the pancreatic tissue and is therefore a suitable and probably the crucial method for detecting alterations associated with early pancreas dysfunction.

5. Sample preparation and analysis

5.1 Ethical statement

The study protocol was approved by the Administration for Food Safety, Veterinary Sector and Plant Protection, Ministry of agriculture, Forestry and Food Republic of Slovenia (approval number: U34401–12/2015/3). The study was conducted in strict accordance with all national and European recommendations pertaining to care and work with laboratory animals, and every effort was made to minimize animal suffering.

5.2 Animals, tissue preparation, light, and transmission electron microscopy

Experiments were performed on 20–22-week-old male C57BL/6 J (RRID: IMSR_JAX:000664) mice purchased from Charles River (**Figure 1A**). Upon weaning, mice were fed with a standard rodent diet (CD, R70, Lantmännen, Stockholm, Sweden) with 72% of kcal from carbohydrates, 10% from fat, and 18% from protein until 12 weeks of age. From 12 to 20 weeks of age, a control group continued to be fed with CD while the second group was fed with WD (D12079B, Research diets inc., New Jersey, USA) containing 43% kcal from carbohydrates, 40% from fats and 17% from proteins (**Figure 1B**). Water was available *ad libitum*. Mice were housed in individually ventilated cages (Allentown LLC, USA) in groups of 1–4 animals per cage at 20–24°C, 45–65% relative humidity, and a 12-hour day-night lighting cycle. The bright part of the cycle was between 7 pm and 7 am. Mice were weighed before sacrifice.

Acute pancreas tissue slices from CD and WD mice were prepared as described previously [90–92]. For light microscopy (LM) and transmission electron microscopy (TEM), a small piece of the pancreatic splenic lobe was clamped using hemostatic forceps to avoid the leakage of agarose into this part of the pancreas. After removal from the body, small fragments of the pancreas were fixed in 2.45% glutaraldehyde and 2.45% paraformaldehyde in a 0.1M sodium cacodylate buffer (pH 7.4) at room temperature for 3 h, and at 4°C for 12 h. The tissue was washed in a 0.1 M sodium cacodylate buffer (pH 7.4) at room temperature for 4 h and post-fixed with 2% OsO₄ at room temperature for 2 h. After washing in a 0.1 M sodium cacodylate buffer (pH 7.4) at room temperature for 3 hours, the tissue was dehydrated in a graded series of ethanol (50%, 70%, 90%, 96%, and 100%, each for 30 minutes at room temperature). The pieces of the tissue were embedded in TAAB embedding resin (Agar Scientific Ltd., Essex, England). For LM, semithin sections (2 μm) were stained with 0.5% toluidine blue in an aqueous solution. For TEM, ultrathin sections (70–75 nm) of the tissue were stained with uranyl acetate and lead citrate and analyzed with a Zeiss EM 902 transmission electron microscope.

5.3 Structure of the exocrine and endocrine pancreas

5.3.1 Qualitative analysis of exocrine and endocrine cell ultrastructure

The pancreas is composed of exocrine and endocrine tissue and this functional specialization can readily be recognized microscopically (**Figure 2**).

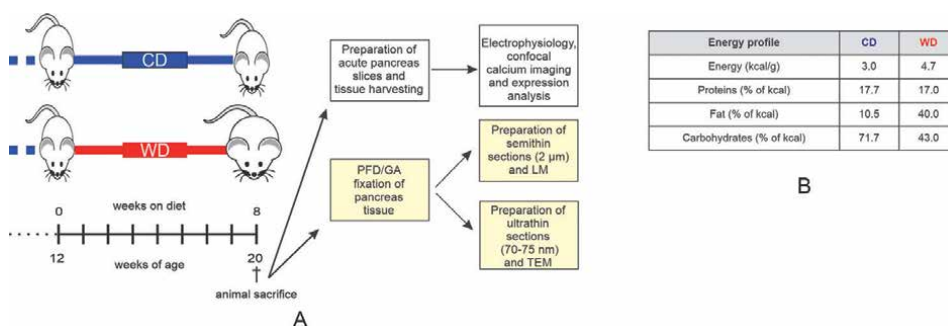


Figure 1.

Study design (A) timeline of the study. The part of the project shown in yellow is presented in this chapter. (B) Energy profile of control diet (CD) and western diet (WD).

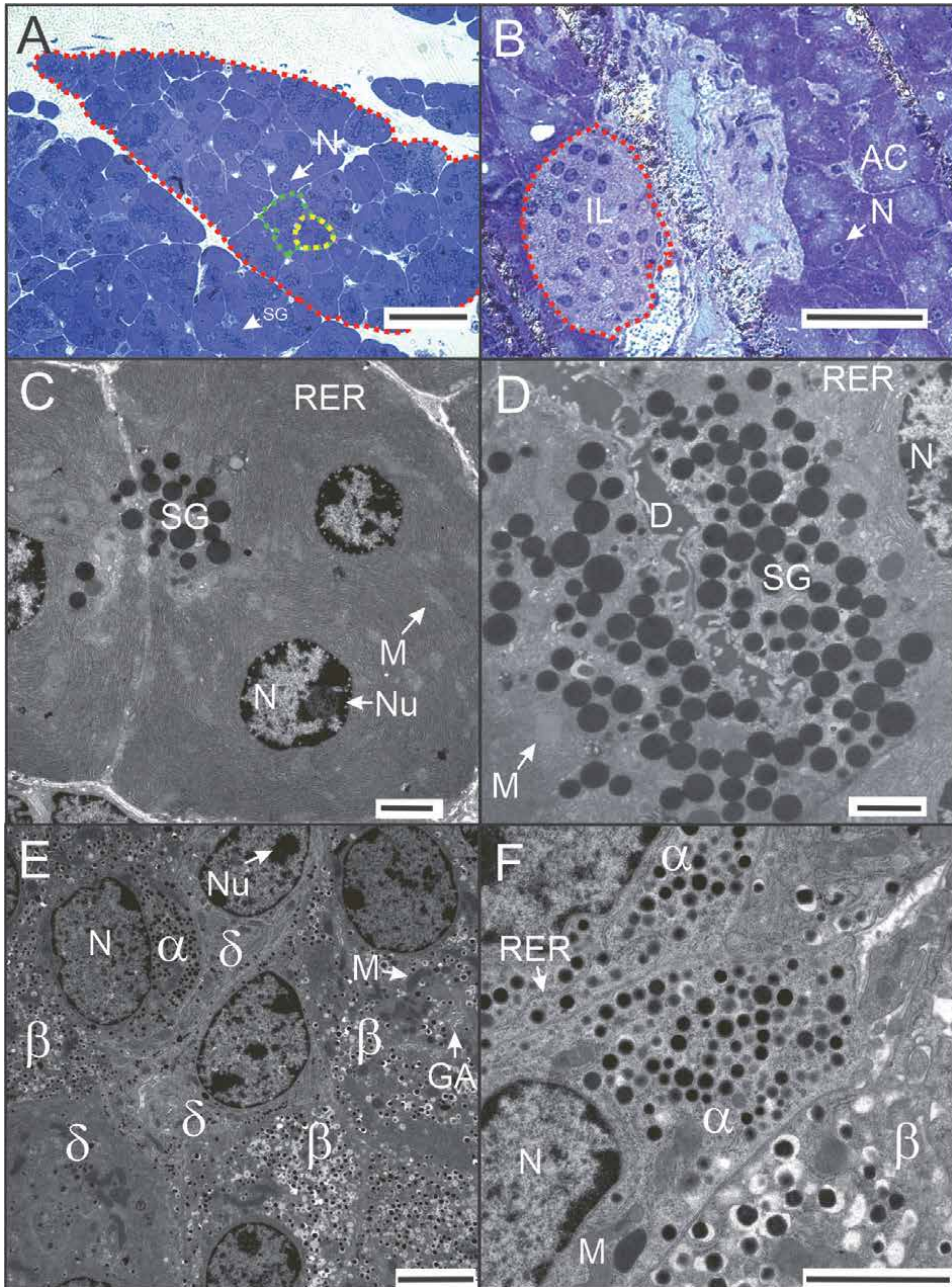


Figure 2. Mice are fed with control diet (CD). (A) and (B) Semithin sections of the pancreas. (A) Exocrine part of the pancreas is composed of acinar cells (one cell marked by the yellow dotted line), organized in acini (one acinus marked by the green dotted line) and lobules (one lobule marked by the red dotted line). (B) Endocrine cells forming a Langerhans islet are seen as brighter stained cells (red dotted line). (C–F) Ultrathin sections of the pancreas. (C) Exocrine cells are easily recognized by their large size, typical shape, by abundant rough endoplasmic reticulum, and secretory granules. (D) The majority of secretory granules are found in the apical part of the cell. (E) and (F) endocrine cells can be distinguished by the fine structure and size of their secretory granules. In all endocrine cells, well-developed rough endoplasmic reticulum, Golgi apparatus, and numerous mitochondria are seen. AC, acinar cell; α , alpha cell; β , beta cell; δ , delta cell; D, duct; IL, islet of Langerhans; GA, Golgi apparatus; M, mitochondrion; N, nucleus; nu, nucleolus; RER, rough endoplasmic reticulum; SG, secretory granules. Scale bars: (A) and (B) 50 μm ; (C) 2.5 μm ; (D) 2 μm ; (E) 5 μm ; (F) 2.5 μm .

5.3.1.1 Normal exocrine and endocrine cell ultrastructure

The majority of tissue consists of pyramid-shaped exocrine cells (**Figure 2A–C**). These cells form clusters or acini around small ducts and are organized in lobes with thin fibrous tissue. The exocrine cells produce inactive digestive enzymes, seen in the cytoplasm packed in secretory vesicles (**Figure 2C and D**), and secrete them into the intercalated ducts which they surround (**Figure 2D**). In each acinus, the exocrine cells are located around the intercalated ducts, with their narrow apical parts oriented to the duct (**Figure 2C and D**). The exocrine cells have a round or oval nucleus (**Figure 2C**), located basally. The most prominent structure of the exocrine cells is the rough endoplasmic reticulum (**Figure 2C**) which is present in all different parts of the cell. Numerous round electron-dense secretory vesicles are seen in the perinuclear and apical cytoplasm (**Figure 2C and D**). The oval mitochondria (**Figure 2C and D**) are found in different parts of the cell.

The endocrine cells are distributed throughout the pancreas (**Figure 2B**) as interlobular positioned clusters of cells termed islets of Langerhans. In the islets of Langerhans (**Figure 2B**) alpha, beta and delta cells can be distinguished (**Figure 2E and F**). They are characterized by numerous secretory vesicles. Glucagon granules of alpha cells are large dense-core vesicles and some of them have a pale halo. The core of the granule is of a similar diameter to insulin granules, but the whole granule is smaller by at least 50% (200 nm vs. 350 nm). Insulin-containing vesicles in beta cells are the largest with large clear peripheral halos. Somatostatin-containing granules of delta cells in mice are the smallest and lozenge-shaped (**Figure 2E and F**) [93–96]. In the cytoplasm of all types of endocrine cells, abundant rough endoplasmic reticulum, Golgi apparatus, and many oval mitochondria are present (**Figure 2E and F**) [97].

5.3.1.2 Ultrastructural changes in WD mice

Comparing the ultrastructure of pancreatic cells in control mice (CD; **Figure 2**) and mice fed the western diet (WD; **Figures 3A and B, 4B, 5E, 7E, and 8D**), we observed many important differences. In the exocrine pancreas of WD mice many necrotic cells (**Figures 3A and 4B**) are present. In some acinar cells, lipid droplets are seen in the

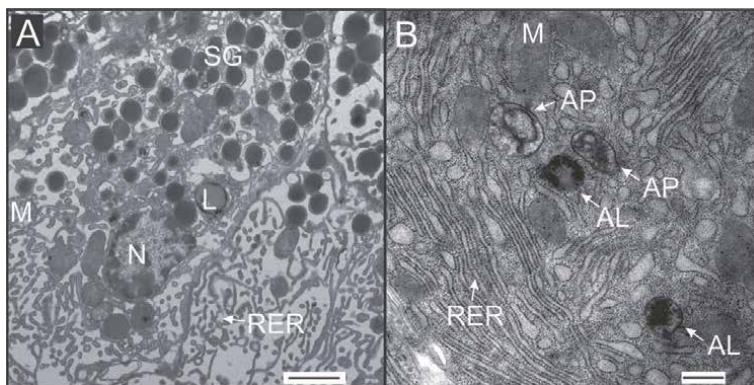


Figure 3. Mice are fed with western diet (WD). (A) and (B) Ultrathin sections of the pancreas. (A) A necrotic acinar cell containing a lipid droplet in the cytoplasm. (B) Autophagosomes and autolysosomes in the cytoplasm of an acinar cell. AL, autolysosome; AP, autophagosome; L, lipid droplet; M, mitochondrion; N, nucleus; SG, secretory granules; RER, rough endoplasmic reticulum. Scale bars: (A) 2 μ m; (B) 500 nm.

cytoplasm (**Figure 3A**). In many cells, numerous autophagic structures, i.e., autophagosomes, autolysosomes (**Figure 3B**), and residual bodies are found. The mitochondria (**Figure 4B**) and rough endoplasmic reticulum (**Figure 5E**) seem to be disorganized, therefore these structures were analyzed in detail.

The structure of the islets of Langerhans in mice fed by WD is non-compact, inhomogeneous, containing more extracellular spaces than in mice fed by CD. There are many necrotic cells in different parts of the islets. In the cytoplasm of endocrine cells, some lipid droplets and many autophagic structures, i.e., autophagosomes, autolysosomes, and residual bodies can be found. Structural differences are also seen in the mitochondria and rough endoplasmic reticulum.

5.3.2 Quantitative analysis of selected cellular structures

Structural characteristics of mitochondria, rough endoplasmic reticulum, zymogen granules, and vacuoles were studied. To accurately analyze various cell compounds, it is necessary to select TEM images taken at the same magnification.

5.3.2.1 Analysis of mitochondria

Since mitochondria are crucial for normal beta cell stimulus-secretion coupling and their ultrastructure is altered during the development of T2DM, we analyzed them in more detail. First, we outlined all the mitochondria in the visual field and calculated the surface area in nm^2 . To quantitatively assess the condition of mitochondria, we measured the following shape descriptors: circularity, roundness, aspect ratio of the best fit ellipse, and solidity using Fiji software (NIH) [98].

Circularity (C) is a shape parameter that can mathematically indicate the degree of similarity to a perfect circle. A value of 1.0 indicates a perfect circle. When the circularity value approaches 0.0, the shape becomes less and less circular. Circularity is defined by the equation

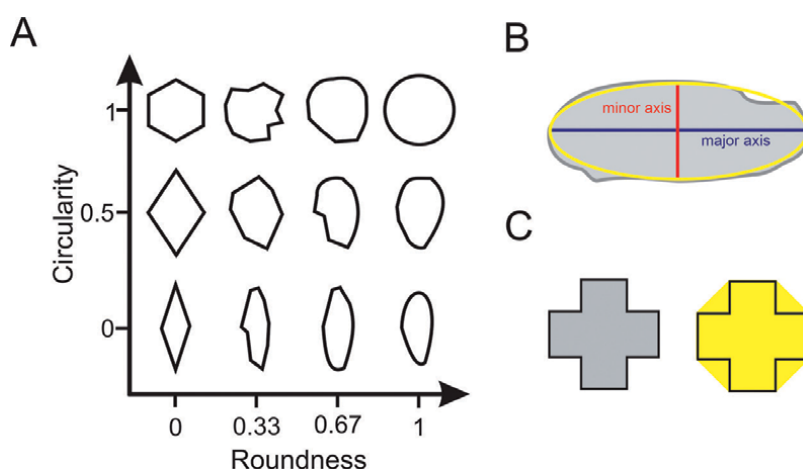


Figure 4. Shape descriptors. (A) Circularity versus roundness. (B) Sketch of a mitochondrion (gray) with an overlay of the best fit ellipse (yellow), the major axis of the best fit ellipse (blue), and the minor axis of the best fit ellipse (red). The major axis is used in determining roundness (Eq. (2)) and aspect ratio (Eq. (3)). (C), the shape area (gray, left) and the convex hull area (yellow, right) are used to determine the solidity.

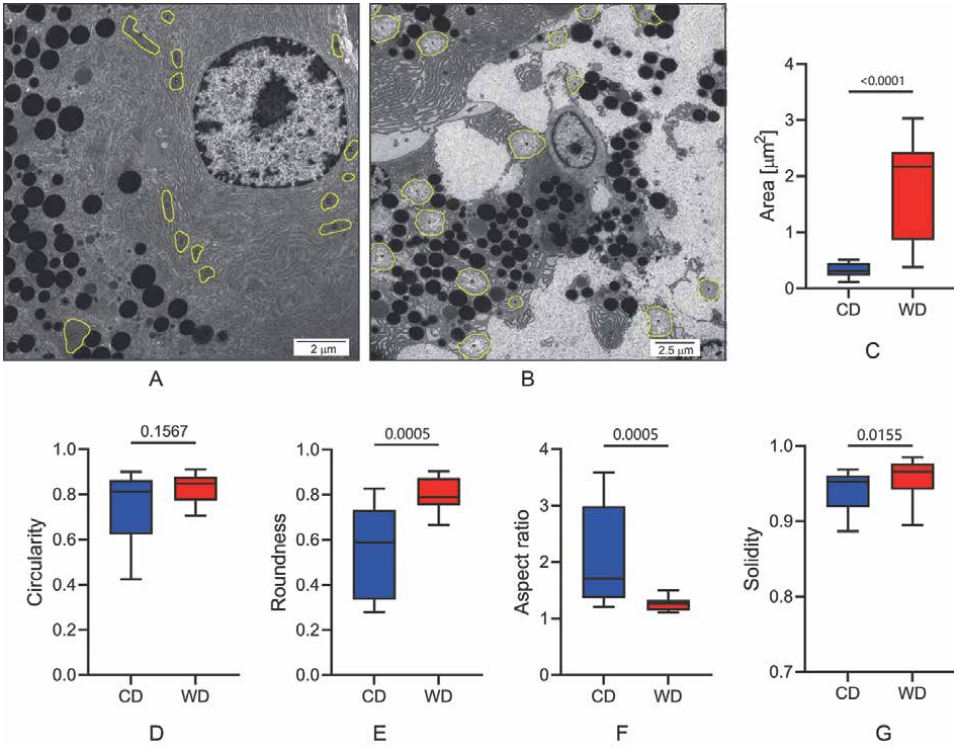


Figure 5. Analysis of the mitochondria from a CD and a WD mouse. Labeled mitochondria in the image of the exocrine pancreas from the (A) CD and (B) WD mouse. Analysis of the (C) surface area, (D) circularity, (E) roundness, (F) aspect ratio and (G) solidity of an image from CD and WD mouse. Data were pooled from the following number of ROIs from the CD/WD image: 14/16. Data were analyzed using the Mann–Whitney U test, *p* values are indicated on graphs.

$$C = 4\pi \frac{\text{Area}}{\text{Perimeter}^2} \quad (1)$$

Roundness (R) on the other hand, characterized by

$$R = \frac{4 \text{Area}}{\pi \text{major axis}^2} \quad (2)$$

is similar to circularity, but it is insensitive to irregular borders along the perimeter of the mitochondria and takes into account the major axis of the best fit ellipse. For an illustrative explanation of the differences between circularity and roundness, see **Figure 6A**.

From the best fit ellipse fit to each mitochondrion, the major and minor axes were determined, and the aspect ratio (AR) was calculated by the following equation:

$$AR = \frac{\text{major axis}}{\text{minor axis}} \quad (3)$$

AR measures the ratio of an object's height to its width (**Figure 6B**). Therefore, the aspect ratio is equal to one for a perfect circle and increases with an increase in deformation.

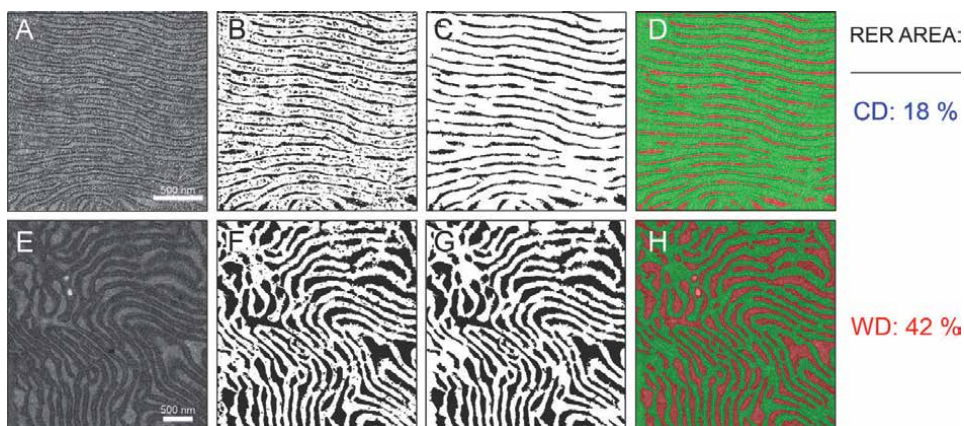


Figure 6. Quantitative analysis of the RER. Representative TEM images from a CD (A) and a WD (E) mouse. The quantification pipeline involves segmentation (B and F), a binary mask depicting RER cisternae in black and cytosol in white), followed by RER determination using particle analysis on the segmented image (C and G). Overlay of the binary masks on the TEM images (D and H), RER cisternae in red, and cytosol in green). Exemplary percentages of the area covered by the RER cisternae are shown in the top right (CD mouse) and bottom right (WD mouse).

At the end, solidity (S) was measured using the same Fiji software. Solidity describes the extent to which shape is convex or concave. Taking the area within the mitochondrion and dividing it by the area enclosed by a convex hull provides information about the solidity of the shape (Figure 6C). Solidity of a perfectly convex structure is 1, but when the structure becomes more concave, the solidity will deviate from 1. The solidity is defined by

$$S = \frac{\text{area}}{\text{convex area}} \quad (4)$$

In the bullet points that follow, we describe each analysis step in detail.

1. Open an image in Fiji.
2. Select the straight line tool from the navigation pane and draw a straight line across the scale bar. The straight line must be precisely the same length as the scale bar.
3. In the “Analyze” menu, select “Set Scale”. When the set scale dialog box opens, enter the value of a scale bar into the “Knowing Distance” box, and in the “Unit of length” box, determine the unit of the scale bar from the image. Click the “OK” button. Now you have set the scale for this particular image.
4. Use the “freehand selection” tool from the toolbar and encircle the first mitochondrion on the image. After the right mouse click within the selected encircled mitochondrion, choose “Add to ROI Manager” from the dialog box.
5. Now encircle the next mitochondrion and click “Add” in the ROI Manager. In the same way, encircle all the mitochondria in the image.
6. In the “Analyze” menu, select “Set measurements” and tick the desired parameters from the dialog box. For the analysis of mitochondria, we selected “Area” and “Shape descriptors”. Click the “OK” button.

7. Now everything is set to analyze all the mitochondria from the image. Select “Measure” in the “Analyze” menu, and a new window with results will pop out. Save the results by selecting “Save as” from the “File” menu of the “Results” window.
8. Now you can analyze the new image in the same way. Remember that the scale must be set again when analyzing the next image.

In **Figure 4** one can observe the results of the above analysis on mitochondria of two representative images of the exocrine pancreas from a CD (**Figure 4A**) and a WD (**Figure 4B**) mouse.

5.3.2.2 Analysis of rough endoplasmic reticulum (RER)

Quantitative analysis of the surface area covered by the RER cisternae on TEM images can provide valuable insight into functional changes in both acinar and endocrine cells. Quantification of the TEM data, in general, involves manual annotation of structures of interest. This approach proved to be an extremely time-consuming process for quantification of the RER data, as the organelle forms a complex and interconnected network of cisternae. To overcome this issue, Trainable Weka Segmentation (TWS, available as Fiji/ImageJ plugin) provides a machine learning tool capable of automated segmentation [99]. A limited number of manual annotations on a sample (training) TEM image produces a classifier that can be applied to the remaining data to segment images automatically. The following pipeline describes steps for RER analysis:

1. Image segmentation: TWS produces a segmented image that reliably separates RER cisternae from the cytosol (**Figure 5B** and **F**, compare with **Figure 5A** and **E**, respectively).
2. Particle analysis: subsequent particle analysis on the segmented image excludes unwanted objects based on the size exclusion criterion that removes small objects that were detected mostly within RER cisternae (**Figure 5C** and **G**). If needed, manually delete unwanted objects.
3. Quantification of data: the resulting binary mask improves partitioning compared to TWS segmentation alone (**Figure 5D** and **H**). The resulting image segments allow for quantification of RER abundance, expressed as the relative area covered by RER cisternae (% RER area). This approach detected a large increase in % RER area in WD mice compared with CD mice in the given cell (42% vs. 18%) (**Figure 5**).

5.3.2.3 Analysis of zymogen granules

Zymogen granules form a reserve pool of digestive enzymes that are secreted from acinar cells after stimulation. The granules are well visible on TEM images and detecting a change in a number of granules per cell, cumulative granule area per cell, or granule size could suggest a functional change in their physiology. Manual counting of granules is the simplest method to quantify zymogen content; however, it relies on an assumption of typical granule size, and it is a relatively time-consuming approach. Alternatively, manual annotation of individual granules would provide data also on the granule size, but it is an even more time-consuming method that would

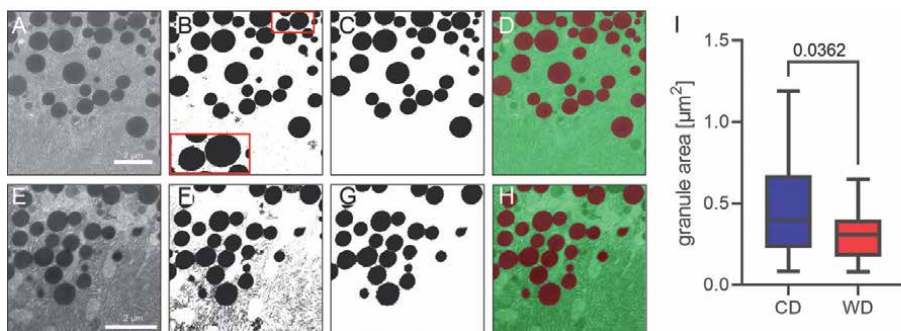


Figure 7. Quantitative analysis of the surface area of zymogen granules. Representative TEM images from CD (A) and WD (E) mice. Image thresholding and watershed separation produce a binary mask (B and F), zymogen granules in black, inset depicts exemplary partitioning of two touching granules). Individual granules are determined using particle analysis on the segmented images (C and G). Panels D and H depict an overlay of the granules on the grayscale TEM image (vesicles in red). Quantification of the granule cross-section area shown in the panel I for a given cell from the CD and the WD mouse. Data were pooled from the following number of ROIs from the CD/WD image: 35/27. Data were analyzed using the Mann–Whitney U test, p values are indicated on graphs.

effectively hamper analysis or limit it to a few cells only. To at least partially automate the quantification, we took advantage of the fact that zymogen granules have typical properties: (i) granules are spherical structures, and (ii) they appear electron-dense (i.e. dark) on TEM images (**Figure 7A** and **E**).

The following brief instructions describe a useful procedure to partition the granules on a TEM image:

1. Image thresholding and separation: Since granules provide good contrast, thresholding the TEM image produces a rough binary mask of granules. Inherently, the thresholding procedure detects two or more granules in close proximity as uniform structures. We can reliably separate the touching granules using the watershed separation method [100]. This method interprets the input image as a topographical surface that is flooded with water, placing water sources in the local topographical minima, and placing dams where water from different sources meets. These dams constitute the watershed (i.e., a border between touching granules, **Figure 7B** inset). The method works best for smooth convex objects that do not overlap too much, and it efficiently separates granules after the initial thresholding (**Figure 7B** and **E**).
2. Particle analysis: Employ particle analysis to remove unwanted small objects in the cytosol that were detected with the thresholding. Limiting the minimal object size effectively removes the background noise (**Figure 7C** and **G**).
3. Quantification of the zymogen granules: The resulting binary mask detects individual granules (see the overlay in the **Figure 7D** and **H**). The segmentation data generally allow for a straightforward counting of granules, assessing the cumulative granule area (case the entire cell is imaged, example data not shown), and granule size. The latter decreased by 22% in the analyzed acinar cell from a WD treated mouse (**Figure 7I**).

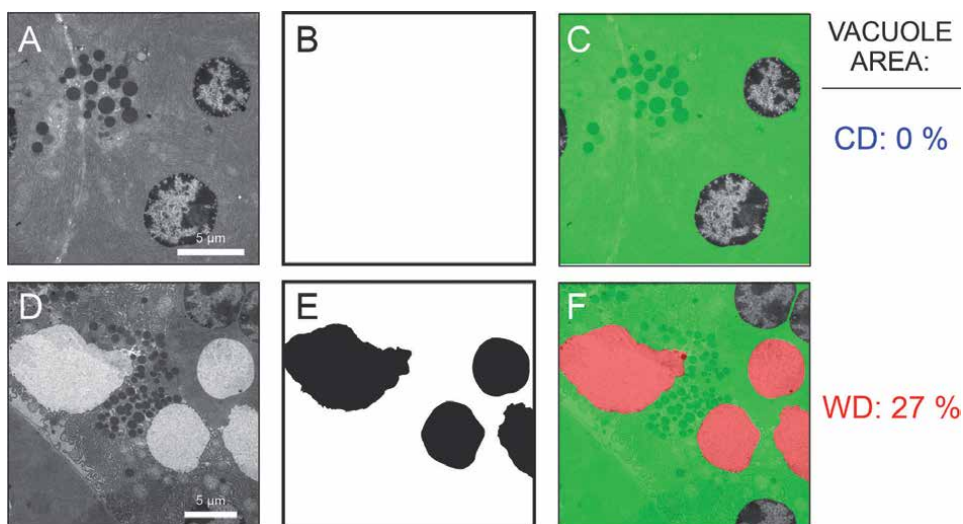


Figure 8.

Quantitative analysis of the vacuoles. Representative TEM images from CD (A) and WD (E) mice. Manual annotation of vacuoles resulted in a binary mask (B and E), vacuoles in black; please note that no vacuoles were present in A. Panels C and D depict an overlay of the vacuole binary mask on the grayscale TEM image (vacuoles in red, cytoplasm in green). Percentages of vacuole cross-section areas are shown on the right for the CD (blue) and the WD (red) mouse.

5.3.2.4 Analysis of vacuoles

Cytoplasmic vacuolization is an ultrastructural change associated with pathological alterations in pancreatic cells [101]. The vacuoles appear electron-lucent (i.e., bright) and inhomogeneous on TEM images, very similar to other structures, and this does not allow the use of image thresholding as a technique to effectively detect vacuoles. Since the number of vacuoles per cell is limited, manual annotation of the structures is feasible.

1. Manual detection of the vacuoles: Use Fiji/ImageJ in combination with the built-in ROI manager to outline the vacuoles, which results in a binary mask of the visible structures on the image (**Figure 8B** demonstrating an empty mask, since no vacuoles were visible on the image, and **8E** shows several vacuoles that were seen within a cell). Overlaying the structures can serve as visual feedback for quality assessment (**Figure 8C** and **F**).

Quantification of the vacuoles: Use data from the above step to measure the relative area covered by the vacuoles by dividing the cumulative vacuole area by the visible cytoplasm surface. Using this approach, we demonstrated that vacuoles are abundant in the acinar cell of WD treated mice (27% vs. 0% in WD vs. CD mice, **Figure 8** right).

6. Conclusions

There are only a handful of studies on pancreatic exocrine and endocrine ultrastructure in mice under diabetogenic conditions. One of the reasons for this relative underrepresentation of such a translationally relevant topic in the literature

may be the rather complex study design typically accompanying work with genetic or dietary mouse models and electron microscopy. An even more important reason may often be a lack of a toolbox to easily, objectively, and reproducibly analyze ultrastructural changes in exocrine and endocrine cells in a quantitative manner. In this chapter, we tried to specifically address this problem by providing the readers with a robust step-by-step approach and detailed instructions on how to quantify changes in the ultrastructure of mitochondria, rough endoplasmic reticulum, and secretory vesicles, as well as the presence of vacuoles, by means of shape descriptors, thresholding, manual selection, and machine-learning supported image segmentation, followed by different quantification steps employed in the open-source Fiji software. With some field-specific modifications, our analyses shall also be useful for many other life scientists.

Acknowledgements

We would like to express our gratitude to colleagues at the Institute of Physiology for their support and to Prof. Gerd Leitinger (Medical University Graz) for critical reading of the manuscript.

Funding

This research was funded by the SLOVENIAN RESEARCH AGENCY, grant number P3-0396, I0-0029, N3-0133, and N3-0170.

Author details

Maša Skelin Klemen^{1*}, Jurij Dolenshek^{1,2}, Ismael Valladolid-Acebes³, Andraž Stožer¹ and Saška Lipovšek^{2,4,5,6}

1 Faculty of Medicine, Institute of Physiology, University of Maribor, Maribor, Slovenia

2 Faculty of Natural Sciences and Mathematics, Department of Biology, University of Maribor, Maribor, Slovenia

3 The Rolf Luft Research Center for Diabetes and Endocrinology, Karolinska Institutet, Stockholm, Sweden


4 Faculty of Medicine, University of Maribor, Maribor, Slovenia

5 Faculty of Chemistry and Chemical Engineering, University of Maribor, Maribor, Slovenia

6 Division of Cell Biology, Histology and Embryology, Gottfried Schatz Research Center for Cell Signaling, Metabolism and Aging, Medical University of Graz, Graz, Austria

*Address all correspondence to: masa.skelin@um.si

IntechOpen

© 2022 The Author(s). Licensee IntechOpen. This chapter is distributed under the terms of the Creative Commons Attribution License (<http://creativecommons.org/licenses/by/3.0>), which permits unrestricted use, distribution, and reproduction in any medium, provided the original work is properly cited. 

References

- [1] IDFIDF Diabetes Atlas. International Diabetes Federation. 2021
- [2] Pørksen N. The in vivo regulation of pulsatile insulin secretion. *Diabetologia*. 2002;**45**(1):3-20
- [3] Simon C, Brandenberger G. Ultradian oscillations of insulin secretion in humans. *Diabetes*. 2002;**51**(suppl_1):S258-S261
- [4] Simon C. Ultradian pulsatility of plasma glucose and insulin secretion rate: circadian and sleep modulation. *Hormone Research in Paediatrics*. 1998;**49**(3-4):185-190
- [5] Stozer A, Hojs R, Dolensek J. Beta cell functional adaptation and dysfunction in insulin resistance and the role of chronic kidney disease. *Nephron*. 2019;**143**(1):33-37
- [6] Lu H et al. Molecular and metabolic evidence for mitochondrial defects associated with beta-cell dysfunction in a mouse model of type 2 diabetes. *Diabetes*. 2010;**59**(2):448-459
- [7] Irls E et al. Enhanced glucose-induced intracellular signaling promotes insulin hypersecretion: Pancreatic beta-cell functional adaptations in a model of genetic obesity and prediabetes. *Molecular and Cellular Endocrinology*. 2015;**404**:46-55
- [8] Gonzalez A et al. Insulin hypersecretion in islets from diet-induced hyperinsulinemic obese female mice is associated with several functional adaptations in individual beta-cells. *Endocrinology*. 2013;**154**(10):3515-3524
- [9] Corezola do Amaral ME et al. Caloric restriction recovers impaired β -cell- β -cell gap junction coupling, calcium oscillation coordination, and insulin secretion in prediabetic mice. *American Journal of Physiology-Endocrinology and Metabolism*. 2020;**319**(4):E709-E720
- [10] Rajab BS et al. Differential remodelling of mitochondrial subpopulations and mitochondrial dysfunction are a feature of early stage diabetes. *Scientific Reports*. 2022;**12**(1):978
- [11] Arrojo EDR, Roy B, MacDonald PE. Molecular and functional profiling of human islets: From heterogeneity to human phenotypes. *Diabetologia*. 2020;**63**(10):2095-2101
- [12] Arrojo EDR. Probing beta-cell biology in space and time. *Diabetes*. 2021;**70**(10):2163-2173
- [13] Titova AA et al. Early ultra- and microstructural alterations in rat pancreas in alloxan-induced diabetes mellitus. *Ultrastructural Pathology*. 2020;**44**(1):61-70
- [14] Lacy PE. Electron microscopic identification of different cell types in the islets of Langerhans of the Guinea pig, rat, rabbit and dog. *The Anatomical Record*. 1957;**128**(2):255-267
- [15] Palade GE. The endoplasmic reticulum. *The Journal of Biophysical and Biochemical Cytology*. 1956;**2**(Suppl. 4):85-98
- [16] Danielsson A et al. The human pancreas proteome defined by transcriptomics and antibody-based profiling. *PLoS One*. 2014;**9**(12):e115421
- [17] Bockman DE. Anatomy of the pancreas. In: Go VLW, editor. *The Pancreas: Biology, Pathobiology, and Disease*. Norris, MT: Raven Press; 1993. pp. 1-8

- [18] In't Veld P, Marichal M. Microscopic anatomy of the human islet of langerhans. In: Islam MS, editor. *The Islets of Langerhans*. Netherlands, Dordrecht: Springer; 2010. pp. 1-19
- [19] Liu XY et al. Pancreas transplantation in the mouse. *Hepatobiliary & Pancreatic Diseases International*. 2010;**9**(3):254-258
- [20] Yaginuma N et al. The microvasculature of the human pancreas and its relation to Langerhans islets and lobules. *Pathology, Research and Practice*. 1986;**181**(1):77-84
- [21] Motta PM et al. Histology of the exocrine pancreas. *Microscopy Research and Technique*. 1997;**37**(5-6):384-398
- [22] Saito K, Iwama N, Takahashi T. Morphometrical analysis on topographical difference in size distribution, number and volume of islets in the human pancreas. *The Tohoku Journal of Experimental Medicine*. 1978;**124**(2):177-186
- [23] Rahier J, Wallon J, Henquin JC. Cell populations in the endocrine pancreas of human neonates and infants. *Diabetologia*. 1981;**20**(5):540-546
- [24] Steiner DJ et al. Pancreatic islet plasticity: Interspecies comparison of islet architecture and composition. *Islets*. 2010;**2**(3):135-145
- [25] Cabrera O et al. The unique cytoarchitecture of human pancreatic islets has implications for islet cell function. *Proceedings of the National Academy of Sciences of the United States of America*. 2006;**103**(7):2334-2339
- [26] Arrojo e Drigo R et al. New insights into the architecture of the islet of Langerhans: A focused cross-species assessment. *Diabetologia*. 2015;**58**(10):2218-2228
- [27] Dolensek J, Rupnik MS, Stozar A. Structural similarities and differences between the human and the mouse pancreas. *Islets*. 2015;**7**(1):e1024405
- [28] Skelin Klemen M et al. The triggering pathway to insulin secretion: Functional similarities and differences between the human and the mouse β cells and their translational relevance. *Islets*. 2017;**9**(6):109-139
- [29] Dolenšek J. *Pancreas Physiology*. London: IntechOpen; 2017
- [30] Hegyi P et al. Pancreatic ductal bicarbonate secretion: Challenge of the acinar acid load. *Frontiers in Physiology*. 2011;**2**:36
- [31] Petersen OH. Physiology of acinar cell secretion. *The Pancreas*. 2008;**26**:69-77
- [32] Argent BE et al. Chapter 51 - Cell Physiology of Pancreatic Ducts, in *Physiology of the Gastrointestinal Tract (Fifth Edition)*, L.R. Johnson, et al., Editors. Boston: Academic Press; 2012. pp. 1399-1423
- [33] Tokarz VL, MacDonald PE, Klip A. The cell biology of systemic insulin function. *The Journal of Cell Biology*. 2018;**217**(7):2273-2289
- [34] Czech MP. Insulin action and resistance in obesity and type 2 diabetes. *Nature Medicine*. 2017;**23**(7):804-814
- [35] Lewis GF et al. Direct and indirect control of hepatic glucose production by insulin. *Cell Metabolism*. 2021;**33**(4):709-720
- [36] Jiang G, Zhang BB. Glucagon and regulation of glucose metabolism. *American Journal of Physiology. Endocrinology and Metabolism*. 2003;**284**(4):E671-E678

- [37] Ramnanan CJ et al. Physiologic action of glucagon on liver glucose metabolism. *Diabetes, Obesity and Metabolism*;13:118-125
- [38] Himsworth HP. Insulin deficiency and insulin inefficiency. *British Medical Journal*;1(4139):719
- [39] Di Ciaula A, Portincasa P. Fat, epigenome and pancreatic diseases. Interplay and common pathways from a toxic and obesogenic environment. *European Journal of Internal Medicine*. 2014;25(10):865-873
- [40] OECD. *The Heavy Burden of Obesity*. Paris, France: OECD; 2019
- [41] Gastaldelli A et al. Relationship between hepatic/visceral fat and hepatic insulin resistance in nondiabetic and type 2 diabetic subjects. *Gastroenterology*. 2007;133(2):496-506
- [42] Goossens GH. The role of adipose tissue dysfunction in the pathogenesis of obesity-related insulin resistance. *Physiology & Behavior*. 2008;94(2):206-218
- [43] Despres JP, Lemieux I. Abdominal obesity and metabolic syndrome. *Nature*. 2006;444(7121):881-887
- [44] Della Corte C et al. Nonalcoholic fatty pancreas disease and nonalcoholic fatty liver disease: More than ectopic fat. *Clinical Endocrinology*. 2015;83(5):656-662
- [45] Petersen KF et al. Reversal of nonalcoholic hepatic steatosis, hepatic insulin resistance, and hyperglycemia by moderate weight reduction in patients with type 2 diabetes. *Diabetes*. 2005;54(3):603-608
- [46] Taylor R et al. Remission of human type 2 diabetes requires decrease in liver and pancreas fat content but is dependent upon capacity for β cell recovery. *Cell Metabolism*. 2018;28(4):547-556
- [47] Acharya C, Navina S, Singh VP. Role of pancreatic fat in the outcomes of pancreatitis. *Pancreatology*. 2014;14(5):403-408
- [48] Navina S et al. Lipotoxicity causes multisystem organ failure and exacerbates acute pancreatitis in obesity. *Science Translational Medicine*. 2011;3(107):107ra110
- [49] Keun Young S et al. Influence of obesity on the severity and clinical outcome of acute pancreatitis. *Gut and Liver*. 2011;5(3):335-339
- [50] Alempijevic T et al. Non-alcoholic fatty pancreas disease. *Postgraduate Medical Journal*. 2017;93(1098):226-230
- [51] Mathur A et al. Nonalcoholic fatty pancreas disease. *HPB*. 2007;9(4):312-318
- [52] Schaefer JH. The normal weight of the pancreas in the adult human being: A biometric study. *The Anatomical Record*. 1926;32(2):119-132
- [53] Ogilvie RF. The islands of langerhans in 19 cases of obesity. *The Journal of Pathology and Bacteriology*. 1933;37(3):473-481
- [54] Taylor R. Remission of type 2 diabetes by weight loss in a non-white population. *The lancet. Diabetes & Endocrinology*. 2020;8(6):458-459
- [55] Riddle MA-O et al. Consensus report: definition and interpretation of remission in type 2 diabetes. *The Journal of Clinical Endocrinology & Metabolism*;107(1):1-9. DOI: 10.2337/dci21-0034
- [56] Petrov MS, Taylor R. Intra-pancreatic fat deposition: bringing hidden fat to the fore. *Nature Reviews Gastroenterology & Hepatology*. 2021;19:1-16

- [57] Taylor R, Holman RR. Normal weight individuals who develop type 2 diabetes: The personal fat threshold. *Clinical Science*. 2015;**128**(7):405-410
- [58] Cerasi E, Ktorza A. [anatomical and functional plasticity of pancreatic beta-cells and type 2 diabetes]. *Medical Science (Paris)*. 2007;**23**(10):885-894
- [59] Weiss R et al. Beta-cell function across the spectrum of glucose tolerance in obese youth. *Diabetes*. 2005;**54**(6):1735-1743
- [60] White MG, Shaw JA, Taylor RA-O. Type 2 diabetes: the pathologic basis of reversible β -cell dysfunction. *Diabetes Care*. 2016;**39**(11):2080-2088
- [61] Paschen M et al. Diet-induced β -cell insulin resistance results in reversible loss of functional β -cell mass. *The FASEB Journal*. 2019;**33**(1):204-218
- [62] Saito K, Fau-Takahashi T, et al. Islet morphometry in the diabetic pancreas of man. *The Tohoku Journal of Experimental Medicine*. 1978;**125**(2):185-197
- [63] Butler AE et al. Beta-cell deficit in obese type 2 diabetes, a minor role of beta-cell dedifferentiation and degranulation. *The Journal of Clinical Endocrinology and Metabolism*. 2016;**101**(2):523-532
- [64] Marchetti P et al. The endoplasmic reticulum in pancreatic beta cells of type 2 diabetes patients. *Diabetologia*. 2007;**50**(12):2486-2494
- [65] Accili D et al. When beta-cells fail: Lessons from dedifferentiation. *Diabetes, Obesity & Metabolism*. 2016;**18**(Suppl. 1): 117-122
- [66] Hunter CS, Stein RW. Evidence for loss in identity, De-differentiation, and trans-differentiation of islet beta-cells in type 2 diabetes. *Frontiers in Genetics*. 2017;**8**:35
- [67] Talchai C et al. Pancreatic beta cell dedifferentiation as a mechanism of diabetic beta cell failure. *Cell*. 2012;**150**(6):1223-1234
- [68] Cinti F et al. Evidence of beta-cell dedifferentiation in human type 2 diabetes. *The Journal of Clinical Endocrinology and Metabolism*. 2016;**101**(3):1044-1054
- [69] Ajoolabady A et al. ER stress in obesity pathogenesis and management. *Trends in Pharmacological Sciences*. 2022;**43**(2):97-109
- [70] Almanza A et al. Endoplasmic reticulum stress signalling – From basic mechanisms to clinical applications. *The FEBS Journal*. 2019;**286**(2):241-278
- [71] Ariyasu D, Yoshida H, Hasegawa Y. Endoplasmic reticulum (ER) stress and endocrine disorders. *International Journal of Molecular Sciences*. 2017;**18**(2)
- [72] Korc M et al. Pancreatic islet-acinar cell interaction: Amylase messenger RNA levels are determined by insulin. *Science*. 1981;**213**(4505):351-353
- [73] Williams JA, Goldfine ID. The insulin-pancreatic acinar axis. *Diabetes*. 1985;**34**(10):980-986
- [74] Wiederkehr A, Wollheim CB. Minireview: Implication of mitochondria in insulin secretion and action. *Endocrinology*. 2006;**147**(6):2643-2649
- [75] Maassen JA, Janssen GM, Hart LM. Molecular mechanisms of mitochondrial diabetes (MIDD). *Annals of Medicine*. 2005;**37**(3):213-221
- [76] Ma Z et al. Diabetes reduces beta-cell mitochondria and induces distinct

- morphological abnormalities, which are reproducible by high glucose in vitro with attendant dysfunction. *Islets*. 2012;**4**(3):233-242
- [77] Anello M et al. Functional and morphological alterations of mitochondria in pancreatic beta cells from type 2 diabetic patients. *Diabetologia*. 2005;**48**(2):282-289
- [78] Masini M et al. Ultrastructural alterations of pancreatic beta cells in human diabetes mellitus. *Diabetes/ Metabolism Research and Reviews*. 2017;**33**(6):e2894
- [79] Folli F et al. Pancreatic islet of Langerhans' cytoarchitecture and ultrastructure in normal glucose tolerance and in type 2 diabetes mellitus. *Diabetes, Obesity & Metabolism*. 2018;**20**(Suppl. 2):137-144
- [80] Jung HS, Lee MS. Role of autophagy in diabetes and mitochondria. *Annals of the New York Academy of Sciences*. 2010;**1201**:79-83
- [81] Jung HS, Lee MS. Macroautophagy in homeostasis of pancreatic beta-cell. *Autophagy*. 2009;**5**(2):241-243
- [82] Masini M et al. Autophagy in human type 2 diabetes pancreatic beta cells. *Diabetologia*. 2009;**52**(6):1083-1086
- [83] Dimmer KS, Scorrano L. (De) constructing mitochondria: What for? *Physiology (Bethesda)*. 2006;**21**:233-241
- [84] Joost H-G, Al-Hasani H, Schurmann A. Animal models in diabetes research. In: *Methods in Molecular Biology*. xi ed. New York: Humana Press; 2012. p. 325
- [85] Fellmann L et al. Murine models for pharmacological studies of the metabolic syndrome. *Pharmacology & Therapeutics*. 2013;**137**(3):331-340
- [86] Gill-Randall RJ et al. Is human type 2 diabetes maternally inherited? Insights from an animal model. *Diabetic Medicine*. 2004;**21**(7):759-762
- [87] Kaplan JR, Wagner JD. Type 2 diabetes - an introduction to the development and use of animal models. *ILAR Journal*. 2006;**47**(3):181-185
- [88] King AJF. The use of animal models in diabetes research. *British Journal of Pharmacology*. 2012;**166**(3):877-894
- [89] Winzell MS, Ahrén B. The high-fat diet-fed mouse: A model for studying mechanisms and treatment of impaired glucose tolerance and type 2 diabetes. *Diabetes*. 2004;**53**(suppl 3):S215-S219
- [90] Stožer A et al. Confocal laser scanning microscopy of calcium dynamics in acute mouse pancreatic tissue slices. *JoVE*. 2021;**170**:e62293
- [91] Stožer A, Dolenšek J, Rupnik MS. Glucose-stimulated calcium dynamics in islets of Langerhans in acute mouse pancreas tissue slices. *PLoS One*. 2013;**8**(1):e54638
- [92] Speier S, Rupnik M. A novel approach to in situ characterization of pancreatic β -cells. *Pflügers Archiv European Journal of Physiology*. 2003;**446**(5):553-558
- [93] Brereton MF et al. Alpha-, delta- and PP-cells: Are they the architectural cornerstones of islet structure and co-ordination? *Journal of Histochemistry & Cytochemistry*. 2015;**63**(8):575-591
- [94] Pfeifer CR et al. Quantitative analysis of mouse pancreatic islet architecture by serial block-face SEM. *Journal of Structural Biology*. 2015;**189**(1):44-52
- [95] Leiter EH, Fau-Gapp DA, et al. Ultrastructural and morphometric studies

of delta cells in pancreatic islets from C57BL/Ks diabetes mice. *Diabetologia*. 1979;17(5):297-309

[96] Lipovšek S et al. Rab3a ablation related changes in morphology of secretory vesicles in major endocrine pancreatic cells, pituitary melanotroph cells and adrenal gland chromaffin cells in mice. *General and Comparative Endocrinology*. 2013;185:67-79

[97] Zeidler A et al. Assessment of pancreatic islet-cell population in the hyperglycemic athymic nude mouse: immunohistochemical, ultrastructural, and hormonal studies. *Pancreas*. 1989;4(2):153-160

[98] Schindelin J et al. Fiji: An open-source platform for biological-image analysis. *Nature Methods*. 2012;9(7):676-682

[99] Arganda-Carreras I et al. Trainable Weka segmentation: A machine learning tool for microscopy pixel classification. *Bioinformatics*. 2017;33(15):2424-2426

[100] Legland D, Arganda-Carreras I, Andrey P. MorphoLibJ: Integrated library and plugins for mathematical morphology with ImageJ. *Bioinformatics*. 2016;32(22):3532-3534

[101] Abdul-Hamid M, Moustafa N. Protective effect of curcumin on histopathology and ultrastructure of pancreas in the alloxan treated rats for induction of diabetes. *The Journal of Basic & Applied Zoology*. 2013;66(4):169-179

Laser-Induced Breakdown Spectroscopy and Microscopy Study of Human Dental Tissues

Muhammad Mustafa, Anwar Latif and Majid Jehangir

Abstract

Laser-induced breakdown spectroscopy (LIBS) analysis of human dental tissues: enamel and dentine, performed by utilizing Nd: YAG laser ($\lambda=1064\text{ nm}$, $\tau=6\text{ ns}$, $E=50\text{ mJ}$) to investigate threshold ablation of laser energy density. Quantitative results based on the experiment provide us with threshold ablation value of laser energy density for calcium (Ca) ablation in enamel and dentine tissues. The computed threshold laser energy density for Ca ablation in dentin tissue is 0.38 J/cm^2 , which is significantly lower than the threshold in the enamel, which is 1.41 J/cm^2 . Scanning electron microscopic (SEM) examination of dental tissues determines that the dentin surface contains pores, voids, and bubbles that make it easy to ablate at low laser energy density, while enamel has a closely packed smear layer structure that is difficult to ablate, requiring high energy densities. These findings are helpful in the field of laser dentistry, where lasers are widely used for dental treatment.

Keywords: electron microscopy, laser-induced breakdown spectroscopy, Nd: YAG laser, dental tissues, energy density

1. Introduction

Lasers have been utilized as a supplementary treatment in dentistry since 1964. They have experienced significant advancements in a variety of dental applications. Nd: YAG lasers are mainly used in dentistry, including soft and hard tissue surgery, cavity preparation in tooth enamel and dentine, detection of tooth decay, prevention of tooth decay by modifying the crystalline structure of enamel, and tooth whitening [1–5].

Lasers to ablate tissues may cause cracks, fractures, fissures, irradiation roughness, surface irregularities, and the removal of smeared layers [6]. The risks of the laser can be avoided by selecting optimized laser parameters according to the chemical composition of the irradiated tissues [7, 8]. It is significant to determine the minimum value of laser energy density that is required to take out an atom of material of the same element, known as threshold ablation. To optimize the laser energy density and energy of the laser, it is required to calculate the threshold ablation of energy density for calcium (the most commonly found mineral in dental tissues) in enamel and dentine that can be precisely achieved by laser-induced breakdown spectroscopy [9, 10].

LIBS is an atomic emission spectroscopic technique. It is also known as “laser-induced plasma spectroscopy” (LIPS) because elements and atomic species are

quantified through spectrometric analysis of laser-induced plasmas. The LIBS spectroscopy technique uses a high-intensity laser capable of ablating small amounts of material, thereby creating a short-duration plasma [11]. The formed plasma contains the excited atoms, molecules, and ions that appeared in the target. As the plasma cools, the atoms, ions, and molecules lose energy due to the emission of light photons that carry certain wavelengths [12]. Thus, spectroscopic characterization of the plasma light will reveal the elements present in the target. The identification of many elemental lines, including both the wavelength and the intensity within the emission spectrum, will form a unique spectral fingerprint of the target, such as calcium [13–16].

Scanning electron microscopy (SEM) is a versatile technique to investigate surface topography, structural morphology, composition, the orientation of grains, crystallography, etc. of dental tissues by achieving its three-dimensional (3D) image with high quality and spatial resolution [17]. In SEM, micro to nanostructure analysis can be examined by focusing a finely collimated electron beam on the dental slices. Due to interaction between incident electrons and the slices, various types of signals may emit from irradiated tissues such as secondary electrons (SE), backscattered electrons (BSE), Auger electrons, continuous and characteristics X-rays, and other photons of different energies [18]. These signals are detected by suitable detectors available in SEM such as Everhart–Thornley detector (ETD) is used to detect SE [19], BSE using a retractable circular BSE detector (CBS) [20], and X-rays signal by energy dispersive spectrometer (EDS) detector [21]. 3D highly magnifying image form on the computer by connecting the signal detectors through the optical fiber.

In the present research work, we have calculated the threshold ablation value of laser energy density for calcium found in human dental tissues such as enamel and dentine by employing LIBS. To investigate the significant difference in threshold ablation for Ca in dental tissues SEM analyses are conducted to examine the surface and structural morphology of these tissues.

2. Sample preparations and methods

Two identical samples of sound extracted human molar teeth were collected from a Dental clinic, Medical & Dental Curatives, and Implant Center, approved by the institute of public health, the government of Punjab, Pakistan. The molars were immersed in saline solution to avoid dryness. Teeth were sectioned into their longitudinal axis using a diamond disk (model HOR, Horico, Germany) to produce two subsamples of dental tissues enamel and dentin of each $5 \times 5 \times 2$ mm thickness. For experimental purposes, enamel-dentine surfaces were polished using #600 and #1200 silicon carbide sandpapers.

Sample 2 slices were coated with an electrically conductive layer of copper for SEM observation.

Figure 1 displays a schematic diagram of the LIBS experimental setup used to record the LIBS spectra of dental tissues in a vacuum. For experimentation J200 Tandem LA (Applied Spectra, Inc. USA) LIBS unit is used, in which pre-installed Q-switched Nd:YAG (1064 nm, 6 ns, 50 mJ) Quanta Ray Pro-230-10 Spectra physics, USA, with the flattop beam profile, the spot diameter of 0.09 cm, and energy density range of 1–15 J/cm² was projected as the source of irradiation. The sample chamber in J200 is a box equipped with an adjustable sample stage. The slices of sample 1: enamel and dentine, are sequentially placed in the sample chamber and irradiated by the Nd:YAG laser. An infrared (IR) lens of a focal length of 75 cm focuses the laser

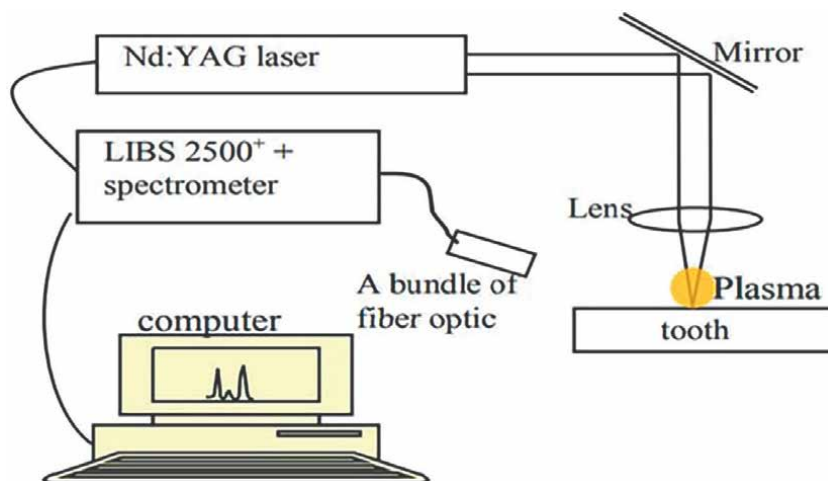


Figure 1.
Represents a schematic diagram of the LIBS experimental setup for dental tissue analysis.

beam on slices to generate plasma. The emission of light photons from the plasma is collected by a lens adjusted at an angle of about 45° to the laser beam axis and fed to the spectrometer. The Scanning Czerny-Turner type spectrometers are continuously operating to capture and read data. It has a response range of wavelength (190–900) nm with a spectral resolution of 0.2 nm. At various laser energy densities of 1 J/cm^2 to 15 J/cm^2 , maximum emission intensities of spectra are displayed by connecting spectrometers to a linear charge-coupled device (CCD) camera.

FEI Nova 450 Scanning electron microscope (SEM) was used for micro to nano-structural analysis of dental tissues. Copper-coated sample 2 slices are placed into a $110 \times 110 \text{ mm}/150 \times 150 \text{ mm}$ stage that can be positioned in five directions: x, y, z, rotation, and tilt. These movements are motorized and controlled by xT microscope control software. The immersion mode is selected from the xT microscope-driven user interface drop-down menu. The immersion lens is activated, and the lens detector (TLD) in secondary electron operation amplifies images of specimens over $500,000\times$, resulting in ultra-high-resolution imaging in digital format.

3. Statistical analysis

Axiom laser ablation (LA) is an operating software in laser-induced breakdown spectroscopy. A chemo-metric technique in LA is a statistical mechanism for the identification of elements to quantify them. It also integrates ICP-MS data management and analysis tools, which are essential for generating precise quantitative solutions and highly accurate statistics. It is employed to choose isotopes of interest and compare their temporally resolved ICP-MS outcomes. Time-resolved signal device is used to study the time-resolved behavior of elements displayed on the graph at various time intervals. Time-resolved ICP-MS rapidly smooths the data and TRSD (Temporal Relative Standard Deviation) statistics are easily obtained. Graphical Development Tool (GDT) chemo-metric software from LIBS Spectra allows us to distinguish LIBS spectra and visualize the differences. The calcium lines that appeared in the LIBS spectra were chosen as the ablation indicators. They appeared at a variety of wavelengths. Their peak areas were computed and plotted according to the laser energy densities. The

relationship between peak areas and energy densities was then represented via data fitting. The ablation thresholds were determined based on the curve fitting. The calculations and statistical analysis were performed using Origin (8.5) software. The measurements from SEM micrographs were taken by ImageJ (1.53 k) software.

4. Results

The relationship between the peak areas of calcium lines and full-width half-maximum is given below [22]:

$$A = \frac{h \times FWHM}{2.35 \times 0.3989} \quad (1)$$

Here, A represents the peak area, h is the amplitude of the peak, and FWHM is the full-width half-maximum. Eq. (1) provides a simple way of peak area calculation by measuring peak height and a full-width half-maximum of spectra. Areas of peak to corresponding energy densities are used to calculate the threshold ablation of calcium in enamel and dentin. In this study, Ca peaks are the peaks of interest that directly reflect the concentration of Ca within the dental tissues.

In the J200 LIBS unit the Nd: YAG laser (1064 nm, 6 nm, 50 mJ) focused on tooth sample enamel and dentin that formed plasma. The emission of photons from plasma

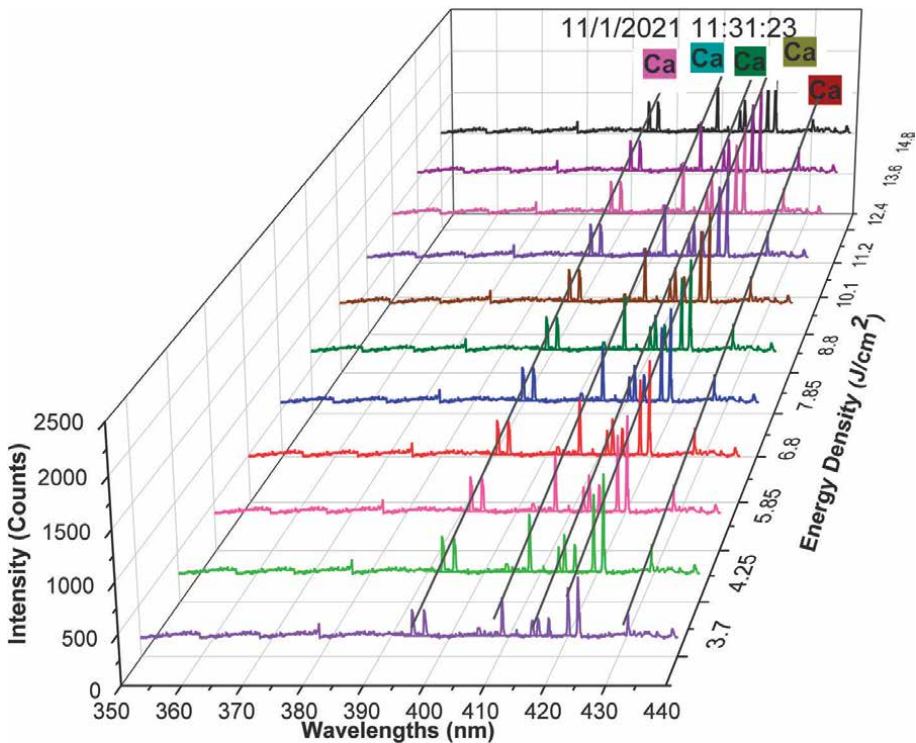


Figure 2. Spectra obtained at different energy densities for enamel at the 14th shot.

is captured by the spectrometers and then displayed on computer intensity spectra as a function of wavelength, as shown in **Figures 2** and **3** respectively. The area under the curves was calculated using the built-in Axiom laser ablation software for laser-induced breakdown spectroscopy.

4.1 Enamel spectra obtained by J200 tandem LA-LIBS instrument using axiom LA system software at various laser energy densities

Figure 2 represents spectra of enamel tissue for different energy density ranges 3.7 J/cm^2 to 14.8 J/cm^2 and optimized number of pulses (14). The emission of the discrete line from enamel tissue is identified as a calcium element, and they have three main features: wavelength, intensity, and shape. The calcium element in tissues has different energy levels and the transition between these energy levels determines the wavelengths of emitted spectral lines.

Table 1 displays the data for 11 enamel spectra (in **Figure 2**) at different wavelengths and their corresponding peak areas. The maximum peak area was 32 counts/nm at 14.8 J/cm^2 while a minimum of 5 counts/nm at 3.7 J/cm^2 and 4.25 J/cm^2 was attained.

4.2 Dentine spectra obtained by J200 tandem LA-LIBS instrument using axiom LA system software at various laser energy densities

Figure 3 exhibits the spectra of dentine tissue for the laser energy densities 2.4 J/cm^2 to 14.8 J/cm^2 and the optimized number of pulses 4. Ca metals were identified as the

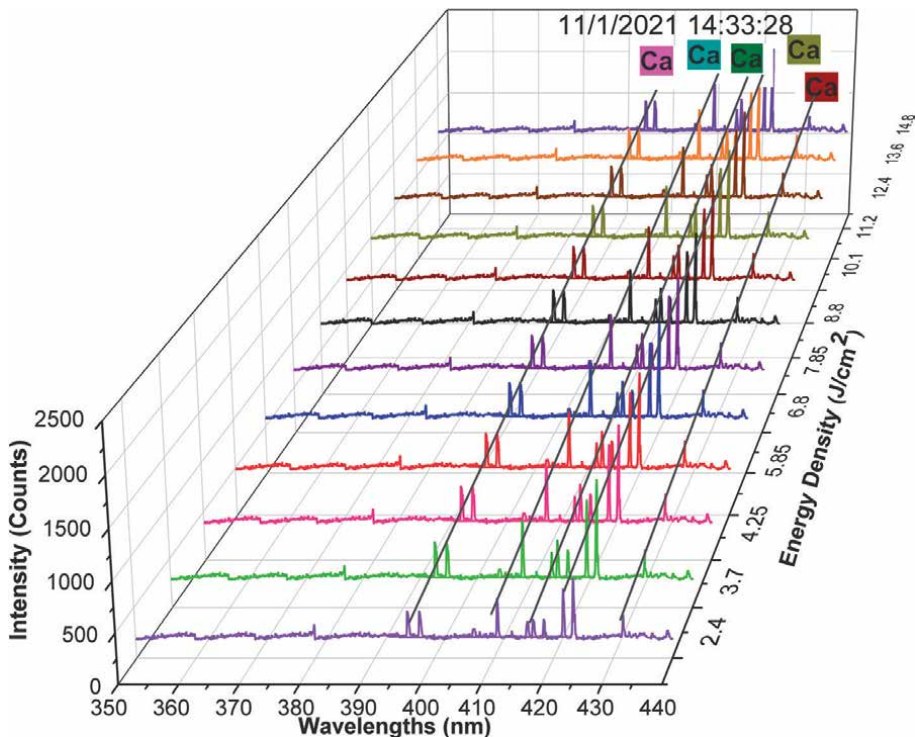


Figure 3.
Spectra at different energy densities for dentin at the 4th shot.

discrete lines emitted from dentine tissue, and they had three primary characteristics: wavelength, intensity, and shape. Ca element in tissues has different energy levels, which determine the wavelength of lines.

Table 2 illustrates the results of 12 dentine spectra (of **Figure 3**) at various wavelengths and their associated peak areas. The intensity (count/nm) of the integrated

| Energy Density (J/cm ²) | Integrated Peak Areas at different Intensities (Count per nm) | | | | |
|-------------------------------------|---|-------------|---------------------------------|-----------------------|-------------|
| | At 395.5 nm, 397.5 nm | At 409.5 nm | At 416.5 nm, 417.5 nm, 419.3 nm | At 423.2 nm, 426.4 nm | At 431.2 nm |
| 3.7 | 8 | 6.5 | 6.8 | 5 | 5.6 |
| 4.25 | 8 | 6.5 | 6.95 | 5 | 6 |
| 5.8 | 10 | 9.7 | 8.4 | 6 | 7.3 |
| 6.8 | 11 | 10.8 | 9 | 6.5 | 8 |
| 7.85 | 11 | 11.1 | 10 | 6.7 | 10 |
| 8.8 | 11 | 12.1 | 10 | 7 | 11 |
| 10.1 | 14 | 12 | 14 | 9 | 12.8 |
| 11.2 | 21 | 19 | 16 | 12 | 16 |
| 12.4 | 23 | 20 | 20 | 14 | 19.1 |
| 13.6 | 27 | 26 | 23 | 17 | 20 |
| 14.8 | 32 | 29 | 28 | 19.48 | 25 |

Table 1.
Peak area calculation for calcium in enamel using axiom LA software.

| Energy Densities (J/cm ²) | Integrated Peak Areas at different Intensities (Counts/nm) | | | | |
|---------------------------------------|--|-------------|---------------------------------|---------------------|-------------|
| | At 395.5 nm, 397.5 nm | At 409.5 nm | At 416.5 nm, 417.5 nm, 419.3 nm | At 423 nm, 426.4 nm | At 431.2 nm |
| 2.4 | 4.3 | 3 | 4 | 3 | 3.2 |
| 3.7 | 4.8 | 4 | 4.2 | 3 | 3.6 |
| 4.25 | 6.8 | 5.3 | 6 | 3 | 4 |
| 5.8 | 6 | 5.8 | 6.2 | 3.1 | 4.3 |
| 6.8 | 8.7 | 7.6 | 6.1 | 3.1 | 5.1 |
| 7.85 | 13.6 | 11.4 | 7.8 | 3.4 | 6.1 |
| 8.8 | 16.1 | 13.1 | 8.7 | 3.4 | 7 |
| 10.1 | 16.2 | 13 | 8.8 | 3.4 | 6.6 |
| 11.2 | 17 | 13.2 | 8.1 | 3.8 | 6.2 |
| 12.4 | 24 | 20 | 10.4 | 4.2 | 8 |
| 13.6 | 26.4 | 20.2 | 12.4 | 4.6 | 9.6 |
| 14.8 | 24 | 19.8 | 13.2 | 4.8 | 9.8 |

Table 2.
Peak area calculation for calcium in dentine using axiom LA software.

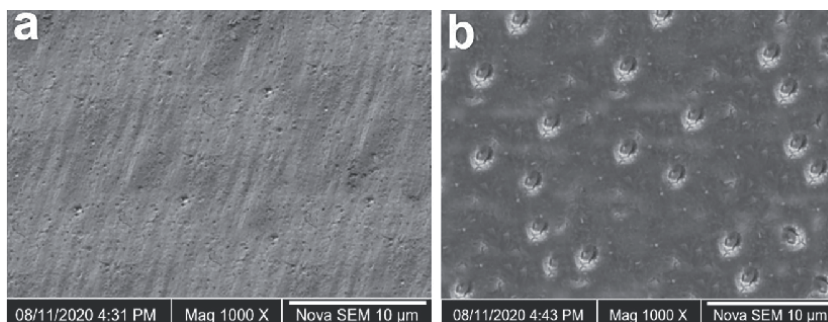


Figure 4. SEM micrographs of sample2 right after cutting with diamond disc (a) enamel slice (b) dentin slice.

peak area increases as energy density increases. The largest peak area was 26.4 counts/nm at 13.6 J/cm^2 , and a minimum of 3 counts/nm at laser energy densities of 2.4 J/cm^2 , 3.7 J/cm^2 , and 4.25 J/cm^2 .

4.3 Surface morphological analysis of enamel and dentin

Figure 4 represents electron micrographs of dental tissues obtained by SEM at $1000\times$ magnification. The enamel surface is not very smooth, covered with smear layers, and a few tiny holes throughout the surface are shown in **Figure 4(a)**. Pores, bubbles, and debris are examined in dentin in **Figure 4(b)**. The measured mean area of particle debris is $2.1 \mu\text{m}^2$ and the mean distance between two consecutive debris is $0.6 \mu\text{m}$ in dentin tissue. In both tissues, smeared Layers observed which formation of micro and nanocrystalline structures is, bit blurriness is an obstacle act of layers in the field of vision and imaging.

5. Discussion

In the present research, we employed two spectroscopic techniques (LIBS & SEM), which were complemented by electron microscopy. When a high-power pulsed laser beam hits the target, it causes localized heating and vaporization of the sample materials. The ablated material expands and forms a plasma plume. Hence, there is a relationship between plasma intensity and ablated material. LIBS is used to define an element in a sample and plasma intensity. Emission intensity is linearly correlated to the number of elements in the sample [10].

Figure 5 represents the plot of peak area versus energy density (there are five exponential lines: purple, green, blue, black and red at intensities of (395.5 nm, 397.5 nm), (409.5 nm), (416.5 nm, 417.5 nm, 419.3 nm), (423.2 nm, 426.4 nm) and 431.2 nm, respectively. There are 11 points in each curve that represent peak areas at different energy densities. The line of best fit is drawn which intercepts the x-axis at 1.41 J/cm^2 and gives the threshold ablation value of energy density for enamel at the 14th shot.

| Calcium emission wavelength (nm) | Equations | slope | x-intercept |
|----------------------------------|-------------------------|-------|-------------|
| 395.53975 | $y = 4.4655e^{0.1287x}$ | 2.1 | 1.418 |
| 409.5 | $y = 3.9591e^{0.133x}$ | 1.9 | 1.415 |
| 416.5, 417.5, 419.3 | $y = 3.8412e^{0.1295x}$ | 1.8 | 1.413 |
| 423.2, 426.4 | $y = 3.3446e^{0.1358x}$ | 1.2 | 1.410 |
| 431.2 | $y = 2.7536e^{0.1287x}$ | 1.7 | 1.414 |

Line of best fit: slope: 2.10 x-intercept: 1.41.
 Threshold ablation for calcium in enamel: 1.41 J/cm².

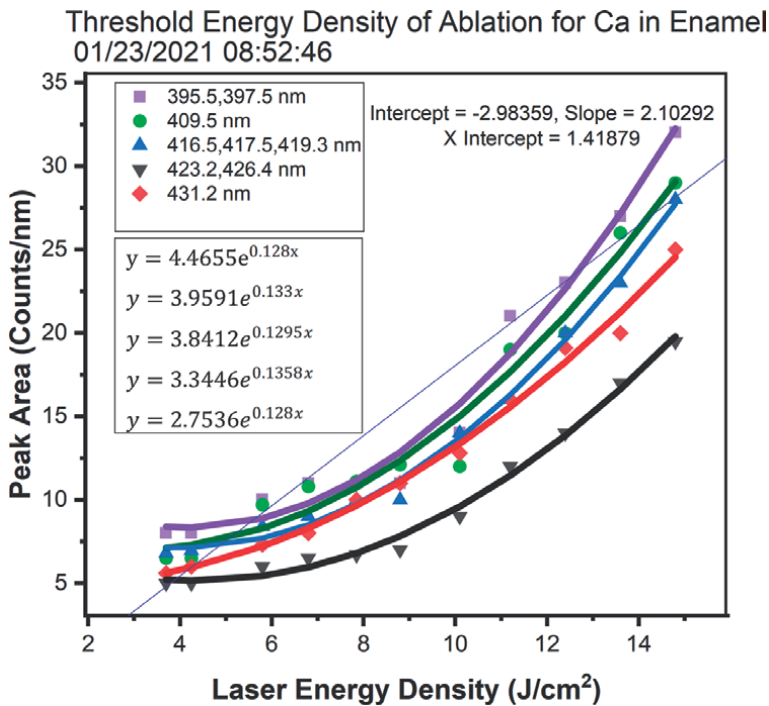


Figure 5. Threshold energy density of ablation for calcium in the enamel.

The integrated peak area for calcium at (395.5 nm, 397.5 nm), (409.5 nm), (416.5 nm, 417.5 nm, 419.3 nm), (423.2 nm, 426.4 nm), and 431.2 nm were plotted for different energy densities in **Figure 6**. There are five linear lines: purple, green, blue, black and red. Each line has 12 points representing peak areas at different energy densities. The line of best fit is drawn such that the intercept x-axis at 0.38 J/cm² gives the threshold ablation value of energy density for dentine at the 4th laser pulse (shots).

| Calcium emission wavelength (nm) | Equations | slope | x-intercept |
|----------------------------------|---------------------|-------|-------------|
| 395.53975 | $y = 1.64x - 0.628$ | 1.6 | 0.38 |
| 409.5 | $y = 1.46x - 0.564$ | 1.4 | 0.38 |
| 416.5, 417.5, 419.3 | $y = 1.05x - 0.418$ | 1.0 | 0.39 |
| 423.2, 426.4 | $y = 0.58x - 0.222$ | 0.5 | 0.38 |
| 431.2 | $y = 0.70x - 0.277$ | 0.7 | 0.38 |

Line of best fit: slope: 1.64 X-intercept: 0.38.
 Threshold ablation for calcium in enamel: 0.38 J/cm².

It can be spotted from **Figures 5** and **6** that the peak areas of enamel and dentine Ca lines are set up at laser energy densities of 3.35 J/cm^2 and 2.43 J/cm^2 respectively. By data fitting curves analysis, an exponential fit is observed for enamel and a linear fit for dentine. The curves in (**Figures 5** and **6**), combine to intersect the x-axis that gives us threshold ablation, in enamel and dentine tissues respectively. Outcomes of LIBS revealed that the threshold ablation for Ca in enamel is approximately four times that of the threshold ablation for Ca in dentine. SEM analysis was conducted to figure out the reason for the huge difference in threshold ablations for calcium in dental tissues by examining their surface topography and structural properties. SEM micrographs in **Figure 4** show that enamel has smear layers that are close to each other's making its structure rigid, hard and calcified. Pores, bubbles, and open spaces on the dentine surface make it delicate, flexible, and less calcified, which is a primary reason for having lower threshold ablation for Ca as compared to enamel [23–27].

Chemical compositional studies of dental tissues determine that they contain hydroxyapatite crystal (HAP), the main mineral constituent of teeth, which is the most stable and least soluble, form of calcium phosphate. The average size of HAP is larger in enamel than dentine, which makes the former more calcified. In addition, enamel contains 95% inorganic material, 1% organic material, and 4% water by weight percentage, whereas dentin is composed of 70% inorganic material, 2% organic material, and 10% water by weight percentage [28–30]. Hence, the compositional analysis revealed that enamel has a lower concentration of water and higher mineral content (than dentin) which makes it difficult to ablate.

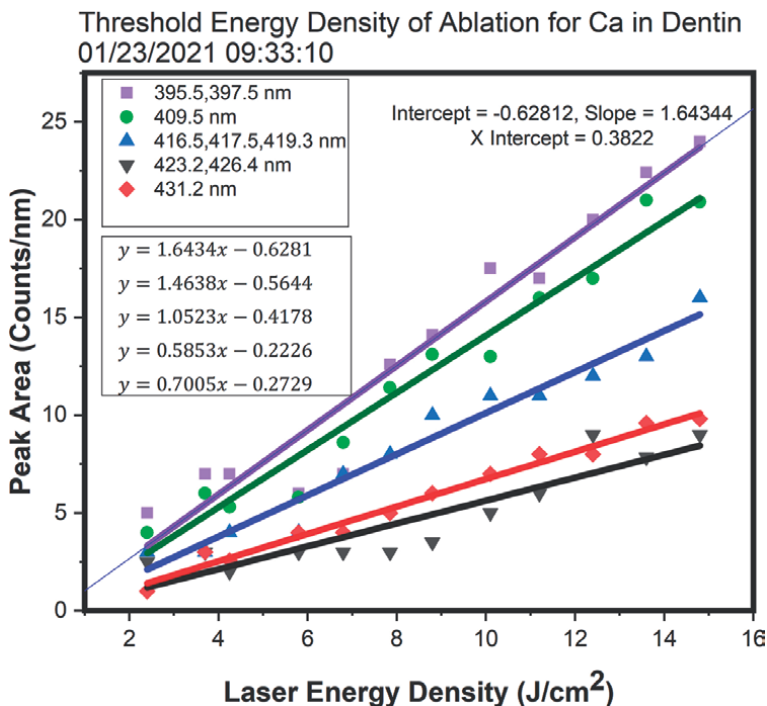


Figure 6.
 Threshold energy density of ablation for calcium in dentine.

6. Conclusions

The LIBS technique has been successfully applied to compute threshold ablation for calcium in dental tissues. Findings revealed that enamel has a higher threshold of ablation for calcium than dentine. SEM microstructural observations and measurements suggest that enamel has a closely packed structure of smear layers making it hard whereas a high porosity level in dentin causes less toughness. These findings are beneficial in the field of dentistry for the use of lasers in dental treatment.

Acknowledgements

We are grateful to Dental Habitat and Dental & Curatives and Implant Center for providing experimental facilities to conduct our research work.

Conflict of interest

The authors declare no conflict of interest.

Appendices and nomenclature

| | |
|-------|--|
| LASER | light amplification by stimulated emission and radiation |
| Nd | YAG, Neodymium-doped yttrium aluminum garnet |
| LIBS | laser-induced breakdown spectroscopy |
| LA | laser ablation |
| LIPS | laser-induced plasma spectroscopy |
| IR | infrared |

Author details


Muhammad Mustafa^{1*}, Anwar Latif¹ and Majid Jehangir²

1 University of Engineering and Technology, Lahore, Pakistan

2 Dental and Curatives and Implant Center, Lahore, Pakistan

*Address all correspondence to: m2dastageer25@gmail.com

IntechOpen

© 2022 The Author(s). Licensee IntechOpen. This chapter is distributed under the terms of the Creative Commons Attribution License (<http://creativecommons.org/licenses/by/3.0>), which permits unrestricted use, distribution, and reproduction in any medium, provided the original work is properly cited. 

References

- [1] Alkaisi A, Abdo SB. Modification of enamel surface morphology and strength using Nd: YAG laser with proper and safe parameters. *European Journal of General Dentistry*. 2021;**10**(03):123-128. DOI: 10.1055/s-0041-1736378
- [2] Galui S, Pal S, Mahata S, Saha S, Sarkar S. Laser and its use in pediatric dentistry: A review of literature and a recent update. *International Journal of Pedodontic Rehabilitation*. 2019;**4**(1):1. DOI: 10.4103/ijpr.ijpr_17_18
- [3] Arjunkumar R. Awareness of Laser Dentistry Among Dentists in Tanjore-A survey. *Biomedical and Pharmacology Journal*. 2018 Sep 21;**11**(3):1623-32. DOI: 10.13005/bpj/1530
- [4] Bawazir R, Alhaidary D, Gutknecht N. The current state of the art in bond strength of laser-irradiated enamel and dentin (Nd: YAG, CO2 lasers) part 1: A literature review. *Lasers in Dental Science*. 2020;**4**(1):1-6. DOI: 10.1007/s41547-020-00084-w
- [5] Tzanakakis EG, Skoulas E, Pepelassi E, Koidis P, Tzoutzas IG. The use of lasers in dental materials: A review. *Materials*. 2021;**14**(12):3370. DOI: 10.3390/ma14123370
- [6] Labunet A, Tonea A, Kui A, Sava S. The use of laser energy for etching enamel surfaces in dentistry—A scoping review. *Materials*. 2022;**15**(6):1988. DOI: 10.3390/ma15061988
- [7] Cobb CM. Lasers and the treatment of periodontitis: The essence and the noise. *Periodontology 2000*. 2017;**75**(1):205-295. DOI: 10.1111/prd.12137
- [8] Parker S, Cronshaw M, Anagnostaki E, Mylona V, Lynch E, Grootveld M. Current concepts of laser–Oral tissue interaction. *Dentistry Journal*. 2020;**8**(3):61. DOI: 10.3390/dj8030061
- [9] Loganathan S, Santhanakrishnan S, Bathe R, Arunachalam M. Prediction of femtosecond laser ablation parameter on human teeth using chemical compositional analysis. *Procedia Manufacturing*. 2019;**34**:379-384. DOI: 10.1016/j.promfg.2019.06.181
- [10] Mustafa M. Impact of Laser Radiation on Dominant Human Body Constitutional Metals [Thesis]. Pakistan: University of Engineering and Technology; 2021
- [11] Maurya GS, Marín-Roldán A, Veis P, Pathak AK, Sen P. A review of the LIBS analysis for the plasma-facing components diagnostics. *Journal of Nuclear Materials*. 2020;**541**:152417. DOI: 10.1016/j.jnucmat.2020.152417
- [12] El-Saeid RH, Abdelhamid M, Abdel-Salam Z, Abdel-Harith M. Exploiting LIBS to analyze selected rocks and to determine their surface hardness based on the diagnostics of laser-induced plasma. *Applied Physics B*. 2020;**126**(1):1. DOI: 10.1007/s00340-019-7356-z
- [13] Batool J, Amin N, Jamil Y, Shaikh N, Al Islam S. Rapid elemental analysis of human teeth using laser-induced breakdown spectroscopy. *Physica B: Condensed Matter*. 2021;**602**:412495. DOI: 10.1016/j.physb.2020.412495
- [14] Keerthi K, George SD, Kulkarni SD, Chidangil S, Unnikrishnan VK. Elemental analysis of liquid samples by laser-induced breakdown spectroscopy (LIBS): Challenges and potential experimental strategies. *Optics and Laser Technology*. 2022;**147**:107622. DOI: 10.1016/j.optlastec.2021.107622

- [15] Tiwari PK, Behera N, Singh RK, Joshi HC. Comparative study of LIBS signal for single and colliding plasma plumes in a variable magnetic field. *Spectrochimica Acta Part B: Atomic Spectroscopy*. 2022;**191**:106411. DOI: 10.1016/j.sab.2022.106411
- [16] Hu Z, Zhang D, Wang W, Chen F, Xu Y, Nie J, et al. A review of calibration-free laser-induced breakdown spectroscopy. *TrAC, Trends in Analytical Chemistry*. 2022;**152**:116618. DOI: 10.1016/j.trac.2022.116618
- [17] Akhtar K, Khan SA, Khan SB, Asiri AM. Scanning electron microscopy: Principle and applications in nanomaterials characterization. In: *Handbook of Materials Characterization*. Cham: Springer; 2018. pp. 113-145. DOI: 10.1007/978-3-319-92955-2_4
- [18] Mazumder M, Ahmed R, Ali AW, Lee SJ. SEM and ESEM techniques used for analysis of asphalt binder and mixture: A state of the art review. *Construction and Building Materials*. 2018;**186**:313-329. DOI: 10.1016/j.conbuildmat.2018.07.126
- [19] Lenthe WC, Stinville JC, Echlin MP, Chen Z, Daly S, Pollock TM. Advanced detector signal acquisition and electron beam scanning for high resolution SEM imaging. *Ultramicroscopy*. 2018;**195**:93-100. DOI: 10.1016/j.ultramic.2018.08.025
- [20] Skoupy R, Fort T, Krzyzanek V. Nanoscale estimation of coating thickness on substrates via standardless BSE detector calibration. *Nanomaterials*. 2020;**10**(2):332. DOI: 10.3390/nano10020332
- [21] Çarıkçıoğlu B, Misilli T, Deniz Y, Aktaş Ç. Effects of high temperature on dental restorative materials for forensic purposes. *Forensic Science, Medicine and Pathology*. Mar 2021;**17**(1):78-86. DOI: 10.1007/s12024-020-00345-x
- [22]] Nader MN, Fleming DE. Assessment of alternative methods for analyzing X-ray fluorescence spectra. *Applied Radiation and Isotopes*. 2019;**146**:133-138. DOI: 10.1016/j.apradiso.2019.01.033
- [23] Wang R, Zhao D, Wang Y. Characterization of elemental distribution across human dentin-enamel junction by scanning electron microscopy with energy-dispersive X-ray spectroscopy. *Microscopy Research and Technique*. 2021;**84**(5):881-890. DOI: 10.1002/jemt.23648
- [24] Kudkuli J, Agrawal A, Gurjar OP, Sharma SD, Rekha PD, Manzoor MA, et al. Demineralization of tooth enamel following radiation therapy; an in vitro microstructure and microhardness analysis. *Journal of Cancer Research and Therapeutics*. 2020;**16**(3):612. DOI: 10.4103/jcrt.JCRT_8_19
- [25] Lapinska B, Klimek L, Sokolowski J, Lukomska-Szymanska M. Dentine surface morphology after chlorhexidine application—SEM study. *Polymers*. 2018;**10**(8):905. DOI: 10.3390/polym10080905
- [26] Skinner AR, Blackwell BA, Blickstein JI, Lundberg J. Using dentine as well as enamel in ESR dating. *Brazilian Journal of Physics*. 2022;**52**(1):1. DOI: 10.1007/s13538-021-01030-2
- [27] Weerakoon AT, Cooper C, Meyers IA, Condon N, Sexton C, Thomson D, et al. Does dentine mineral change with anatomical location, microscopic site and patient age? *Journal of Structural Biology: X*. 2022;**6**:100060. DOI: 10.1016/j.yjsbx.2022.100060

[28] Lee ES, Wadhwa P, Kim MK, Jiang HB, Um IW, Kim YM. Organic matrix of enamel and dentin and developmental defects. In: Human Teeth–Structure and Composition of Dental Hard Tissues and Developmental Dental Defects. Rijeka: IntechOpen; 2021. DOI: 10.5772/intechopen.99542

[29] Velo MM, Farha AL, da Silva Santos PS, Shiota A, Sansavino SZ, Souza AT, et al. Radiotherapy alters the composition, structural and mechanical properties of root dentin in vitro. *Clinical Oral Investigations*. 2018;**22**(8):2871-2878. DOI: 10.1007/s00784-018-2373-6

[30] Tanaskovic Stankovic S, Tanaskovic I, Jovicic N, Miletic Kovacevic M, Kanjevac T, Milosavljevic Z. The mineral content of the hard dental tissue of mesiodens. *Biomedical Papers*. 2018;**162**(2):149-153. DOI: 10.5507/bp.2018.017

Edited by Mohsen Mhadhbi

This book provides an overview of the principles and types of electron microscopes. It also describes the different practical applications of electron microscopes, ranging from particle analysis and materials characterization to industrial failure analysis and process control. Over eight chapters divided into two sections, this book gives readers a comprehensive and updated review of the latest advances in electron microscopy.

Published in London, UK

© 2022 IntechOpen
© © wacomka / iStock

IntechOpen

